

UNIVERSITÀ
DI PAVIA

Dipartimento di Fisica "A.Volta"

Corso di Laurea Magistrale in Scienze Fisiche

Preliminary In-Vitro and Dosimetric Studies of Boron Neutron Capture Therapy (BNCT) and Carbon Ion Radiotherapy (CIRT) using a Radiobiological 3D Spheroid Model of Pancreatic Cancer

Studi Preliminari In-Vitro e Dosimetrici sulla Terapia per Cattura Neutronica del Boro (BNCT) e sulla Radioterapia con Ioni Carbonio (CIRT) mediante un Modello Radiobiologico 3D a Sferoidi di Carcinoma Pancreatico

Tesi per la laurea di:
Nefeli Eliade

Relatrice:
Prof. Nicoletta Protti

Correlatrice:
Dr Katarzyna Dziedzic-Kocurek

Correlatore:
Dr Alessandro Somenzi

Anno accademico 2025 – 2026

Acknowledgments

I would like to express my sincere gratitude to my supervisor, Prof. Nicoletta Protti, for her insightful guidance throughout this thesis and for giving me the opportunities to constantly grow beyond my comfort zone and expand my skills.

I extend my appreciation to my co-supervisor, Dr Katarzyna Dziedzic-Kocurek, for her kindness and support, as well as to the team in Kraków, Prof. Raczkowska, Anna Cieślik, Svitlana Tymetska, for their warm welcome, their time, and all their help during my traineeship. I am also very thankful to Prof. Rajfur for his great assistance with the confocal microscopy.

Furthermore, I am deeply grateful to my other co-supervisor, Alessandro Somenzi (m.p.), for his continuous guidance and support throughout this work, and especially for his never-ending patience and encouragement, which I truly valued.

Last but not least, I want to thank the most important people in my life, my friends and family, for all their love and constant support.

Abstract

Pancreatic ductal adenocarcinoma (PDAC) is among the most lethal and radioresistant solid tumors, due to its hypoxic, dense microenvironment and its proximity to radiosensitive organs at risk. Carbon ion radiotherapy (CIRT) and Boron Neutron Capture Therapy (BNCT) are two innovative, particle radiotherapy modalities with therapeutic potential against such tumors. CIRT is effective in targeting hypoxic tumors and delivering homogeneous dose distributions, while BNCT is based on biochemical specificity through selective accumulation of B-10 carriers in tumor cells, offering cellular level high-LET radiation confined to the tumor cells. Combining the two modalities, could overcome their individual limitations and synergistically enhance treatment efficacy. However, their biological effectiveness in PDAC, alone or combined, remains largely unexplored. Additionally, conventionally used as in-vitro preclinical models 2D cell cultures, poorly represent the tissue architecture of real tumors, highlighting the need for more accurate preclinical models. This thesis presents an integrated experimental and computational framework for evaluating BNCT and CIRT, individually and combined, using 3D PANC-1 spheroids as a pancreatic cancer model.

Initially, the 3D PANC-1 spheroids were characterized by size and shape assessment. In addition, the spatial distribution of the viability of the spheroid cells was mapped by confocal fluorescent microscopy, showing a necrotic core surrounded by a viable proliferating shell, accounting for 46% of the spheroid volume. The boron uptake of the spheroids, following incubation with the boron carrier boronophenylalanine (BPA), was quantified by Inductively Coupled Plasma Mass Spectrometry (ICP-MS). Preliminary qualitative attempts of performing boron localization in the biological samples have been done by neutron autoradiography. Spheroids were then irradiated with thermal neutrons at the TRIGA Mark II reactor in LENA, with and without prior BPA incubation, with C-ions at CNAO, and with a combination of the two. Their response was followed through radius regression over 10 days post-irradiation. 2D monolayers were studied in parallel by clonogenic assays. Moreover, Monte Carlo simulations (MCNP6) of the spheroids in a 96-well plate inside the reactor's thermal column provided the dosimetry.

Boron uptake in 3D spheroids was about an order of magnitude lower than in 2D monolayers (1.1-1.5 vs 15-17 ppm), and simulated BNCT doses to spheroids were correspondingly lower, supporting the hypothesis that 2D cultures overestimate BNCT efficacy. BNCT treatment at physical doses of 0.7Gy induced spheroid shrinkage comparable in effect to 4Gy of C-ions, corresponding to a size reduction of $\sim$38% and $\sim$24%, respectively. Neutron irradiations without BPA did not generate a significant effect. The preliminary combined CIRT-BNCT experiments produced a size regression of about $\sim$34%, comparable to the single modalities. Due to the variability between spheroids and the limited statistics, no definitive additive or synergistic effect can be clearly established by the present study.

The findings of the present thesis support 3D spheroids as a more realistic model for BNCT dosimetry and provide the first experimental data on combined CIRT-BNCT in a 3D pancreatic model.

Abstract (Italian)

Il carcinoma duttale pancreatico (PDAC) è tra i tumori solidi più letali e radioresistenti, a causa del suo microambiente ipossico e denso e della prossimità a organi a rischio radiosensibili. La radioterapia con ioni carbonio (CIRT) e la terapia per cattura neutronica con boro (BNCT) sono due modalità innovative di radioterapia con particelle che presentano un potenziale terapeutico contro tali tumori. La CIRT è efficace nel colpire i tumori ipossici e nel fornire distribuzioni di dose omogenee, mentre la BNCT si basa sulla specificità biochimica ottenuta mediante l'accumulo selettivo di vettori del ^{10}B nelle cellule tumorali, producendo radiazione ad alto LET a livello cellulare, confinata alla cellula tumorale. La combinazione delle due modalità potrebbe superare i rispettivi limiti individuali e potenziare in modo sinergico l'efficacia del trattamento. Tuttavia, la loro efficacia biologica nel PDAC, da sole o in combinazione, rimane in larga parte inesplorata. Inoltre, le colture cellulari 2D, convenzionalmente impiegate come modelli preclinici in vitro, rappresentano in modo inadeguato l'architettura tissutale dei tumori reali, evidenziando la necessità di modelli preclinici più accurati. Questa tesi presenta un framework sperimentale e computazionale integrato per la valutazione della BNCT e della CIRT, singolarmente e in combinazione, utilizzando sferoidi 3D di cellule PANC-1 come modello di tumore pancreatico.

Inizialmente, gli sferoidi 3D di PANC-1 sono stati caratterizzati mediante la valutazione di dimensioni e forma. Inoltre, la distribuzione spaziale della vitalità cellulare all'interno degli sferoidi è stata mappata mediante microscopia confocale a fluorescenza, evidenziando un nucleo necrotico circondato da un guscio proliferante e vitale, pari al 46% del volume dello sferoide. L'assorbimento di boro da parte degli sferoidi, in seguito a incubazione con il vettore del boro boronofenilalanina (BPA), è stato quantificato mediante spettrometria di massa ICP (Inductively Coupled Plasma Mass Spectrometry, ICP-MS). Tentativi preliminari per la valutazione qualitativa della distribuzione spaziale del boro entro gli sferoidi sono stati fatti sfruttando la tecnica della autoradiografia neutronica. Gli sferoidi sono stati quindi irradiati con neutroni termici presso il reattore TRIGA Mark II del LENA di Pavia, con e senza previa incubazione con BPA, con ioni carbonio presso il CNAO, e con una combinazione delle due modalità. La loro risposta è stata monitorata attraverso la regressione del raggio nei 10 giorni successivi all'irradiazione. In parallelo, colture cellulari 2D sono state studiate mediante saggi clonogenici. Inoltre, simulazioni Monte Carlo (MCNP6) degli sferoidi in una piastra a 96 pozzetti all'interno della colonna termica del reattore hanno fornito la dosimetria computazionale di supporto all'interpretazione dei dati radiobiologici.

L'assorbimento di boro negli sferoidi 3D è risultato inferiore di circa un ordine di grandezza rispetto ai monostrati 2D (1.1-1.5 contro 15-17 ppm), e le dosi BNCT simulate negli sferoidi sono risultate di conseguenza più basse, supportando l'ipotesi che le colture 2D sovrastimano l'efficacia della BNCT. Il trattamento BNCT a dosi fisiche di 0,7 Gy ha indotto una riduzione degli sferoidi di entità paragonabile a quella ottenuta con 4 Gy di ioni carbonio, corrispondente a una riduzione di dimensioni di circa il 38% e il 24%, rispettivamente. Gli irraggiamenti con neutroni in assenza di BPA non hanno generato un effetto significativo. Gli esperimenti preliminari di combinazione CIRT-BNCT hanno prodotto una regressione dimensionale di circa il 34%, paragonabile a quella

delle singole modalità. A causa della variabilità tra gli sferoidi e della statistica limitata, il presente studio non consente ancora di stabilire in modo definitivo un effetto additivo o sinergico.

Questi risultati supportano l'impiego degli sferoidi 3D come modello più realistico per la dosimetria BNCT e forniscono i primi dati sperimentali sulla combinazione CIRT-BNCT in un modello pancreatico 3D.

Contents

Abstract ii

Abstract (Italian) iii

1 Introduction 1
1.1 Significance of the thesis . . . 1
1.2 Objectives . . . 3

2 Theoretical Framework 5
2.1 Radioresistant Solid Tumors . . . 5
2.1.1 Pancreatic Ductal Adenocarcinoma (PDAC) . . . 6
2.2 Advanced Particle Therapy Approaches . . . 7
2.2.1 Carbon Ion Radiation Therapy (CIRT) . . . 7
2.2.2 Neutron Capture Therapy (NCT) . . . 9
2.2.3 Combination Therapy . . . 11
2.3 3D Tumor Spheroids as a Radiobiological Model . . . 12

3 Materials and Methods 14
3.1 Computational Dosimetry . . . 14
3.1.1 MCNP6 Simulations of the radiation dose delivered to the 3D tumor spheroids . . . 14
3.1.1.1 Geometry of the 96-well U-bottom plate containing spheroids . . . 14
3.1.1.2 Translated source and Target placement . . . 17
3.1.2 BNCT Dose Components . . . 18
3.1.3 Scored Physical Quantities . . . 18
3.1.3.1 Total Absorbed Dose . . . 20
3.1.3.2 Survival Fraction (SF) as a function of the dose . . . 20
3.2 Experimental Methodology . . . 21
3.2.1 Cell Culture Models: 2D Monolayer and 3D Spheroids . . . 21
3.2.2 Spheroid Characterization . . . 22
3.2.2.1 Size and Shape Assessment . . . 22
3.2.2.2 Spheroid Imaging . . . 23
3.2.3 Boron Uptake Studies . . . 24
3.2.3.1 BPA solutions preparation . . . 24
3.2.3.2 Cytotocixcity of BPA . . . 25
3.2.3.3 Boron Uptake Studies in in-vitro 2D and 3D models . . . 25
3.2.4 Irradiation Experiments . . . 28
3.2.4.1 Radiation Facilities . . . 28
3.2.4.2 Sample Seeding and Pre-Irradiation Conditioning . . . 30
3.2.4.3 Irradiation Protocols . . . 30
3.2.4.4 Post-Irradiation Analysis . . . 31
3.2.4.5 Statistical Analysis . . . 33

4 Results and Discussion 34
4.1 Computational Results . . . 34
4.2 Experimental Results . . . 36
4.2.1 Spheroid Characterization . . . 36

4.2.1.1 Size and shape assessment 36
4.2.1.2 Spheroid Imaging 38
4.2.2 Boron Uptake Studies 39
4.2.2.1 Cytotoxicity of BPA 39
4.2.2.2 Boron Uptake Studies in in-vitro 2D and 3D models 39
4.2.3 Radiobiological Response of PANC-1 2D Monolayers and 3D Spheroids to Neutron, BNCT, C-ion, and Combined Irradiation 44
4.2.3.1 2D Cultures 44
4.2.3.2 3D Spheroids 44
4.2.4 Comparative analysis 51

5 Conclusions **59**
5.1 Summary of key findings 59
5.2 Preliminary nature of the study and future directions 61

References **63**

List of Figures

1.1 Estimated numbers of incidence and mortality of pancreatic cancer worldwide from 2024 to 2050, Males and Females aged 0-85+ [3]. 1

2.1 The oxygen fixation hypothesis. About two-thirds of the biologic damage produced by x-rays is by indirect action mediated by free radicals. The damage produced by free radicals in DNA can be repaired under hypoxia but may be "fixed" (made permanent and irreparable) if molecular oxygen is available [28]. 6
2.2 Anatomy of the pancreas including a ductal adenocarcinoma and a neuroendocrine tumor [30]. 6
2.3 Comparative depth–dose profiles of photons, protons, and carbon ions [14] 8
2.4 Distribution of DNA damage inducing ionization events along the particle tracks, after exposure to IR of low ($0.5keV$ electrons) and high ($4MeV$ alpha particles) LET. Large dots represent ionizations and small dots represent excitations. The tracks are simulated by Monte Carlo on the same scale as the DNA [37] 9
2.5 Schematic diagram of the dual targeting mechanism of BNCT. (A) Biochemical targeting: Selective accumulation of boron agents in cancer cells. (B) Physical targeting: Cellular-scale precision from neutron capture reactions [14]. 10
2.6 Diagram illustrating the characteristics of monolayer cell culture models and 3D spheroids, highlighting the unique features of each system. [57] 12
2.7 Scheme of similarities between in vitro spheroids and in vivo tumors, featuring the layered structure, the decreased availability of oxygen and nutrients for cells of deeper layers and cell-cell signaling and contact.[62] 13

3.1 Multiscale view of the MCNP6 geometry model showing the 96-well plate setup (left), a single U-bottom well including the spheroid and DMEM (center), and a magnified view of the 3D concentric tumor spheroid structure featuring the necrotic core and the proliferating shell (right). [Magenta=air, green=DMEM medium, polystyrene=blue, yellow=proliferating tissue, light blue=necrotic tissue] 16
3.2 Top-down view of the MCNP6 model illustrating the complete thermal column irradiation cavity containing the translated source and the 96-well plate positioned at the beam entrance side (left) and a magnified view of the full 96 well-plate array containing the spheroids (right). The physical quantities were scored in the two cells marked with yellow. [Magenta=air, green=DMEM medium, polystyrene=blue] 16
3.3 2D representations of the Triga Mark II geometry simulated with MCNP. (a) top view (b) lateral view. [Grey: concrete, dark grey: graphite, magenta: bismuth, blue: cooling pool, white: air] [64]. 17
3.4 The thermal column of TRIGA II Mark reactor (longitudinal view). The samples were irradiated at position 1. [Grey: graphite, magenta: bismuth, green: boral (borated aluminium), white: air] [69]. 18
3.5 PANC-1 cell cultures: 3D spheroid in 96-well plate and 2D monolayer in T-75 flask. Created in BioRender.com. 22
3.6 The same PANC-1 tumor spheroid on day 5 after seeding, with different magnifications: (a) $x4$, (b) $x10$, (c) $x20$. 23
3.7 Schematic diagram of an inductively coupled plasma mass spectometer [78]. 26
3.8 Spheroids embedded in an OCT matrix at room temperature. 28
3.9 (a) The TRIGA Mark II reactor at L.E.N.A., Pavia. (b) Cherenkov light torch illuminating the reactor core when operating above 100 kW. 28

3.10 The thermal column (blue) of the TRIGA Mark II reator at LENA. 29
3.11 The CNAO hadrontherapy synchrotron facility in Pavia. 29

4.1 PANC-1 tumor spheroid on days 1-5 after seeding, with different magnifications ($x4$, $x10$, $x20$). 36
4.2 Spheroid radius sizes over 5 consecutive days from the day of seeding. 37
4.3 Spheroids shape parameters (circularity and solidity) over 5 consecutive days from day of seeding. 37
4.4 Confocal laser scanning microscopy of a PANC-1 spheroid, combined with live/dead fluorescent staining. Captured at $10x$ magnification. 38
4.5 3D representation of a PANC-1 spheroids after confocal laser scanning microscopy, combined with live/dead fluorescent staining. Captured at $10x$ magnification. 38
4.6 3D PANC-1 spheroids embedded in OCT (a) Histological staining with hematoxylin and eosin (b) Autoradiography after BPA incubation using an air-dried sample. 41
4.7 Neutron autoradiographies of an air-dried sample of 3D PANC-1 spheroids embedded in OCT (a) after 2h incubation with BPA 4mM, (b) control with no BPA. 42
4.8 Neutron autoradiographies of a freeze-dried sample of 3D PANC-1 spheroids embedded in OCT after 2h incubation with BPA 4mM captured by (a) an optical microscope and (b) a stereomicroscope 43
4.9 Normalized radius of spheroids irradiated with neutrons with and without BPA, with respect to the irradiation time. 45
4.10 Normalized Radius of spheroids irradiated with neutrons, with respect to the days post-irradiation. [mean ± SEM] 46
4.11 Normalized Radius of spheroids irradiated with neutrons after incubation with BPA, with respect to the days post-irradiation. [mean ± SEM] 47
4.12 Comparison of the normalized radius of spheroids irradiated with 5 min neutron irradiation with and without a 2h incubation with BPA, as a function of the days post-irradiation. . . . 47
4.13 Normalized Radius of spheroids irradiated with different doses of C-ions, with respect to the days post-irradiation. [mean ± SEM] 48
4.14 Normalized Radius of spheroids irradiated with a combination of C-ions (2Gy) and neutrons, with respect to the days post-irradiation. [mean ± SEM] 49
4.15 Normalized Radius of spheroids irradiated with a combination of C-ions (2Gy) and neutrons after incubation with BPA, with respect to the days post-irradiation. [mean ± SEM] 50
4.16 Picture taken at x10 magnification of the same spheroid, day 10 post-irradiation (2h BPA incubation and 10min thermal neutron beam exposure) , before (left) and after (right) the change of medium. 50
4.17 LQ fit of the survival curve of the clonogenic survival assays for 2D PANC-1 cell cultures after exposure to C-ions (pink), neutrons (blue) and BNCT (green). 52
4.18 LQ fit of the survival curve of the clonogenic survival assays for 2D PANC-1 cell cultures after exposure to C-ions (blue) and comparison with the reference results [52] (grey). 53
4.19 Normalized 3D spheroid radii with respect to the irradiation conditions boxplots (A) C-ions (B) neutrons/BPA+neutrons (C) Comparison among irradiation modalities. Asterisks indicate statistically significant differences: *$p < 0.05$, ** $p < 0.01$, and *** $p < 0.001$. 55
4.20 Comparison of the effect on the 3D spheroids radii after irradiation with ∼1Gy across different irradiation modalitites. Asterisks indicate statistically significant differences: *$p < 0.05$, ** $p < 0.01$, and *** $p < 0.001$. 56
4.21 PANC-1 spheroid photos comparison captured at x10 magnification: (i) 1Gy C-ion irradiation, on day 10 post-irradiation (ii) 5 minutes n irradiation with 2h BPA incubation, on day 9 post-irradiation (iii) 10 minutes n irradiation without BPA incubation on day 10 post-irradiation (iv) 10 minutes n irradiation with 2h BPA incubation on day 10 post-irradiation. 57
4.22 PANC-1 spheroids captured at x10 magnification exposed to ∼1Gy BNCT (left) and 4Gy C-ion irradiation (right), on day 8 post-irradiation, from the same biological replicate. . . . 58

List of Tables

2.1 Q-values for thermal neutron capture in ^{10}B, ^{157}Gd, and ^{6}Li. 11

3.1 Elemental composition, nuclide identification number, and densities of the materials used in the simulation. 15
3.2 Comparison of thermal neutron (25meV) cross sections and Q-values of the main reactions of interest in BNCT dosimetry [70]. 18
3.3 Summary of the experimental irradiation conditions. 31

4.1 MCNP6 simulation dose rates results and associated relative errors scored in 3D tumor spheroids irradiated in the thermal column of the Pavia TRIGA Mark II reactor. 34
4.2 Total absorbed dose calculation results (D_{tot} ± SD in Gy). 35
4.3 ICP-MS results of ^{10}B uptake in 2D cell monolayers and 3D tumor spheroids following BPA incubation. 40
4.4 Comparison between the initial bulk 3D ICP-MS ^{10}B concentrations (measured across the whole spheroid volume) and the concentrations normalized to the viable proliferating shell in 3D PANC-1 tumor spheroids [mean ± SD]. 41
4.5 Clonogenic surviving fraction and delivered physical absorbed doses in 2D PANC-1 cell monolayers. 44
4.6 BNCT 1: Normalized radius ($R_{\text{day10}}/R_{\text{day}-1}$) and spheroid regression across different irradiation times with and without BPA. 45
4.7 BNCT 2: Normalized radius ($R_{\text{day9}}/R_{\text{day}-1}$) and regression across biological replicates (a, b, c) under various incubation and exposure conditions. 46
4.8 C-ions: Dose-response and spheroid regression ($R_{\text{day10}}/R_{\text{day}-1}$) across biological replicates exposed to carbon ion beams. 48
4.9 C-ions and BNCT Combination: Combined effect of carbon ion irradiation (2 Gy) and neutron exposure with or without BPA on spheroid regression. 49
4.10 Percentage of boron enhancement across experimental setups. 51
4.11 Linear-quadratic model parameters (α, β) and calculated α/β ratios with standard propagated uncertainties. 52
4.12 Comparison of absorbed doses between PANC-1 2D monolayer cultures and 3D spheroids (shell vs core) across irradiation modalities. (value ± SD) 54

List of Abbreviations

BNCT Boron Neutron Capture Therapy

CIRT Carbon Ion Radiation Therapy

PDAC Pancreatic Ductal Adenocarcinoma

TME Tumor Microenvironment

OAR Organ at risk

OER Oxygen Enhancement Ratio

LET Linear Energy Transfer

RBE Relative Biological Effectiveness

BPA Boronophenylalanine

TRIGA Training, Research and Isotopes-production General Atomics

LENA Laboratorio Energia Nucleare Applicata

CNAO Centro Nazionale di Adroterapia Oncologica

ROS Reactive Oxygen Species

DNA Deoxyribonucleic acid

IR Ionizing Radiations

NET Neuroendocrine tumor

PT Proton Therapy

SSB Single Strand Breaks

DSB Double Strand Breaks

NCT Neutron Capture Therapy

MRI Magnetic Resonance Imaging

RB-BNCT Reactor-based BNCT

AB-BNCT Accelerator-based BNCT

CTV Clinical Target Volume

NCEPT Neutron Capture Enhanced Particle Therapy

ECM Extracellular Matrix

MCTS Multicellular Tumor Spheroids

PDO Patient-derived Organoid

MCNP Monte Carlo N-Particle Transport Code

ICRU International Commission on Radiation Units and Measurements

UNIPV University of Pavia

SSW Surface Source Write

SSR Surface Source Read

CPE Charged Particle Equilibrium

KERMA Kinetic Energy Released in Matter

ppm parts per million

ICP-MS Inductively Coupled Plasma Mass Spectrometry

SF Surviving Fraction

DMEM Dulbecco's Modified Eagle Medium

FBS Fetal Bovine Serum

PBS Phosphate-Buffered Saline

PI Propidium Iodide

LDH Lactate Dehydrogenase

SSTD Solid State Track Detector

OCT Optimal Cutting Temperature

TLS TAE Life Sciences

SOBP spread-out Bragg peak

PE Plating efficiency

LAT1 L-type amino acid transporter 1

LQ Linear Quadratic

IQR Interquartile range

RIBE Radiation Induced Bystander Effect

FNTD Fluorescent Nuclear Track Detectors

Chapter 1

Introduction

1.1 Significance of the thesis

Cancer currently ranks as the second leading cause of mortality worldwide, claiming over 10 million deaths annually [1], and constitutes the leading cause of death among people under 65 years of age in the EU [2]. Estimating more than 20 million annual global incidences and projected to nearly double by 2050, reversing this trend is crucial and it requires a fundamental shift towards a people-centered approach that responds to the needs of the most affected people and communities [1], showcasing the increased need for more precise and personalized therapeutic modalities.

Pancreatic cancer remains one of the deadliest malignancies in the world, responsible for more than 490,000 deaths and roughly 530,000 new incidences in 2024 [3].

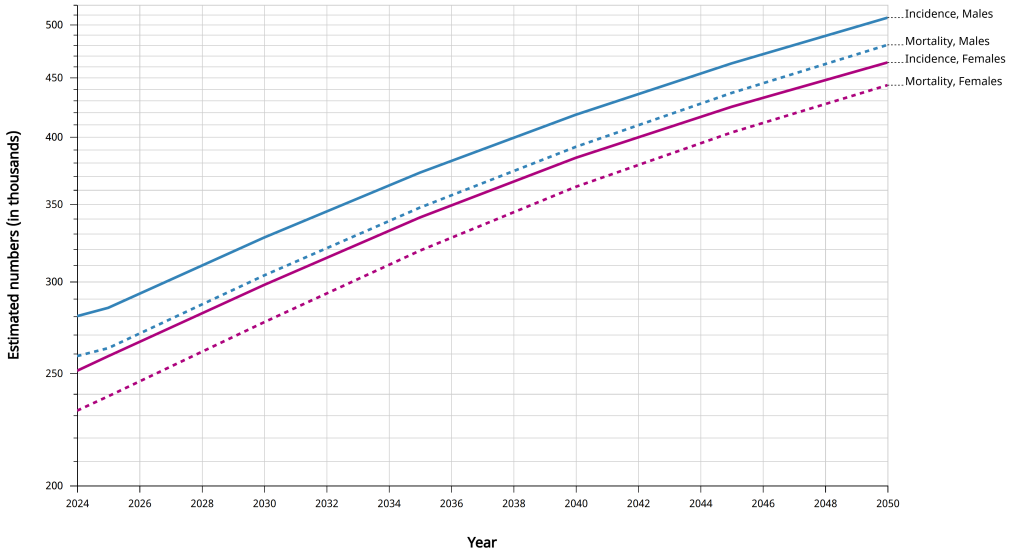


Figure 1.1: Estimated numbers of incidence and mortality of pancreatic cancer worldwide from 2024 to 2050, Males and Females aged 0-85+ [3].

The 5-year relative survival rate is 13% overall, but just 8% for people diagnosed with pancreatic ductal adenocarcinomas (PDAC), which constitute around 95% of the total

cases [4]. Due to the inability to detect the clinical symptoms until late in progression [5], approximately 85% of patients present with unresectable or metastatic disease at the time of diagnosis [6], therefore less than 20% of patients survive past the first year [7], making it one of the cancers with the poorest prognosis, and without much difference between high- and low-income countries [8].

Surgery remains the only treatment that offers curative potential, yet it yields a 5-year survival rate of only 10-25% [6], while conventional treatments such as chemotherapy and radiotherapy do not result in significant improvements in clinical outcomes [7]. This intrinsic resistance is driven by PDAC's dense, immunosuppressive tumor microenvironment (TME) and high hypoxia levels [9], combined by limitations on radiotherapy treatment's dose escalation due to the surrounding radiosensitive organs at risk (OAR) [10], [11], [12]. Consequently, with its increasing incidence and lack of effective therapeutic options, PDAC's cure remains an unmet oncological need [13].

Carbon-ion radiation therapy (CIRT), is one of the most promising treatments for radioresistant tumors characterized by hypoxia and located near sensitive OAR, such as PDACs, because of the decreased oxygen enhancement ratio (OER), the increased linear energy transfer (LET), its superior dose conformity, and its pro-immunogenic role within the TME [12], [14], [9]. However, its therapeutic precision relies solely on spatial targeting of the dose deposition, posing a challenge in minimizing normal tissue toxicity [14].

Boron Neutron Capture Therapy (BNCT) integrates biochemical specificity, through tumor-selective boron-10 (^{10}B) agents, with cellular-level physical precision, releasing short-range, high-LET particles confined to the tumor cell. This dual mechanism holds immense potential for treating recurrent and intractable malignancies [14], with its promising efficacy for recurrent malignant gliomas, head and neck cancers and melanomas already reported in clinical studies [15]. Thus, it is considered as a promising approach for pancreatic tumor treatment [9], although its biological effectiveness against pancreatic tumors remains underexplored [15]. Combining BNCT with another therapeutic modality represents a novel dual-modality strategy that can be capable of overcoming the individual limitations of each approach and synergistically enhance treatment efficacy. While such approaches have gained increasing attention recently, they have yet to be adopted in clinical practices [16].

Even though BNCT is effective against hypoxic tumor cells, studies have confirmed that the uptake of boron compounds is limited in hypoxic and quiescent cell populations, diminishing the treatment's efficacy [17]. Since the intracellular distribution of ^{10}B within tumors influences the relative biological effectiveness (RBE) of the treatment, and the spatial organization of cells can affect the cellular microenvironment and various aspects of cellular physiology, which are known to be highly associated with the RBE of radiation therapies [15], accurate preclinical models are required to evaluate these treatments.

Two-dimensional (2D) monolayer cell cultures are traditionally used to study cellular radiation response and drug accumulation. However, they oversimplify in-vivo conditions, which are crucial for proliferation, metabolism, differentiation and function [18]. Particularly for the immense complexity of PDAC's TME, new models imitating the tissue organization and cell heterogeneity are highly desirable [11]. Conversely, while animal models are widely used in preclinical settings in cancer research for drug screening and RBE evaluations [19], the average translation rate from animal model to clinical cancer patients is less than 8% [15]. Three-dimensional (3D) models, particularly tumor spheroids,

are bridging this gap, as studies have confirmed that they are a feasible environment for testing different radiation types [9]. They can more accurately replicate the cell-cell interactions, tissue architecture and TME features, providing a more ethical, cost-effective and biologically relevant platform for radiobiological and dosimetric assessments, ultimately leading to more reliable estimations [20], [15], [18], [19]. However the interactions between the microenvironment and cancer cells remain to be further elucidated [7], and a substantial amount of work is needed to clarify all parameters that determine radiotherapeutic resistance to use this information to improve the therapy [21].

The presented study emphasizes the need for further research in treatment modalities for radioresistant tumors with high mortality rates, such as PDACs, using more accurate preclinical models, to ultimately contribute to more effective treatment strategies.

1.2 Objectives

The primary aim of this thesis is to establish an integrated experimental and computational framework for the evaluation of BNCT both as a single modality and in combination with CIRT, for the treatment of PDAC. By exploiting 3D in vitro tumor spheroid models, alongside conventional 2D monolayer systems, this work addresses critical preclinical gaps in the evaluation of innovative particle therapy treatments against radioresistant solid tumors.

More specifically, the research is organized into five objectives:

1. Establish and characterize 3D PANC-1 spheroids as a biologically relevant in-vitro model of pancreatic cancer for BNCT dosimetry.
2. Evaluate the cellular uptake and cytotoxicity of the clinically approved boron carrier Boronophenylalanine (BPA) in 3D PANC-1 spheroids, comparing with 2D PANC-1 monolayer cell culture model results.
3. Perform neutron irradiation trials at the TRIGA (Training, Research and Isotopes-production General Atomics) Mark II research reactor mantained at Laboratorio Energia Nucleare Applicata (L.E.N.A.), in the presence and absence of BPA, followed by post-irradiation assessment analysis and comparison with 2D models.
4. Conduct a preliminary irradiation study combining carbon-ion irradiation at the Centro Nazionale di Adroterapia Oncologica (CNAO) with thermal neutron irradiation at LENA after BPA incubation, assessing the potential synergistic or additive effects of CIRT and BNCT, comparing between 2D and 3D models.
5. Develop a computational dosimetry model of the 3D spheroids using MCNP Monte Carlo simulation code for the assessment of BNCT dosimetry exploiting as an irradiation position the modified thermal column of UNIPV LENA reactor.

This thesis provides a preliminary but integrative evaluation of the suitability of PANC-1 spheroids for BNCT research and contributes to the development of more realistic preclinical models for the assessment of emerging radiation therapies.

The work is framed within a broader collaborative project between the Physics Department of Pavia University and CNAO center, which is dedicated to evaluating experimentally the

combined efficacy of CIRT and BNCT in pancreatic cancer. Notably, the outcomes of this thesis provide the first preliminary experimental data of the combination of CIRT and BNCT in a more representative, biologically accurate model, the 3D spheroids.

An introduction to the purpose of this work and its importance is provided in Chapter 1. Then, a theoretical framework follows in Chapter 2, including information about radioresistant solid tumors, advance radiotherapy treatment modalities, in particular BNCT and CIRT, and the preclinical models currently used in cancer research.
Chapter 3 presents the methodology followed for conducting the radiobiological experiments and the computational dosimetry.
The results of the analysis and a brief discussion are given in Chapter 4, followed by the conclusions and future directions in Chapter 5.

Chapter 2

Theoretical Framework

2.1 Radioresistant Solid Tumors

Cancer encompasses a large array of diseases originating in organs or tissues of the body and characterized by the uncontrolled growth of abnormal cells [22]. The development of cancer at a cellular level is termed carcinogenesis. During carcinogenesis, abnormal cells develop certain phenotypic traits that lead to their rapid, uncontrolled proliferation, and their ability to survive independently in specific microenvironments, resulting in tissue masses called neoplasms or tumors, and spreading them to other parts of the body, in a process called metastasis [23]. Such processes can be attributed to a combination of a person's genetic predisposition and environmental influences [24]. Radioresistant tumors are defined as malignancies that have either a poor or a negligible respond to conventional radiotherapy, due to a combination of their TME features and genetic radiosensitivity. They are characterized by intrinsic characteristics such as hypoxia, low cell proliferating fractions, and classical tumor escape hallmarks [13].

Hypoxia is a prevalent feature of solid tumors, defined as the TME's oxygen pressure levels below 10mm Hg, and it is significantly contributing to increased tumor aggressiveness, greater metastatic potential, and resistance to conventional therapies. This condition results from the increased demand for oxygen driven by the accelerated proliferation of tumor cells, coupled with an inadequate oxygen supply to cells and tissues due to the formation of a disorganized tumor microvascular network which is unable to compensate for the lack of oxygen [25].

Following the interaction of radiation with matter, water radiolysis generates reactive oxygen species (ROS), which are highly reactive and cause DNA damage. In a hypoxic environment, the lack of oxygen not only limits ROS formation but also prevents the fixation of damaged DNA into stable peroxides, allowing tumor cells to successfully repair the DNA lesions [26]. The magnitude of hypoxia-related radioresistance can be quantified by the oxygen enhancement ratio (OER), defined as the ratio of radiation doses needed under hypoxic versus normoxic conditions to achieve the same biological effect. In hypoxic regions, tumor cell survival rate against ionizing radiations (IR) is 2-3 times higher compared to normoxic areas [27].

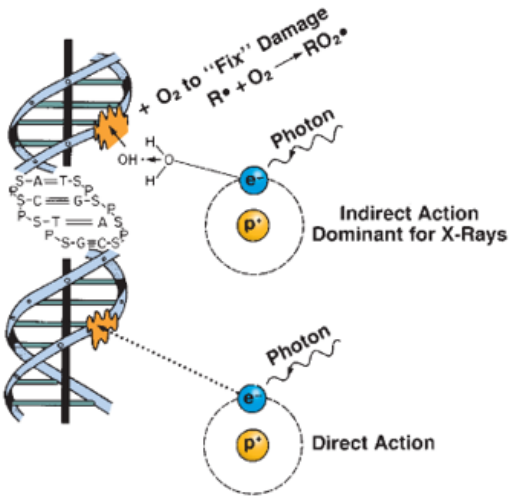


Figure 2.1: The oxygen fixation hypothesis. About two-thirds of the biologic damage produced by x-rays is by indirect action mediated by free radicals. The damage produced by free radicals in DNA can be repaired under hypoxia but may be "fixed" (made permanent and irreparable) if molecular oxygen is available [28].

2.1.1 Pancreatic Ductal Adenocarcinoma (PDAC)

Pancreatic ductal adenocarcinomas (PDAC), developed in the exocrine tissues of the pancreas, consists around 95% of pancreatic cancer cases, even though ductal epithelial cells constitute only 5% of the pancreatic tissue. Endocrine tumors, referred to as pancreatic neuroendocrine tumors (NETs), are much less frequent, and primary pancreatic nonepithelial tumors are extremely rare. [23], [29]

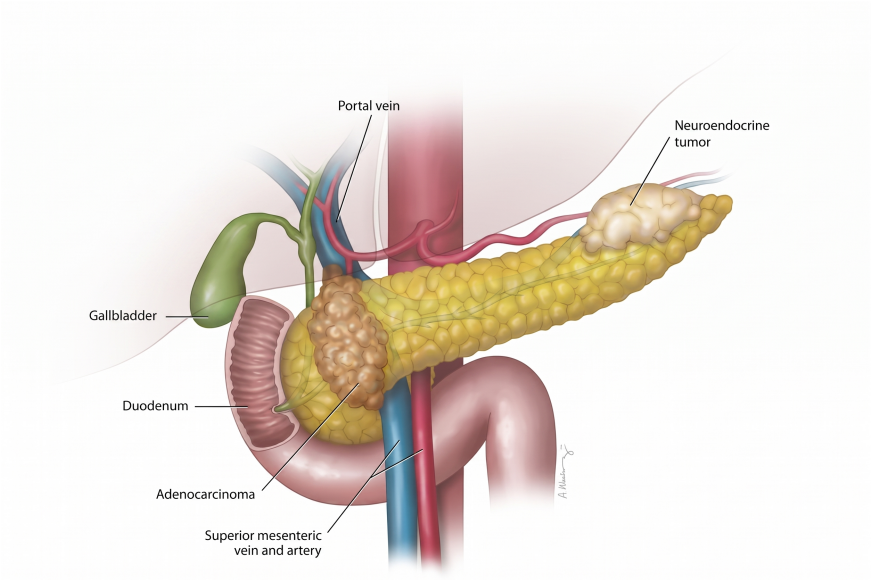


Figure 2.2: Anatomy of the pancreas including a ductal adenocarcinoma and a neuroendocrine tumor [30].

PDAC are classified as rare, radioresistant tumors [13], characterized by an immunosuppressive TME and significantly higher hypoxia levels compared to most solid tumors [12].

The pancreatic TME is composed of a dense extracellular matrix, a poorly formed vascular system, diverse populations of suppressive immune cells and a large number of fibroblasts [5]. This dense fibrotic tissue surrounding the tumor, known as desmoplasia, results in increased interstitial pressure and blood vessel compression [13], [12]. Combined with hypoxia, it amplifies its aggressively invasive behavior and metastatic phenotype, thus tumor cells often directly extend into the spleen, adrenals, stomach, and transverse colon [31]. In addition, it promotes tumor growth and hinders drug activity and penetration. From a genetic point of view, PDAC are characterized by substantial genetic heterogeneity, even within a single primary tumor, and combined with the existence of cancer stem cells ($\sim$1%), it contributes to an even more resistant tumor state [7]. Therefore, there is a clear requirement for aggressive multimodality therapy to tackle the unmet clinical demands of pancreatic cancer [32].

2.2 Advanced Particle Therapy Approaches

Conventional photon radiotherapy remains a default therapeutic modality, utilized in over 50% of all cancer treatments and for most solid tumors. However, its therapeutic efficacy is limited by unfavorable dose-depth distributions and oxygen-dependent cytotoxicity, which cause unwanted damage to healthy tissues. Particle radiotherapy overcomes these limitations through its superior physical and biological properties, enabling more precise, tumor-targeted energy depositions [14].

2.2.1 Carbon Ion Radiation Therapy (CIRT)

Carbon Ion Radiation Therapy (CIRT) is a form of Hadron Therapy that utilizes carbon ion beams instead of photons. The physical advantage of CIRT, lies in the energy loss rate of the ions, resulting in a depth-dose profile exhibiting a plateau region of minimal energy loss and a distinct peak near the end of the ions range, depicting a sharp increase in ionization due to a large energy deposition. This phenomenon is known as the Bragg peak. The narrow Bragg peak can be precisely positioned to the desired depth within the tumor volume, to maximize the dose at the target while sparing healthy tissues [33].

The parameter that describes the gradual energy loss of a charged particle propagating through an absorber is called stopping power. It depends on the properties of the absorbing medium (density, atomic number) as well as the particle's properties (mass, charge, energy). The overall stopping power (S) consists of the sum of two components. The collision stopping power (S_{coll}) that results from charged particle interaction with orbital electrons of the absorber and the radiation stopping power (S_{rad}) resulting from charged particle interaction with nuclei of the absorber [34], [35].

Therefore, the stopping power is defined by:

$$S(E) = \frac{dE}{dx} \implies S_{coll}(E) + S_{rad}(E) = \left(\frac{dE}{dx}\right)_{coll} + \left(\frac{dE}{dx}\right)_{rad} \tag{2.1}$$

with dE the amount of energy loss and dx the thickness of the material.

Regarding heavy charged particles, the energy loss is depicted in the following equation:

$$\frac{dE}{dx} = \frac{4\pi z^2 e^4}{mV^2} NZ \left[\ln\frac{2mV^2}{I} + \ln\frac{1}{1-\beta^2} - \beta^2 - \frac{C}{Z} - \frac{\delta}{2}\right](1+\eta) \tag{2.2}$$

where:

- dE/dx is the particle stopping power in units of MeV/cm,
- z is the charge number of the incoming particle,
- e is the elementary charge,
- m is the electron rest mass,
- V is the velocity of the incoming particle,
- β is the relative velocity of the particle ($\beta = V/c$),
- Z is the atomic number of the absorbing medium,
- I is the mean excitation potential of the absorber in units of eV,
- η is the correction parameter for quantum electrodynamics,
- N is the number of target atoms per unit volume in cm^{-3} ($N = \rho N_A/A$, where ρ is the absorber density, N_A is Avogadro's number, and A is the atomic weight of the absorber).
- C is the shell correction parameter ($0 \leq C \leq 1$),
- δ is the density effect correction parameter

Notably, the shell parameter C and the density effect parameter δ are particularly relevant at low or high energies, respectively.

Carbon ions demonstrate significantly steeper dose gradients than protons, combined with reduced lateral scattering due to their larger mass, resulting in an exceptionally sharp dose distribution border and superior dose conformity [14]. However, C-ions dose-depth profile exhibit a fragmentation tail at the end of their energy deposition, due to nuclear interactions along the beam path. The produced fragmentation ions and recoiled particles with a variety of LET are therefore producing different biological effects in the post-Bragg peak tail region [36].

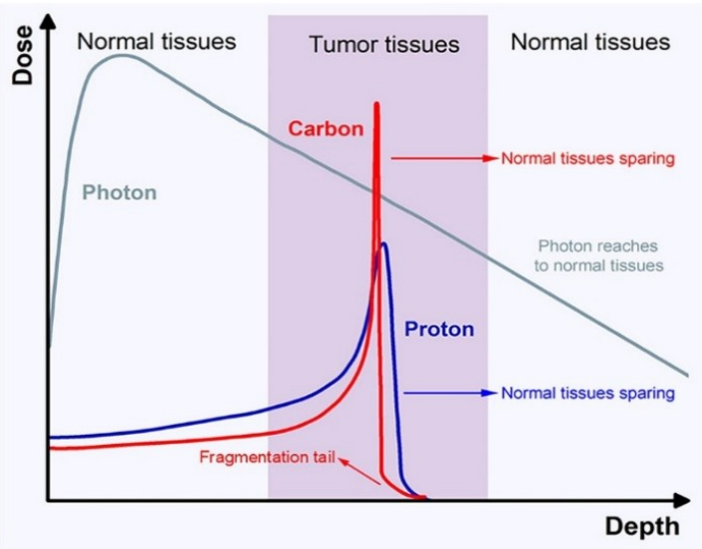


Figure 2.3: Comparative depth–dose profiles of photons, protons, and carbon ions [14]

.

In addition, CIRT offer distinct radiobiological advantages over both photons and lower-mass hadron therapies, like proton therapy (PT). These advantages are driven by their LET, defined as the amount of energy transferred to the tissues per unit of irradiation track length, that describes the ionization density, which is especially high for heavy, slow ions [12]. Firstly, while low-LET particles primarily induce repairable single-strand DNA breaks (SSBs) via oxygen-depended ROS, thus limiting their therapeutic efficacy in hypoxic and radioresistant tumors, high-LET carbon ions directly ionize DNA. This generates complex, clustered DNA double-strand breaks (DSBs), that are hard to repair and independent of tumor oxygenation. Secondly, the high LET results in a significantly higher RBE, maximizing treatment efficacy at lower fractional doses, hence offering the dosimetric advantages of greater dose to the target while sparing the surrounding OAR. Therefore, this combination of precise physical confinement and enhanced oxygen-independent biological damage sets CIRT as a promising modality for anatomically complex and hypoxic, radioresistant malignancies. [28], [14], [9]

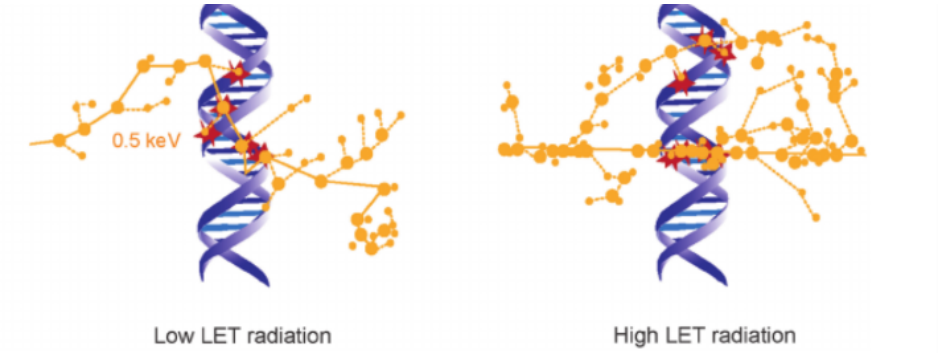


Figure 2.4: Distribution of DNA damage inducing ionization events along the particle tracks, after exposure to IR of low (0.5keV electrons) and high (4MeV alpha particles) LET. Large dots represent ionizations and small dots represent excitations. The tracks are simulated by Monte Carlo on the same scale as the DNA [37]

.

2.2.2 Neutron Capture Therapy (NCT)

Neutron capture reactions are nuclear reactions in which an atomic nucleus absorbs one or more neutrons, thus becoming a heavier and often unstable nucleus. The probability of interaction of the incoming neutrons with the target nuclei is quantified by the cross-section (σ), measured in barns. Based on that principle, Neutron Capture Therapy (NCT) is an experimental, non-invasive therapeutic technique designed to selectively target high-LET heavy charged particle radiation to tumors at the cellular level [38], directly inside the tumor. Being a binary, activation hadrontherapy modality, it relies on two components to achieve its therapeutic effect: a low-energy neutron beam and an isotope that selectively accumulates inside tumor cells in much higher concentrations than normal cells, has low toxicity, and exhibits a high cross-section for neutron capture. Each component is stable and non-harmful by itself, but when combined the effect is highly lethal [39], effectively achieving a biochemically targeted treatment, sparing healthy tissues, and transitioning the targeting precision standard from simple geometric localization to molecular recognition at the cellular level [14].

Presently, the two clinically approved agents that are available are sodium borocaptate

(BSH;$Na_2B_{12}H_{11}SH$) and boronophenylalanine (BPA;$C_9H_{12}BNO_4$) [40], both designed for Boron Neutron Capture Therapy (BNCT). BNCT is based on the nuclear capture decay that occurs when non-radioactive ^{10}B is irradiated with thermal neutrons of the appropriate energy to yield excited ^{11}B*, which undergoes an instantaneous nuclear reaction producing an alpha particle (^{4}He) and a ^{7}Li nucleus [39].

The nuclear reaction is given by:

$$^{10}\mathrm{B} + \mathrm{n} \longrightarrow {}^{11}\mathrm{B}^* \longrightarrow \begin{cases} {}^4\mathrm{He} + {}^7\mathrm{Li}^* \longrightarrow {}^7\mathrm{Li} + \gamma\,(0.478\,\mathrm{MeV}) \quad (94\%), \\ \\ {}^4\mathrm{He} + {}^7\mathrm{Li} \quad (6\%) \end{cases} \tag{2.3}$$

Both ^{4}He and ^{7}Li deposit their energy within the order of a few micrometers (5–9 μm), which is comparable to a mammalian cell diameter [41]. Therefore, the detrimental effect is strictly confined inside the target cells where ^{10}B has accumulated. Simultaneously, the mixed radiation field, characterized by different LET, amplifies the therapeutic effect. In addition, the high-LET products of the reaction are independent of oxygenation status, allowing the same effectiveness against tumor cells in normoxic and hypoxic environments, unlike conventional radiotherapy [42].

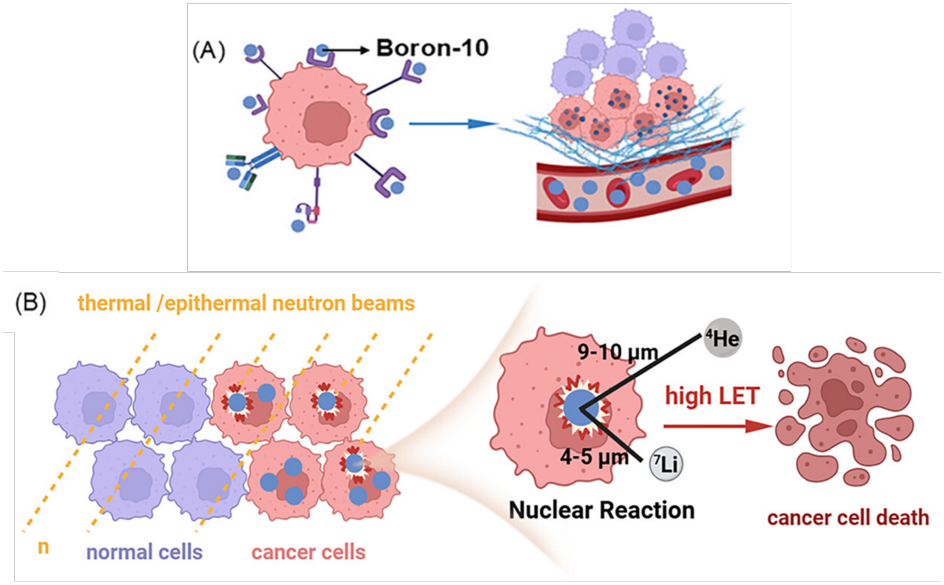


Figure 2.5: Schematic diagram of the dual targeting mechanism of BNCT. (A) Biochemical targeting: Selective accumulation of boron agents in cancer cells. (B) Physical targeting: Cellular-scale precision from neutron capture reactions [14].

Research into Gd- and Li-based NCT agents is also being actively conducted. For GdNCT, ^{157}Gd and ^{155}Gd isotopes are used due to their high thermal neutron cross-sections, both higher than ^{10}B, with ^{155}Gd possessing the highest value among stable isotopes in the periodic table [40]:

$$^{157}\mathrm{Gd} + \mathrm{n} \longrightarrow {}^{158}\mathrm{Gd}^* \longrightarrow \begin{cases} {}^{158}\mathrm{Gd} + \gamma & (31\%) \\ {}^{158}\mathrm{Gd} + \mathrm{ICE} + \mathrm{Auger}_{e^-} + \mathrm{X\text{-}rays} & (69\%) \end{cases} \tag{2.4}$$

In addition, Gd-based agents are already clinically approved as magnetic resonance imaging (MRI) contrast agents, implying that GdNCT agents could potentially serve as theragnostic platforms (ex. MRI-guided GdNCT) [43], [44], [45]

Furthermore, another element that holds significant interest for NCT is ^{6}Li:

$$^{6}\mathrm{Li} + \mathrm{n} \longrightarrow {}^{7}\mathrm{Li}^{*} \longrightarrow {}^{4}\mathrm{He} + {}^{3}\mathrm{H} \tag{2.5}$$

The products of this nuclear reaction are more energetic than those resulting from ^{10}B [46], yielding a reaction that is twice as exothermic, despite having a lower thermal neutron cross-section. The reaction does not emit gamma rays, resulting in a cleaner cellular-level dose; however, the ionizing range of the emitted tritium ions (^{3}H) exceeds that of BNCT by several cell diameters, requiring precise geometric and biological modeling in treatment planning [47].

Table 2.1: Q-values for thermal neutron capture in ^{10}B, ^{157}Gd, and ^{6}Li.

Isotope	Q**-Value**
^{10}B	2.31 MeV (94%)
	2.79 MeV (6%)
^{157}Gd	7.94 MeV
^{6}Li	4.78 MeV

Generally, two different neutron energy regimes are used in BNCT: thermal beams ($E =$ 0.005-0.5 eV), where therapeutic benefit is limited to shallow depths for superficial tumors such as melanoma, and epithermal beams ($E =$ 0.5-30 keV), where the penetration extends up to approximately 10 cm for deep-seated tumors [38]. Historically, nuclear research reactors were the primary source capable of delivering sufficient neutron flux (of the order of $10^{9} cm^{-2} s^{-1}$) for reactor-based BNCT (RB-BNCT). However, the past two decades have seen substantial advancements in hospital-based, accelerator-based neutron sources (AB-BNCT) [38].

2.2.3 Combination Therapy

Despite the favorable selectivity of BNCT and the physical dose conformality of particle therapies, single-modality treatments often fail to achieve durable local control in big, infiltrative, or radioresistant tumors. Specifically in the case of BNCT, recurrence after treatment has been linked to intrinsic limitations of boron delivery agents, including heterogeneous intratumoral boron distribution, incomplete coverage of the clinical target volume (CTV), and the dosimetric constraints of neutron beams [17]. In parallel, CIRT is dependent on macroscopic tumor targeting and constrained by the fragmentation tail, which deposits doses beyond the Bragg peak, to OARs or surrounding healthy tissues.

This has motivated a growing interest in multimodal combination strategies, with several being already under investigation. Combined PT-CIRT modalities have shown favorable toxicity profiles in inoperable osteosarcoma [48] and promising local control in stage I NSCLC [49], PT/CIRT-photon combinations have yielded encouraging results in gliomas and meningiomas [50], and Neutron Capture Enhanced Particle Therapy (NCEPT) has

been proposed as a way to exploit the thermal neutron field generated during proton or carbon ion treatment to further boost tumor dose via neutron capture agents [51].

Combining the cellular-level selectivity of BNCT with the precision of CIRT is particularly attractive because the two modalities are theoretically mechanistically complementary [16], since CIRT could target the tumor's hypoxic core and BNCT the metabolically active cells at the tumor margins [52]. This rationale was supported by an in-silico, effect-based treatment study in glioblastoma patients, through Monte Carlo simulations and treatment planning at software level, achieving a more homogeneous effect distribution within the CTV and the reduction of healthy tissue toxicity, suggesting its potential applicability for tumors characterized by pleomorphic, infiltrative, radioresistant, and voluminous features [53]. Collectively, these efforts support the feasibility and rationale of pairing particle therapy with neutron capture-based approaches.

2.3 3D Tumor Spheroids as a Radiobiological Model

Two-dimensional (2D) cell culture has been used as a prescreening tool for anticancer drug testing for over a century and remains the predominant preclinical method today [19], [54]. Despite being easy to use, has high throughput, and is cost-effective, they oversimplify in-vivo conditions, as they fail to replicate the cell-cell and cell-extracellular matrix (ECM) interactions of tumors, which are crucial for proliferation, metabolism, differentiation and function [18]. Moreover, processes such as morphogenesis, tissue remodeling, and cancer cell migration actively reshape the three-dimensional (3D) organization of the tumor microenvironment, a dynamic that 2D culture systems cannot replicate [55]. These limitations have driven a paradigm shift in cancer pre-clinical modeling towards 3D systems, which more faithfully reproduce in vivo tumor pathophysiology, therefore allowing a more accurate assessment of drug efficacy and toxicity [56], [19].

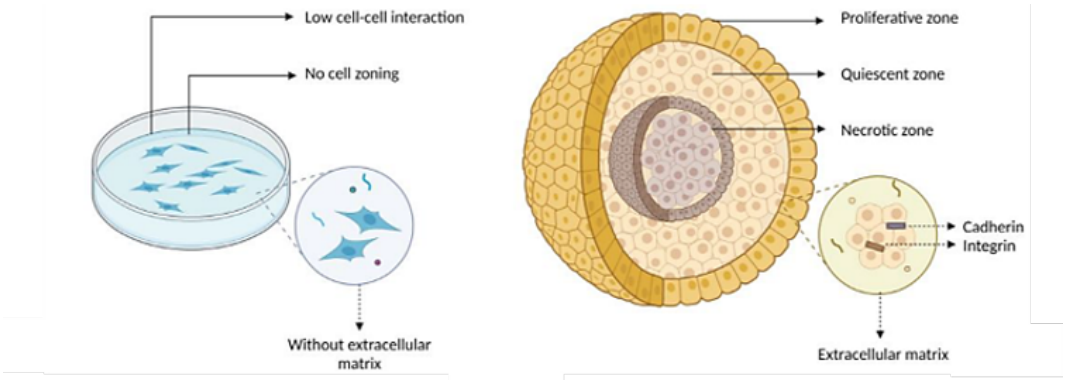


Figure 2.6: Diagram illustrating the characteristics of monolayer cell culture models and 3D spheroids, highlighting the unique features of each system. [57]

3D tumor spheroids are cancer cell aggregates formed by in-vitro 3D cell cultures. If grown beyond 400 µm, they develop gradients of oxygen, nutrients, pH, and growth factors that give rise to a characteristic multilayered architecture: an outer shell of proliferating cells, an intermediate layer of quiescent cells, and an inner core of hypoxic and necrotic cells resulting from limited molecular transport. This structure mimics the poorly vascularized regions and spatial heterogeneity typical of solid tumors, while also preserving cell-cell

and cell-ECM interactions and physiologically relevant growth kinetics [19], [54], [58], [59], [18]. As in human cancers, these features contribute to increased resistance to both chemotherapeutic agents and radiation, making spheroids a valuable model for studying how hypoxia, necrosis, invasion, and cell adhesion influence radiosensitivity and drug response [19], [54], [59]. Notably, 3D spheroids display greater apparent radioresistance than 2D cultures and support more physiologically relevant invasion assays [18]. Because 3D culture better captures the complex cellular organization and microenvironment found in in vivo tumors, it is now widely recognized as providing more reliable estimates of therapeutic response than conventional 2D culture [59]. Specifically for 3D PANC-1 spheroids, it was proven that they release significantly more exosomes with disease-relevant miRNA and protein profiles than 2D cultures, therefore showing more features relevant to the progression of pancreatic cancer and highlighting the potential importance of using spheroids as in vitro model to study cancer development and progression [60].

Nonetheless, spheroids derived from established cancer cell lines have important limitations as they do not capture the genetic and molecular heterogeneity of an individual patient's tumor, lacking key components of the native TME, including immune cells, stromal cells, and extracellular matrix elements [20]. This is a significant gap, as TME plays a critical role not only in carcinogenesis, tumor progression, and metastasis but also in affecting therapeutic efficacy [19]. A novel, promising alternative of single-cell spheroids tested for pancreatic cancer to mimic its complexity, is hetero-type multicellular tumor spheroids (MCTS), a 3D tumor model consisting of a triple co-culture of PANC-1 cells, fibroblasts and endothelial cells [61].

A promising alternative to spheroids is the use of patient-derived organoids (PDOs), 3D cultures generated directly from primary tumor biopsies. PDOs are increasingly applied in cancer research for understanding the pathophysiology of cancer progression and resistance, screening anticancer treatments in vitro, and modeling the specificity of an individual patient's tumor to enable personalized treatment selection [20].

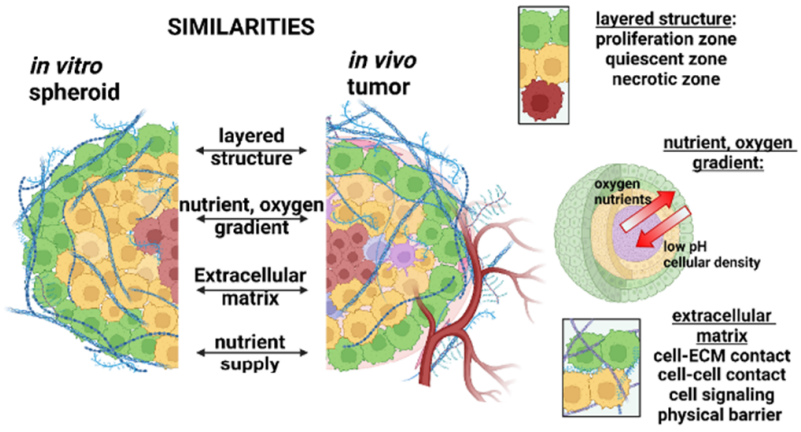


Figure 2.7: Scheme of similarities between in vitro spheroids and in vivo tumors, featuring the layered structure, the decreased availability of oxygen and nutrients for cells of deeper layers and cell-cell signaling and contact.[62]

Chapter 3

Materials and Methods

3.1 Computational Dosimetry

3.1.1 MCNP6 Simulations of the radiation dose delivered to the 3D tumor spheroids

The computational dosimetry part of the thesis was carried out using the Monte Carlo code MCNP6 (Monte Carlo N-Particle Transport Code) version 6.1. MCNP6 is a general-purpose, continuous-energy, generalized-geometry, time-dependent, Monte Carlo radiation-transport code designed to track many particle types over broad ranges of energies [63]. It has many applications, among others the design of nuclear reactors, radiation protection, high energy dosimetry and medical physics. MCNP6 is currently utilized for BNCT treatment planning, and it is considered as one of the most suitable codes for calculating accurately the BNCT dose distributions [38].

MCNP is a condensed-history code of radiation transfer in matter, grouping several interactions into a single step, based on stopping power data, where the deposited energy is scored. Compared to event-by-event codes, this method significantly reduces computational time, making it suitable for radiation transport simulations in complex geometries like reactors or radiation treatment rooms. Ultimately, the goal of the simulations is to obtain radiometric (e.g., fluence, current) and dosimetric (e.g., absorbed dose, KERMA) quantities in simulation volumes (cells) and surfaces, using standard computational tools, called by the MCNP software "tallies" [64].

3.1.1.1 Geometry of the 96-well U-bottom plate containing spheroids

For the composition of the PANC-1 spheroids, the material used was the average adult male healthy soft tissue according to ICRU-44 [65], a tissue-equivalent mixture with 13 elements of the human body. The density of pancreatic tissue was set as ρ=1.05 g/cm^3 [66]. However, for the necrotic core present in spheroids exceeding 200μm in diameter, the composition was adjusted to reflect the lack of oxygen and nutrients, as well as the accumulation of metabolic waste [67]. More specifically, by lowering the hydrogen and oxygen and increasing the carbon percentages. The density of the medium is equal to the density of water.

The complete list of elements that make up the spheroids, the plastic 96-well plate and the medium is shown in the following table:

Table 3.1: Elemental composition, nuclide identification number, and densities of the materials used in the simulation.

Material	**Density** [g/cm^3]	**Element**	**Nuclide Identification Number****	**Mass fraction** [%]
ICRU-44 soft tissue *(necrotic tissue)*	1.05	H	1001	10 (9)*
		C	6000	23 (25)*
		N	7014	2.30
		O	8016	63 (61)*
		Na	11023	0.13
		Mg	12000	0.015
		P	15031	0.24
		S	16032	0.22
		Cl	17000	0.14
		K	19000	0.21
		Fe	26056	6.3×10^{-3}
		Zr	40000	8.0×10^{-4}
		Pb	82207	1.6×10^{-5}
DMEM High Glucose non-complete	1.00	H	1001	10.97
		C	6000	0.24
		O	8016	87.94
		Na	11023	0.36
		P	15031	2.8×10^{-3}
		Cl	17000	0.43
		K	19000	0.02
		Ca	20000	7.21×10^{-3}
Polystyrene $(C_8H_8)_n$	1.06	H	1001	7.69
		C	6000	92.31

*Values marked with parentheses indicate the adjusted necrotic tissue composition.
**In MCNP coding, nuclides are identified by sequences of maximum 6 digits, the first referring to the atomic number (Z), the last three referring to the mass number (A), where the 000 set represent the natural isotopic abundance of a certain element.

The 96-well U-bottom plate was reproduced according to the company's product data sheet [68].

The simulated geometry is based on the detailed definition of a single well that includes the medium and the spheroid inside. Each well is defined as a cylinder merging with a hemisphere, to create the U-bottom. Wall thickness of the cylinder was set to $0.05cm$. The material used is polystyrene C_8H_8 with ρ=1.06 g/cm^3. The spheroid is composed of

a necrotic core (sphere of radius=281 μm) and a proliferating shell (concentric sphere of radius=335 μm). The two radii were acquired from the live/dead confocal microscopy imaging described in Section 3.2.2.2, with its results presented in Section 4.2.1.2. The well contains the spheroid, and the DMEM non-complete medium solution (200μl), so the level of the liquid inside the well was calculated by subtracting the volume of the spheroid from the volume of the DMEM.

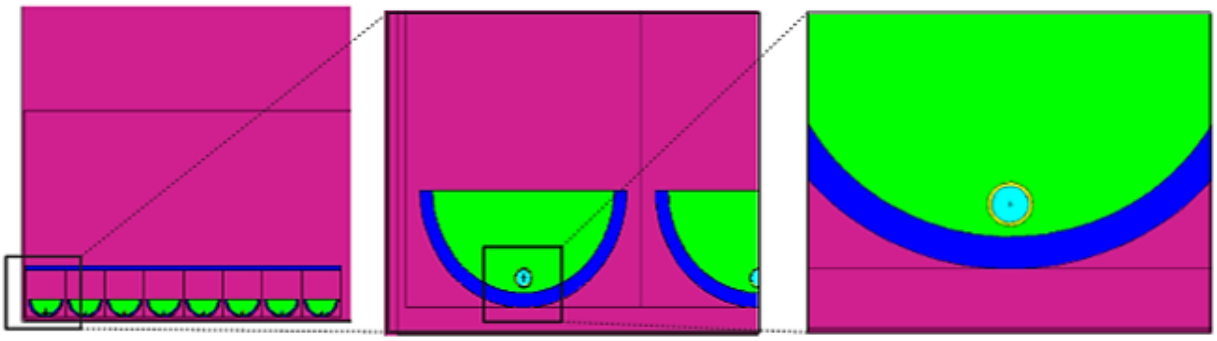


Figure 3.1: Multiscale view of the MCNP6 geometry model showing the 96-well plate setup (left), a single U-bottom well including the spheroid and DMEM (center), and a magnified view of the 3D concentric tumor spheroid structure featuring the necrotic core and the proliferating shell (right). [Magenta=air, green=DMEM medium, polystyrene=blue, yellow=proliferating tissue, light blue=necrotic tissue]

To get from a single well to the 96-well plate, a 2D lattice repeating the individual well unit in an 8-row by 12-column array and surrounded by an air gap around the structural matrix units was constructed. The matrix plate is enclosed within an external frame and a 0.1 cm polystyrene top cover.

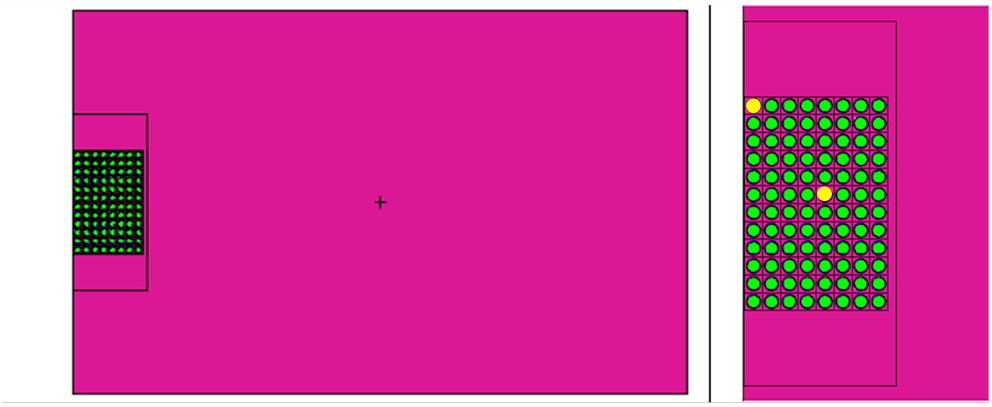
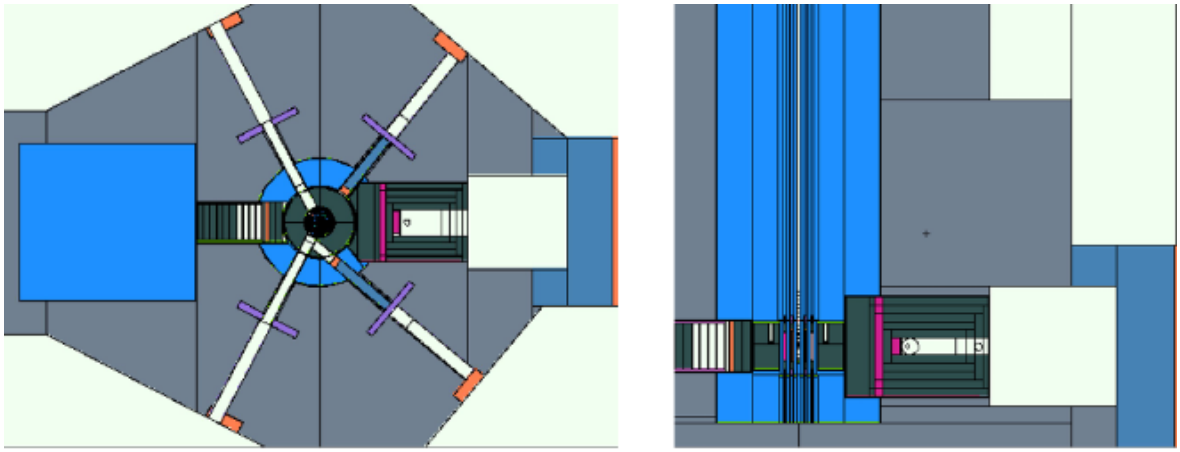


Figure 3.2: Top-down view of the MCNP6 model illustrating the complete thermal column irradiation cavity containing the translated source and the 96-well plate positioned at the beam entrance side (left) and a magnified view of the full 96 well-plate array containing the spheroids (right). The physical quantities were scored in the two cells marked with yellow. [Magenta=air, green=DMEM medium, polystyrene=blue]

3.1.1.2 Translated source and Target placement

For the simulations, the geometry of the UNIPV Triga Mark II reactor was used, which was previously built in MCNP and validated. The geometry is shown in Fig.3.3.



(a) (b)

Figure 3.3: 2D representations of the Triga Mark II geometry simulated with MCNP. (a) top view (b) lateral view. [Grey: concrete, dark grey: graphite, magenta: bismuth, blue: cooling pool, white: air] [64].

In a whole-reactor simulation, the radiation field is made up of both neutrons and photons. The primary neutrons can be generated by a KCODE criticality source, or by exploiting statistical distributions of the initial position, energy, and flight direction. In both cases the transport must cover a significant fraction of the whole reactor geometry, even though only a very small fraction of the histories ever reaches the region of interest, the target spheroids inside the thermal column, especially considering their microscopic sizes compared to the reactor. Hence, reaching adequate statistics would be very time consuming.

To overcome this limitation and optimize computational efficiency, a translated source was created. In a prior, validated simulation of the entire TRIGA Mark II reactor, a KCODE criticality source located in the reactor's core generated the neutron and photon fields, and the Surface Source Write (SSW) card available in MCNP code was used to score the phase space of the particles crossing a defined set of surfaces, storing them in an external file (WSSA) [64]. These surfaces form a virtual, rectangular volume (here and later named the "gamma box") placed at the irradiation position inside the thermal column and large enough to contain the target. When running the current simulation, the Surface Source Read (SSR) command allows to read the WSSA file and launches the same particles across the boundary surfaces of the gamma box directly towards the target, thus minimizing significantly the computational time.

The 96-well plates containing the spheroids were placed at position 1 (Fig.3.4), inside the thermal column of the TRIGA Mark II reactor, corresponding to a distance of 130.95 cm from the center of the reactor's core.

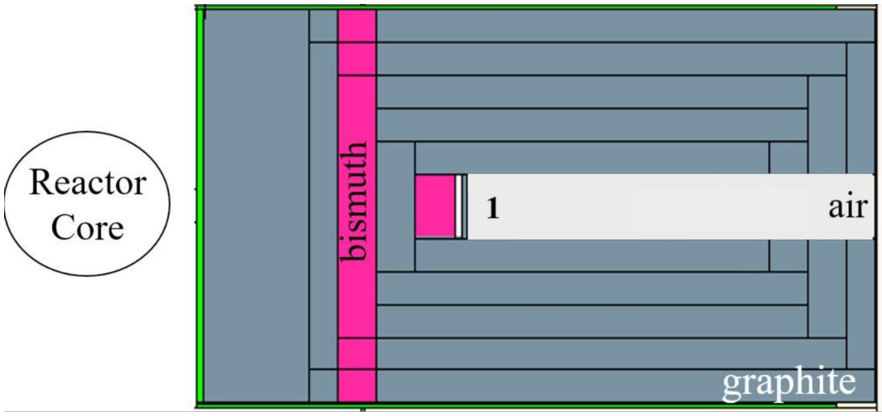


Figure 3.4: The thermal column of TRIGA II Mark reactor (longitudinal view). The samples were irradiated at position 1. [Grey: graphite, magenta: bismuth, green: boral (borated aluminium), white: air] [69].

3.1.2 BNCT Dose Components

The radiation field produced in BNCT consists of a mix of four distinct radiation components with different LET, hence different biological effectiveness [38]:

1. **Boron Dose (D_B):** high-LET, short-range charged particles (α particles and ^{7}Li ions) generated from the capture reaction ^{10}B(n, α)^{7}Li ($Q_{value} = 2.79MeV$). A long-range $0.478MeV$ γ is also emitted with a 94% probability.
2. **Nitrogen Dose (D_N):** intermediate-LET charged particles ($584keV$ protons and ^{14}C recoil nuclei) emitted by the capture reaction ^{14}N(n, p)^{14}C ($Q_{value} = 0.626MeV$).
3. **Hydrogen Dose (D_H):** intermediate-LET proton coming from the elastic scattering of fast and epithermal neutrons on the hydrogen of the body ^{1}H(n, n')p.
4. **Photon Dose (D_γ):** prompt γ (2.2MeV) from radiative neutron capture reactions ^{1}H(n, γ)^{2}H in the irradiation set-up and γ background contamination of the incident radiation field due to the activation of graphite [64].

Table 3.2: Comparison of thermal neutron (25meV) cross sections and Q-values of the main reactions of interest in BNCT dosimetry [70].

Reaction	σ [barns]	Q-value [MeV]
^{10}B(n, α)^{7}Li	3837	2.79
^{14}N(n, p)^{14}C	1.84	0.626
^{1}H(n, γ)^{2}H	0.322	2.2

3.1.3 Scored Physical Quantities

The irradiations in the thermal column were modeled assuming an operating power of the reactor of 60kW, corresponding to a source intensity of $I = (4.56 \times 10^{15})$ neutron/s in the core position [64]. Consequently, all dose rates results were normalized by this

factor. As MCNP normalizes the tally output per simulated particle history by default, the source factor is mandatory to have consistent predictions in the real world. Transport was simulated in "mode n p e" to simultaneously account for neutrons, photons, and electrons.

The tallies used in this simulation were F4 and *F8:

- **F4 Tally:** Evaluates the track-length estimate of the cell flux [particles/cm^{-2}], so the neutron fluence normalized by the number of primary particles (nps). It is defined as [71]:
$$F4 = \frac{1}{V}\int_V \int_t \int_E \Phi(\vec{r}, E, t)\, dE\, dt\, dV = \frac{W \cdot T_l}{V} \tag{3.1}$$
where: $\Phi(\vec{r}, E, t) = vN(\vec{r}, E, t)$ is the particle flux, v is the particle velocity, N is the particle density, V is the cell volume [cm^3], W is the particle weight, and T_l is the total track length [cm].
- ***F8 Tally:** F8 gives a Pulse Height, the energy distribution of the pulses created inside a cell that models a detector. Specifically, the *F8 variant was used, which records the energy deposited by charged particles inside the designated cell [MeV]. The absorbed dose is subsequently derived by dividing this energy by the cell mass [70].

For the dose components D_B, D_N and D_H, the reaction rates were calculated using the F4 tally coupled with the FM multiplier card, for neutrons or protons respectively.

The FM card modifies the flux tally, allowing you to determine the number of reactions per unit of nps and mass occurring in the cell of interest, assuming it is entirely made of a fictitious material:

$$\texttt{FM} \quad C \quad m \quad R$$

where m is the fictitious material number representing the target isotope where the process takes place, R is the interaction rate (the total number of processes x in a certain volume V), and C is the scaling factor converting reaction rates into absorbed dose [Gy/nps]:

$$C = N \cdot 10^{-24} \cdot Q \cdot 1.602 \times 10^{-10} \tag{3.2}$$

Here:

- $N = \frac{m \cdot N_A}{A}$ represents the number N of atoms in mass m of a certain element with atomic mass A, with N_A the Avogadro constant
- Q is the reaction Q-value in MeV as shown in table 3.2
- 10^{-24} is the numerical constant necessary to change barn in cm^2
- 1.602×10^{-10} is the constant to change MeV/g in J/kg=Gy.

In the case of charged particles production processes, under the assumption of charged particle equilibrium (CPE), the physical quantity calculated is a KERMA and it can be equated to absorbed dose (D_B, D_N). This condition is satisfied considering the short range of the secondary particles produced in these reactions, meaning all the energy produced in the reaction is deposited locally. Considering also that the ^{10}B concentration is assumed to be strictly confined within the proliferating shell (with a radius of 64 μm), there was no need for a secondary step transporting directly the α particles, ^{7}Li ions and protons. The calculated quantity is the energy transferred to charged particles due to the considered

reaction per gram of cells per source neutron [70]. Regarding D_H, the estimated quantity is the heating, the energy transferred by neutrons to hydrogen nuclei per cells gram per source neutron, due to elastic scattering processes. This quantity can be considered as a dose.

The physical quantities were scored separately in the two spheroid regions: the proliferating shell, where boron accumulation is assumed, and the necrotic core. To assess spatial variations across the 96-well plate, the same quantities were scored in a central well and in a peripheral well, as can be seen in Fig.3.2.

3.1.3.1 Total Absorbed Dose

The total absorbed physical dose D_{tot} delivered to the cells over an irradiation time t_{irr} at a reactor power P [kW] was calculated using the following equation: [70], [72]

$$D_{\text{tot}} = \left(R_{\text{bg}} + C_{\text{B}} \cdot R_{\text{B}}\right) \cdot t_{\text{irr}} \cdot \frac{P}{P_{\text{ref}}} \tag{3.3}$$

where:

- R_{B} is the dose rate from the $^{10}\text{B}(\text{n},\alpha)^{7}\text{Li}$ reaction per 1 ppm of ^{10}B [Gy/s].
- P_{ref} is the reference reactor power (250kW)
- C_{B} is the ^{10}B concentration in the target volume [ppm], determined experimentally via ICP-MS (Section 3.2.3.3).
- $P = 60$ kW is the irradiation reactor power
- R_{bg} is the background dose rate [Gy/s] resulting from the sum of the non-boron components:

  $$R_{\text{bg}} = R_{\text{N}} + R_{\text{H}} + R_{\gamma} \tag{3.4}$$

  with R_{N} the dose rate due to $^{14}\text{N}(\text{n},\text{p})^{14}\text{C}$ reaction, R_{H} the dose rate due to neutron elastic scattering on hydrogen, and $R_{\gamma} = R_{\gamma,\text{bg}} + R_{\gamma,2.2}$ encompassing both core background photons and capture gammas from $^{1}\text{H}(\text{n},\gamma)^{2}\text{H}$.

3.1.3.2 Survival Fraction (SF) as a function of the dose

The cells' post-irradiation survival was described using the Linear-Quadratic (LQ) model:

$$SF(D) = \exp\left(-\alpha D - \beta D^2\right) \tag{3.5}$$

where:

- SF is the surviving fraction at an absorbed dose D
- α [Gy^{-1}] represents the linear component corresponding to lethal, non-repairable lesions (predominant in high-LET radiation like α particles and ^{7}Li ions)
- β [Gy^{-2}] represents the quadratic component associated with sublethal damage (characteristic of sparsely ionizing low-LET radiation like photons and electrons).

The α/β ratio determines the dose at which the linear and quadratic cell-killing contributions are equal [64].

For in vitro studies, the survival curves are plotted on a semilogarithmic scale, with absorbed dose on the linear and surviving fraction on the logarithmic axis. For a fixed cancer cell line, the shape of the curves reflects the LET of the radiation: low-LET radiations, produces a curve that starts straight at low doses, bends at intermediate doses, and straightens again at high doses whereas high-LET radiations produce a linear curve with a constant slope.

3.2 Experimental Methodology

3.2.1 Cell Culture Models: 2D Monolayer and 3D Spheroids

For the in-vitro radiobiological experiments conducted, the human pancreatic ductal adenocarcinoma cell line PANC-1 was utilized, obtained from the Istituto Zooprofilattico Sperimentale della Lombardia e dell'Emilia Romagna (IZSLER, Cat. No. BS TCL 49). Originally isolated from the pancreatic duct of a 56-year-old white male with epithelioid carcinoma, it exhibits epithelial morphology and it is suitable for use in cancer research [73]. The PANC-1 cell line was chosen based on prior research conducted in Pavia, specifically combination treatments of BNCT and carbon ions in 2D monolayers [64], and comparative photon, proton, and carbon-ion studies in 2D and 3D spheroids models [9], which validated experimental feasibility and baseline radiobiological responses. Advancing this line of research, the present work transitions to a 3D spheroid model to investigate the therapeutic efficacy of combined BNCT and carbon-ion irradiation.

Cells were maintained in Dulbecco's Modified Eagle Medium (DMEM) high glucose with L-Glutamine (Dutscher, Ref. 509050) supplemented with 10% Fetal Bovine Serum (FBS), to add the necessary growth factors, and 1% penicillin-streptomycin (100 U/mL penicillin, 100 mg/mL streptomycin), antibiotics to reduce the contamination risk. Cultures were seeded in T-25 or T-75 flasks, depending on the experiment, and incubated under standard conditions: 37°C in a humidified atmosphere of 5% CO_2. The culture medium was replaced every second day. Once cultures reached a confluence between 70-90%, cells were passaged to prevent contact inhibition and maintain exponential growth.

The standard cell passage process was performed as follows:

1. The old medium was aspirated and discarded.
2. The cell layer was gently washed twice with sterile phosphate-buffered saline (PBS).
3. Cells were detached by adding 0.1% trypsin (Trypsin-EDTA) solution and incubating for approximately 2 minutes.
4. When detached, complete culture medium was added at twice the volume of trypsin used. The cell suspension was collected into a falcon and centrifuged at 150g for 9 minutes.
5. The liquid was discarded and the resulting pellet was resuspended in 1 mL of fresh complete medium.

6. Cell density was determined by using a Bürker chamber, after a 1:1 dilution with Trypan Blue to count the viable cells.
7. The calculated volume of cell suspension was reseeded into new flasks containing fresh complete medium at the target seeding density.

For the 3D spheroid formation, cells were maintained for at least 2 passages before seeding. Then, they were harvested via trypsinization, centrifuged, and resuspended in complete medium. Cells were seeded into 96-well U-bottom polysterene microplates (Greiner Bio-One, Cat. No. 650970) at a density of 2000 cells per well [72] [74], in an initial volume of 150 μL of medium. The plates were incubated under standard conditions (37°C, 5% CO_2). After 24 hours, an additional 100 μL of complete medium was carefully added to each well to achieve a final volume of 250 μL. This prevented the disruption of the fragile cell aggregates, when the spheroids were still forming. After that, half of the medium was refreshed every second day.

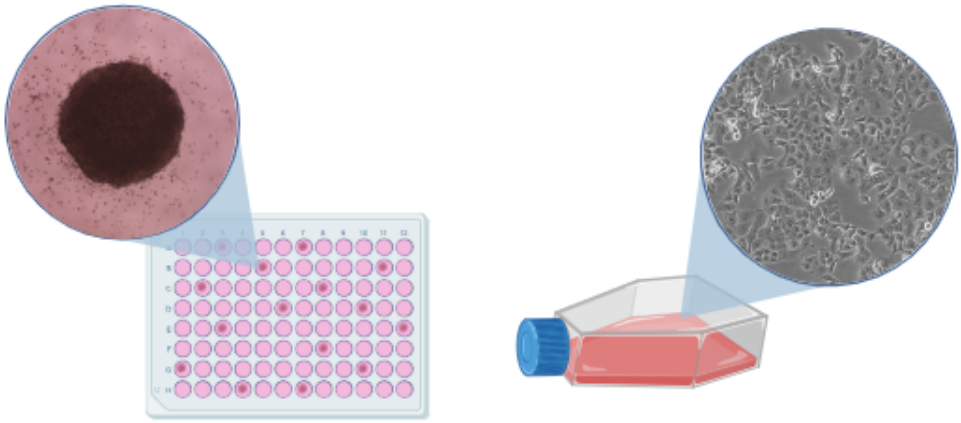


Figure 3.5: PANC-1 cell cultures: 3D spheroid in 96-well plate and 2D monolayer in T-75 flask. Created in BioRender.com.

3.2.2 Spheroid Characterization

This initial phase of the project was carried out during an Erasmus+ traineeship at the Department of Molecular and Interfacial Biophysics of the M.Smoluchowski Institute of Physics, at the Faculty of Physics, Astronomy and Applied Computer Science of the Jagiellonian University in Krakow, Poland. There, 2D PANC-1 cell cultures were initially developed, and subsequently the 3D PANC-1 spheroid models.

3.2.2.1 Size and Shape Assessment

3D PANC-1 spheroids were monitored daily using optical microscopy (Fig.3.6). The acquired images were processed and analyzed on Fiji (ImageJ) [75]. Spheroid growth and morphological integrity were quantified using the area and the derived radius as the size parameters, and circularity and solidity as the shape parameters. The results are presented in plots.

Circularity measures how close a shape is to a perfect circle, with maximum value of 1:

$$C = \frac{4\pi \cdot A}{P^2} \tag{3.6}$$

where A is the area and P the perimeter.

Solidity measures how compact a region is, with maximum value 1 for a completely convex shape:

$$S = \frac{A}{A_{\text{conv}}} \tag{3.7}$$

where A is the area and A_{conv} the area of its convex hull.

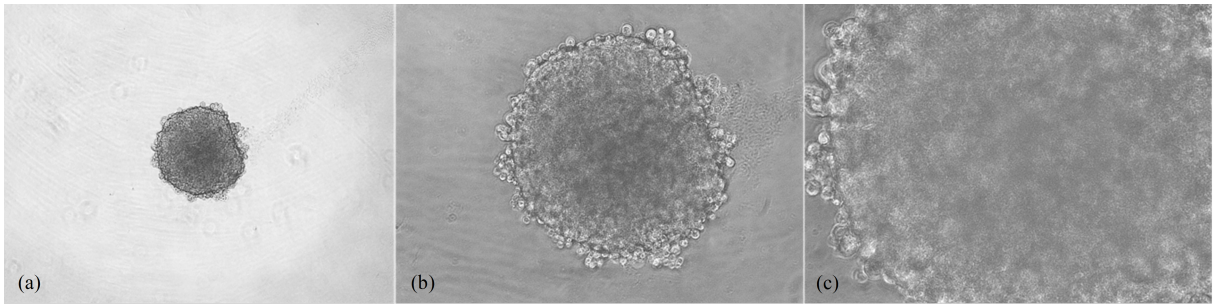


Figure 3.6: The same PANC-1 tumor spheroid on day 5 after seeding, with different magnifications: (a) x4, (b) x10, (c) x20.

3.2.2.2 Spheroid Imaging

Confocal images were acquired using a Zeiss LSM 710 confocal module set on Zeiss AxioObserver.Z1 inverted microscope (Carl Zeiss Microscopy GmbH, Jena, Germany). Combined with live/dead fluorescent staining, the confocal microscopy images were used to examine the internal morphology of the 3D PANC-1 spheroids by visualizing alive and dead cells.

Cell viability was evaluated using the Cellstain Double Staining Kit (Sigma-Aldrich, Cat. No. 04511). The assay relies on the simultaneous fluorescence staining of viable and dead cells, due to the Calcein-AM and propidium iodide (PI) solutions which stain viable cells green and dead cells red, respectively. More specifically:

- Calcein-AM is a highly lipophilic and cell membrane permeable compound. Although it is non-fluorescent, the calcein generated from Calcein-AM by esterase in a viable cell emits a strong green fluorescence (λ_{ex} 490 nm, λ_{em} 515 nm).
- PI is a fluorescent agent able to stain cells and nucleic acids, but unable to pass through a viable cell membrane. Upon compromise of the cell membrane, typically due to cell death, apoptosis, or damage, it can penetrate the cell an then intercalate with the DNA double helix to emit red fluorescence (λ_{ex} 535 nm, λ_{em} 617 nm).
- Since both calcein and PI-DNA can be excited with 490 nm light, simultaneous monitoring of viable and dead cells is possible with a fluorescence microscope.

The culture medium was aspirated from the wells of spheroids on day 8 post-seeding, which were then washed with PBS. After that, 100 μL of the dye solution, prepared

according to the manufacturer's protocol, was added to each well. Following a 15-minute incubation, individual spheroids were carefully transferred into glass-bottom dishes for fluorescence confocal acquisition.

Using these imaging results, the relative proportion of the proliferating outer shell compared to the necrotic core was calculated. The outer and inner radii of the spheroid were derived from the areas, measured using Fiji. The percentage of the shell volume was then calculated using the following formula:

$$\%_{\text{shell}} = \left(1 - \frac{V_{\text{c}}}{V_{\text{w}}}\right) \times 100 \tag{3.8}$$

where V_c is the volume of the spheroid's core and V_w the volume of the whole spheroid.

3.2.3 Boron Uptake Studies

3.2.3.1 BPA solutions preparation

For the BNCT experiments, ^{10}B-enriched boronophenylalanine (^{10}B-BPA or BPA) was employed as the ^{10}B delivery agent. Due to variations in laboratory protocols, two different preparation routes were adopted: a BPA-Fructose solution for the pre-irradiation investigations in Krakow, and a direct BPA dissolution in complete culture medium for the irradiations in Pavia. It was experimentally observed in previous studies conducted in Pavia [52], that the two methods did not show a difference in boron internalization in the samples or BPA solubility. Potentially, glucose in the DMEM medium acts similarly to fructose to enhance BPA solubility.

BPA-Fructose solution (protocol used for the experiments performed in Krakow):
The fructose solution (0.154M, 10% molar excess) was prepared by adding the weighted amount of fructose powder to H_2O. The required amount of BPA was then added, to reach a final concentration of 0.14M, and the solution was then mixed. To facilitate the dissolution of the BPA crystalline powder, NaOH (1M) was added to elevate the pH of the solution to approximately 10, vortexing in between. Once no particles were visible by naked eye, the pH was neutralized back to pH $\approx$ 7, by adding HCl (1M). The resulting solution was then sterilized by passage through a 0.22μm syringe filter and stored protected from light in the fridge. On the day of the experiment, this solution was diluted into DMEM to achieve the concentration of 8mM. [62]

BPA solution (protocol used for the experiments performed in Pavia):
For the in-vitro irradiation experiments conducted in Pavia, BPA was directly dissolved in DMEM without other agents. The mass of BPA powder (m_{BPA}) required to achieve the target concentration was calculated according to the following formula:

$$C = \frac{m_{\text{BPA}}}{M_{\text{BPA}}} \cdot \frac{1}{V_{\text{DMEM}}} \tag{3.9}$$

where:

- C is the target molar concentration (M),
- m_{BPA} is the weighed mass of ^{10}B-BPA powder (mg),
- M_{BPA} is the molar mass of ^{10}B-BPA ($= 208.21\,\text{g} \cdot \text{mol}^{-1}$),

- V_{DMEM} is the volume of DMEM used as the solvent (mL).

The weighted BPA powder was transferred into a 15 mL Falcon tube, where also the predetermined volume of DMEM was added. To facilitate the mixing of the solution, for practical convenience, the volume of the solvent was set to 15mL during the calculation of the m_{BPA}, as filling the tube near maximum capacity significantly reduced the formation of bubbles due to trapped air or foaming during the mixing process. The solution was mixed by a combination of mechanical agitation, alternating between vigorously manual shaking and vortex mixing, and thermal incubation, in a 37 °C water bath, until particles were no longer visible to the naked eye. The solution was then centrifuged to verify that the powder is indeed dissolved, if no residual undissolved solute was shown as a pellet. Finally, the solution was filtered through a 0.22μm filter, to ensure biological sterility, and was stored protected from light in the fridge [64].

3.2.3.2 Cytotocixcity of BPA

The cytotoxicity of the BPA solution in PANC-1 spheroids was quantified using the CyQUANT TM LDH Cytotoxicity Assay (Invitrogen, Cat.No. C20301) according to the manufacturer's protocol. This assay evaluates cytotoxicity by measuring lactate dehydrogenase (LDH), a cytosolic enzyme released into the extracellular medium, when the cell membrane is damaged, using colorimetric detection on microplate readers [76].

Samples were prepared as follows:

- BPA-treated LDH activity: spheroids after 2 and 4 hours of incubation with BPA-Fructose solution;
- Spontaneous LDH activity: spheroids in filtered, normal complete medium, acting as control;
- Maximum LDH activity: spheroids with 20 μL of 10X of lysis buffer added, acting as killed control.

After following the procedure of the manual, the absorbance was measured on a SPECTROstar Nano microplate reader, at λ=490nm substracting the background of λ=680nm.

To calculate the cytotoxicity the following formula was used:

$$\%\ \text{Cytotoxicity} = \left[\frac{\text{BPA-treated LDH activity} - \text{Spontaneous LDH activity}}{\text{Maximum LDH activity} - \text{Spontaneous LDH activity}}\right] \times 100 \quad (3.10)$$

3.2.3.3 Boron Uptake Studies in in-vitro 2D and 3D models

The intracellular distribution of ^{10}B within tumors is affected by the spatial organization of the cells, ultimately impacting the efficacy of the BNCT treatment [15]. Thus, examining the uptake difference between 3D spheroids and 2D monolayers is crucial.

Inductively Coupled Plasma Mass Spectrometry (ICP-MS):
To evaluate the ^{10}B uptake, 3D spheroids and 2D monolayers were analyzed on day 5 and day 6 post-seeding, respectively.

Following different incubation times with the ^{10}B-BPA solution, samples were collected, processed and prepared for ICP-MS, a gold standard method for ^{10}B quantification in BNCT.

In this method, the liquid sample is vaporized by a nebulizer and introduced into an argon plasma operating at temperatures up to 10,000 K. The plasma atomizes and ionizes the sample, to positively charged ions. These ions are sampled through a vacuum chamber consisting of a sampling cone and skimmer, to an ion optics system that focuses them into a quadrupole mass analyzer that separates the ions according to their specific mass-to-charge ratio (m/z). Finally, the separated ions are measure at an ion detector, which converts each physical ion impact into an electric signal. The resulting electrical pulse rate is directly proportional to the isotopic concentration of the target element in the original sample [77].

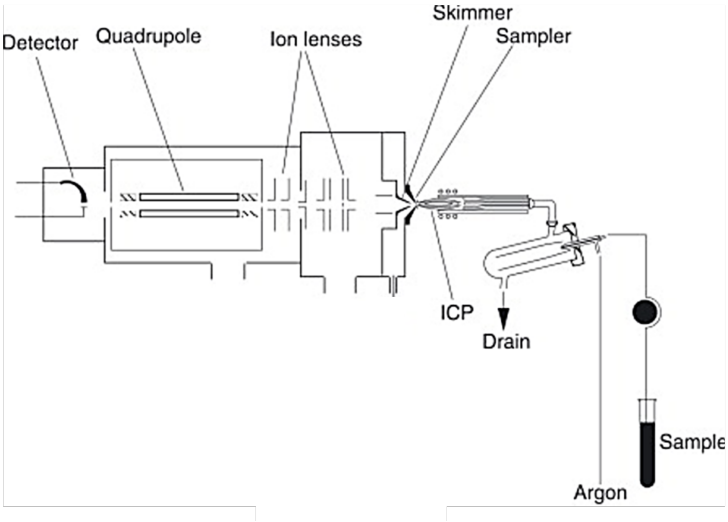


Figure 3.7: Schematic diagram of an inductively coupled plasma mass spectometer [78].

The sample preparation procedure is the following:

1. 2D monolayers and 3D spheroids were incubated under standard conditions (37°C, 5% CO_2) with 4 mM ^{10}B-BPA for either 2 h or 4 h. Controls were maintained in standard complete culture medium.
2. After incubation: 2D cell culture medium was aspirated and the cell monolayer was washed with PBS, detached using 0.25% trypsin, neutralized with fresh medium and centrifuged at 260 g for 10 minutes. The 3D spheroids with the incubation medium were transferred to falcons and centrifuged at 260 g for 10 min. Each falcon contained the spheroids collected from two 96-well plates, which is approximately 192 spheroids per falcon. After removing the liquid, the pellet was washed with PBS and transferred to a new 15mL falcon.
3. The cells and spheroids were then washed three times, by adding 1mL of PBS in each falcon followed by centrifugation at 300g for 5 minutes, to eliminate any extracellular BPA.
4. All the falcons used were weighted prior to sample addition. After the final PBS wash, the PBS was aspirated and the pellet's weight was calculated (by removing the initial weight of each empty falcon from the total final weight).
5. 1mL of concentrated HNO_3 was added in the pellet of each falcon under the fume hood and was left there for 1.5h, to stabilize elements in solution.

6. All falcons were then stored in refrigerated conditions (4 °C) until the ICP-MS analysis.

The measurements were conducted by the inductively coupled plasma mass spectrometer (Perkin Elmer Elan DRC-e) of the Laboratory of Analytical Atomic Spectrometry, Department of Analytical Chemistry, Faculty of Chemistry of the Jagiellonian University.

Qualitative Neutron Autoradiography:
A preliminary attempt to evaluate qualitative the spatial distribution of ^{10}B was performed on spheroids using neutron autoradiography, a well known technique for ^{10}B quantification in BNCT, particularly developed in the Physics Department of the University of Pavia. The spheroids were embedded in Optimal Cutting Temperature (OCT) compound, a water-soluble gel used to embed and freeze 3D biological samples for cryostat sectioning, to then use for the autoradiography.

Neutron autoradiography is a technique used to detect the presence of nuclei that absorb neutrons and release charged particles, employing a CR-39 Solid State Track Detector (SSTD). In this case, the alpha particles and Li-ions emitted from the capture reaction of the thermal neutrons with the ^{10}B, create latent tracks in the detector. Through optical microscopy, these tracks can be visualized and offer an indirect information on the amount and spatial distribution of the ^{10}B present in the sample.

To prepare the OCT-embedded spheroids the following protocol was followed:

1. The medium was removed from the wells of spheroids on day 5 post-seeding, and 100μL of BPA 4mM solution was added to each well. The 96-well plates were then incubated for 2 hours under standard conditions (37°C, 5% CO_2). For the control spheroids, the medium was replaced with fresh complete medium.
2. After the incubation, the spheroids were washed twice with PBS, fresh medium was added, were transferred in a 15mL falcon and centrifuged at 100 rpm for 10 minutes to avoid spheroids disgregation. Then, the supernatant was removed, and 50μL of fresh medium was added to resuspend the spheroids gently.
3. For the mixing of spheroids and the OCT two methods were developed:
   (a) 200μL of OCT gel was aspirated in a P1000 pipette cut tip. The spheroids were then aspirated with another pipette and dispensed directly in the tip containing the OCT, while mixing slightly.
   (b) 250μL of OCT gel was dispensed in the falcon containing the spheroids, while gently mixing. The mixture was then aspirated using a P1000 pipette cut tip.
4. The tips containing the OCT and spheroids (shown in Fig.3.8) were placed horizontally in contact with ice packs for fast freezing. After the OCT was frozen, the tips were stored at −20°C.
5. The samples were then cryosectioned (thickness: 60μm) at the Mario Negri Institute for Pharmacological Research (IRCCS) in Milan, Italy, using a Leica CM 1850 UV cryostat.

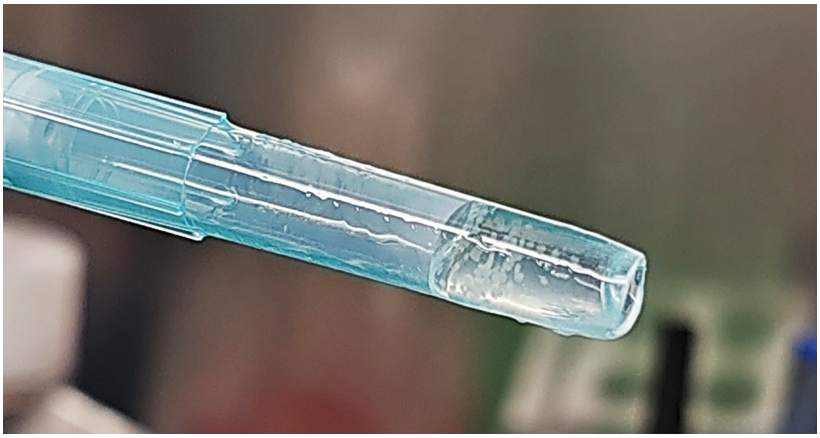


Figure 3.8: Spheroids embedded in an OCT matrix at room temperature.

The cell samples were deposited on CR-39 and dried either through air-drying at room temperature or by lyophilization. They were then irradiated in the thermal column of the TRIGA Mark II reactor of the University of Pavia for 2h with an estimated mean neutron flux of $(2 \times 10^9) n/cm^2 s$, at reactor power 250kW. After irradiation, the CR-39 was chemically etched using a NaOH 6.25N at 70°C for 15min, and subsequently washed with cold water. The chemical reactions induced by the solution are faster in correspondence of the damages, allowing a visualization of the tracks that become larger.

3.2.4 Irradiation Experiments

3.2.4.1 Radiation Facilities

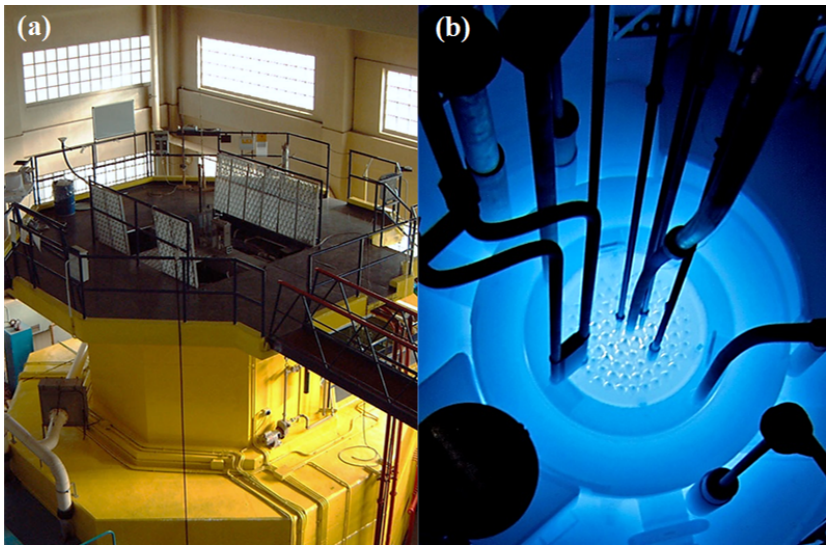


Figure 3.9: (a) The TRIGA Mark II reactor at L.E.N.A., Pavia. (b) Cherenkov light torch illuminating the reactor core when operating above 100 *kW.*

The TRIGA Mark II nuclear research reactor of LENA at the University of Pavia was installed in 1965. It is a pool-type reactor, cooled and partly moderated by light water. Its fuel consists of a homogeneous mixture of uranium and zirconium hydride, providing a prompt negative temperature coefficient. It operates at a maximum steady-state power of

250 kW [79], [80]. The neutron irradiation experiments of this thesis were conducted inside the thermal column of the reactor.



Figure 3.10: The thermal column (blue) of the TRIGA Mark II reator at LENA.

The carbon-ion irradiation experiments were carried out at the National Center for Oncological Hadrontherapy (CNAO) in Pavia. The CNAO synchrotron is designed as a ring with a 25-meter diameter and 80-meter circumference. It is the only center in Italy, and one of six worldwise, delivering both proton and carbon-ion hadrontherapy. Furthermore, through the ongoing collaboration between CNAO and TAE Life Sciences (TLS), and the PROGRESS BNCT@CNAO project, a neutron beam accelerator will be installed at CNAO in the near future, designed for clinical and research activities, making it potentially the first center in the world offering all three. [81]

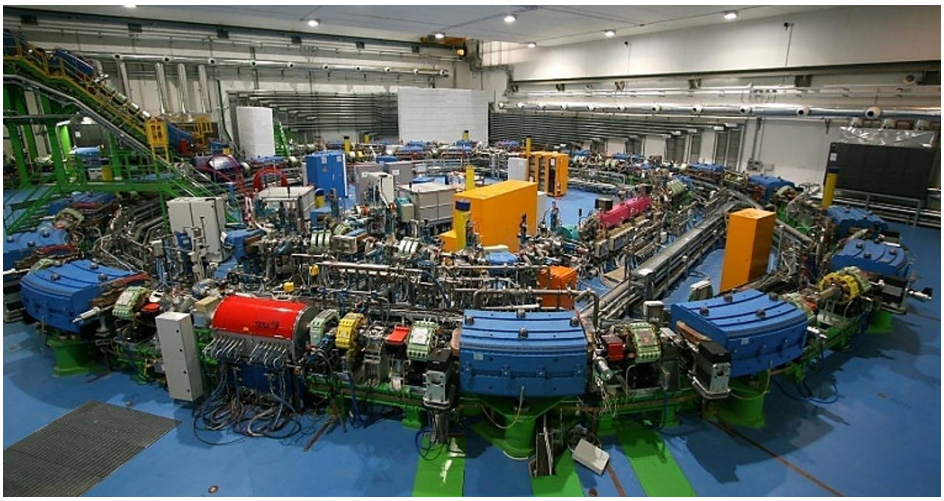


Figure 3.11: The CNAO hadrontherapy synchrotron facility in Pavia.

3.2.4.2 Sample Seeding and Pre-Irradiation Conditioning

Cells were seeded five days prior to exposure. For the 2D monolayer experiments, cells were seeded in T-25 culture flasks at a density of 70000 cells per flask, to achieve approximately 60% confluence on the day of irradiation. For the 3D tumor spheroid experiments, cells were seeded into 96-well U-bottom plates at a density of 2000 cells per well.

For the BNCT experiments, on day 5 post-seeding, the cell cultures were incubated with complete culture medium containing 4 mM ^{10}B-BPA for the planned amount of time. Control cultures were maintained in standard boron-free complete medium for matching incubation intervals. Following the BPA incubation, the medium was aspirated, and all flasks and wells were washed 3 times with PBS, to remove any extracellular boron.

Then, flasks and wells were completely filled with non-complete DMEM (20mL per T-25 flask, and 200μL per well). This is done in order to simulate better the dose-composition received by a tumor in a real patient, which has a lot of water equivalent material surrounding the tumor. Another reason, is to maintain as equal as possible the irradiation conditions of C-ions, in which the flasks are filled completely with ∼60ml, to satisfy CPE conditions during exposure:

$$(E_{\text{in}})_c = (E_{\text{out}})_c \tag{3.11}$$

where $(E_{\text{in}})_c$ and $(E_{\text{out}})_c$ are defined as the total kinetic energy of secondary charged particles entering and exiting the volume of interest, respectively. Since by increasing the volume of medium, the gamma dose is also increasing, the 20mL is adopted as an intermediate solution.

3.2.4.3 Irradiation Protocols

The non-irradiated control samples were prepared in the same manner and underwent identical conditions outside of the incubator as the irradiated ones.

Neutron Irradiations at LENA: Neutron exposure was conducted at a reactor power of 60kW. Two different irradiation experiments took place, as shown in Table 3.3. During the first one (BNCT1), samples were incubated for 2 hours with or without 4mM BPA and exposed to the thermal neutron field for 5min or 10min, including also a non-irradiated control. BNCT1 was a preliminary test of the biological effectiveness, thus only one biological replicate was used. On the other hand, for the second experiment (BNCT2), samples were evaluated across three biological replicates, meaning 3 groups of cells cultured independently for at least two passages prior to seeding, to accumulate more solid statistics. Exposure time of 5min following either 2h or 4h of BPA incubation were compared, alongside boron-free neutron controls (5min with no BPA) and non-irradiated controls (0min).

Carbon-Ion Hadrontherapy at CNAO: 2D monolayers and 3D spheroids were exposed to C-ion beams at doses of 0 (non-irradiated control), 1, 2, and 4 Gy, for three biological replicates each (a, b, c). The clinical beam was utilized with a spread-out Bragg peak (SOBP) by modulating energies between 246-312 MeV/u. The flasks and plates were placed in the middle of the SOBP, corresponding to a dose-averaged LET of about 45keV/μm.

Combined BNCT and C-ion Exposure: To evaluate the potential synergistic or additive effects between BNCT and C-ion radiotherapy, the dual-modality irradiation was executed as follows. On day 3 post-seeding, the cells received a 2Gy C-ion irradiation at CNAO. After a 50-hour window, on day 5 post-seeding, they were exposed at the LENA reactor under 5min neutron exposure following either 2h or 4h incubation with 4mM BPA, including also a control condition with 0min irradiation.

Table 3.3: Summary of the experimental irradiation conditions.

Experiment	BPA Incubation (4 mM)	Neutron Field (60 kW)	C-ion Dose
BNCT 1	—	0 min	—
	2 h	5 min	—
	2 h	10 min	—
BNCT 2	—	0 min	—
	2 h	5 min	—
	4 h	5 min	—
C-ion	—	—	0 Gy
	—	—	1 Gy
	—	—	2 Gy
	—	—	4 Gy
Combination	—	0 min	2 Gy
	2 h	5 min	2 Gy
	4 h	5 min	2 Gy

3.2.4.4 Post-Irradiation Analysis

2D cultures

After the radiation delivery, the irradiated medium was removed, cells were washed with PBS, harvested via trypsinization, and counted to seed the clonogenic survival assays.

Clonogenic Assays and Surviving Fraction: Clonogenic assay is an in vitro cell survival assay that quantifies the ability of a single cell to proliferate, growing into a colony, over a predetermined post-irradiation interval. A colony is defined as a group of at least 50 cells. Clonogenical death is defined as the permanent loss of a cell's capacity to divide indefinitely and produce a colony [82].

The assay involves plating cell suspensions at very low cellular densities into culture flasks, therefore after the viable cells were counted using the Bürker chamber with Trypan Blue 1:1 dilution, the required seeding volume was calculated and seeded in T-25 flasks with complete medium. Depending on the radiation dose received, cell numbers ranged between 250-1500 cells/flask, with cell numbers adjusted upward as a function of the delivered radiation dose to ensure statistically meaningful colony generation. Maintaining low initial density is critical to avoid colony overlap and ensure colony formation arises from isolated, single cells. When the required seeding volume was $< 100\,\mu$L, up to three consecutive 1:5 dilutions were performed (1 mL cell suspension into 4 mL medium) to keep the final pipetting volume within a reliable range between 100 and 1000 μL.

The flasks were gently agitated and then placed in the incubator, where they remained undisturbed for 10 days. At the endpoint, flasks were fixed using 2mL of ethanol 70% on each flask for 10 min. The ethanol fixes the cells and permeabilizes the cell membranes, allowing the dye solutions to penetrate into them. After removing the ethanol, 2mL of Giemsa dye was added in each flasks for 10 min. The dye was subsequently removed, and the plates were washed gently with distilled water 3 times and air-dried at room temperature. The colonies were then counted.

The plating efficiency (PE) is a standard method used to evaluate the clonogenic capability. After an incubation period T, the PE is determined according to:

$$\mathrm{PE} = \frac{N_{\mathrm{colonies}}}{N_{\mathrm{seeded}}} \tag{3.12}$$

where N_{colonies} is the number of scored colonies formed at time T, and N_{seeded} the initial number of seeded cells.

It is important to note that even for the control group this value is less than 100%, as cells undergo different types of stress, also during the plating efficiency protocol itself, in processes such as centrifugation or also cell seeding in such low density in a flask.

The surviving fraction (SF) at a given physical dose D is normalized to the non-irradiated control:

$$\mathrm{SF}(D) = \frac{\mathrm{PE}(D)}{\mathrm{PE}(0)} \tag{3.13}$$

where PE(0) represents the plating efficiency of the unexposed control (0 Gy or 0 min).

The SF curve with respect to the dose was then plotted for every irradiation type and fitted to the linear-quadratic model as described in Eq.3.5.

3D Spheroids

Immediately following radiation delivery, the irradiated medium was completely removed and replaced with 200μL of fresh complete culture medium per well. Plates were then returned to the incubator (37 °C, 5%CO_2), and they were being followed for 10 days after irradiation, by pictures taken using optical microscopy. The acquired images were then processed and analyzed using macros on Fiji. To visualize the effect that each irradiation condition had on the size of the spheroids over time, the graph of the radius with respect to the days after irradiation was plotted for each condition. All values were normalized by the measurements of the day before irradiation, to ensure the results were not absolute but relative to the initial size of the samples, accounting for the natural variability in dimensions observed in biological specimens [83].

The percentage of the size regression of the spheroids, based on measurements of the radius (R), and the percentage of boron enhancement between the same conditions with and without BPA, were calculated using the following formulas:

$$\%_{\mathrm{regression}} = \left(1 - \frac{R_{\mathrm{final\ day}}}{R_{\mathrm{day-1}}}\right) \times 100 \tag{3.14}$$

$$\%_{\mathrm{B\text{-}enhancement}} = \left(1 - \frac{R_{\mathrm{norm\ (BPA)}}}{R_{\mathrm{norm\ (n)}}}\right) \times 100 \tag{3.15}$$

where $R_{\text{final day}}$ is the radius on the final day of following the spheroid post irradiation, $R_{\text{day}-1}$ is the radius on the day before irradiation, $R_{\text{norm (BPA)}}$ the normalized radius for spheroids treated with BPA and $R_{\text{norm (n)}}$ the normalized radisu for spheroids exposed to neutron irradiation without prior BPA incubation.

3.2.4.5 Statistical Analysis

Statistical analysis was performed using a one-way ANOVA, followed by Tukey's HSD post-hoc test for multiple pairwise comparisons. Adjusted p-values are reported as: * $p < 0.05$, ** $p < 0.01$, and *** $p < 0.001$. All the statistical tests were performed using the open source software R, version 4.6.1.

Chapter 4

Results and Discussion

4.1 Computational Results

The dose rates results explained in Section 3.1.3, for all dose components, are presented in the following table:

Table 4.1: MCNP6 simulation dose rates results and associated relative errors scored in 3D tumor spheroids irradiated in the thermal column of the Pavia TRIGA Mark II reactor.

Dose Component	**Spheroid Region**	**Center Well**		**Edge Well**	
		Dose [Gy/s]	**Rel. Err.**	**Dose [Gy/s]**	**Rel. Err.**
D_{B} (per 1 ppm of ^{10}B)	Core	3.38×10^{-4}	3.83%	3.87×10^{-4}	3.70%
	Shell	3.44×10^{-4}	3.50%	3.19×10^{-4}	3.19%
D_{N}	Core	6.98×10^{-4}	3.83%	8.01×10^{-4}	3.70%
	Shell	7.12×10^{-4}	3.50%	7.87×10^{-4}	3.19%
D_{H}	Core	0.45×10^{-4}	11.09%	0.53×10^{-4}	9.96%
	Shell	5.10×10^{-4}	92.07%	0.50×10^{-4}	11.30%
$D_{\gamma}{}^{*}$	Core	3.31×10^{-4}	17.89%	2.36×10^{-4}	26.53%
	Shell	3.19×10^{-4}	25.61%	2.21×10^{-4}	26.41%

[*] Converted from total deposited energy scored via tally `*F8` (MeV/particle) using the respective mass ($m_{\mathrm{core}} = 9.759 \times 10^{-5}$ g, $m_{\mathrm{shell}} = 8.459 \times 10^{-5}$ g).

It is observed that there is a difference in the dose rates received across the plate geometry, as the dose rates of the edge well, that is closer to the lateral walls of the thermal column cavity, tend to be higher for D_B and D_N, compared to the central well. The increased doses could be attributed to the higher flux, as the in-air neutron flux is less attenuated on the edges of the plate compared to the central region. This was shown in [79], by the parabolic profile exhibited of the thermal neutron flux in tissue equivalent material, after measurements conducted in the thermal column of the Triga Mark II reactor, validated by MCNP simulations.

From the dose rates of table 4.1, the total doses were calculated using Eq.3.3. The boron concentration values from the ICP-MS results (table 4.3) were used for the calculations. For the proliferating shell the boron concentration used was normalized using Eq.4.1,

assuming that the boron concentration is strictly accumulated within it. For the necrotic core, the boron concentration of the control sample with no BPA was used, following the same assumption.

Table 4.2: Total absorbed dose calculation results (D_{tot} ± SD in Gy).

Spheroid	**Well**	**Neutron**			**Neutron + BPA**			
Region	**Position**	**0m_n** [Gy]	**5m_n** [Gy]	**10m_n** [Gy]	**0m_2hBPA** [Gy]	**5m_2hBPA** [Gy]	**5m_4hBPA** [Gy]	**10m_2hBPA** [Gy]
Shell	Center	0 ±0	0.5 ±0.1	0.9 ±0.3	0 ±0	0.7 ±0.1	0.8 ±0.1	1.4 ±0.3
	Edge	0 ±0	0.32 ±0.02	0.63 ±0.04	0 ±0	0.59 ±0.02	0.69 ±0.02	1.19 ±0.04
Core	Center	0 ±0	0.32 ±0.02	0.64 ±0.04	0 ±0	0.32 ±0.02	0.32 ±0.02	0.65 ±0.04
	Edge	0 ±0	0.33 ±0.02	0.65 ±0.04	0 ±0	0.33 ±0.02	0.33 ±0.02	0.66 ±0.04

The doses of the samples without BPA, are slightly increasing with irradiation time, establishing the background radiation baseline of the experiments. Compared with the spheroids irradiated with the neutron beam for the same amount of time but following BPA incubation, the doses of the latter are higher. There is also a slight increase observed with the BPA incubation time.

It should be noted that, while computational dosimetry was performed at representative edge and central wells, the spheroids analyzed were distributed across the entire 96-well plate. Consequently, this spatial dose inhomogeneity is averaged out across all wells, and it contributes to the overall experimental uncertainty of the results.

4.2 Experimental Results

4.2.1 Spheroid Characterization

4.2.1.1 Size and shape assessment

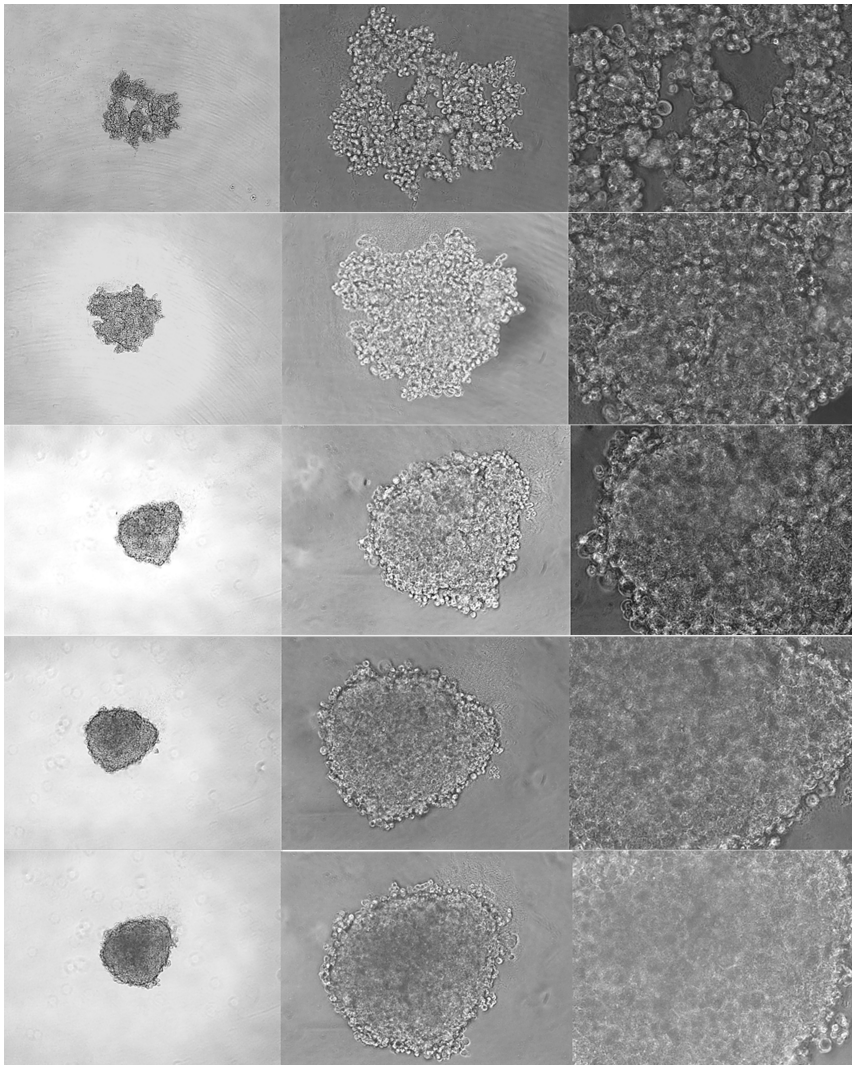


Figure 4.1: PANC-1 tumor spheroid on days 1-5 after seeding, with different magnifications (x4, x10, x20).

Shown in Figure 4.1, is the same PANC-1 spheroid monitored over five consecutive days after seeding, with three different magnifications. The apparent differences in orientation between the acquisition days are due to possible rotational variations during the repositioning of the camera.

Over the five-day observation period, the cell cluster exhibits progressive compaction, developing a rounder, more regular geometry with increasingly defined outer margins. Concurrently, the core becomes visibly darker due to the heightened cellular density, and there is a gradual loss of distinguishable single-cell boundaries. After its compaction into a solid shape, in day 3 post-seeding, we observe a gradual increase of the spheroid's size.

Quantifying the observations of the followed spheroids, Figures 4.2 and 4.3 were plotted.

Unless otherwise specified, lines connecting discrete data points in all plots in this section are intended as visual guides to the eye and do not represent theoretical fits.

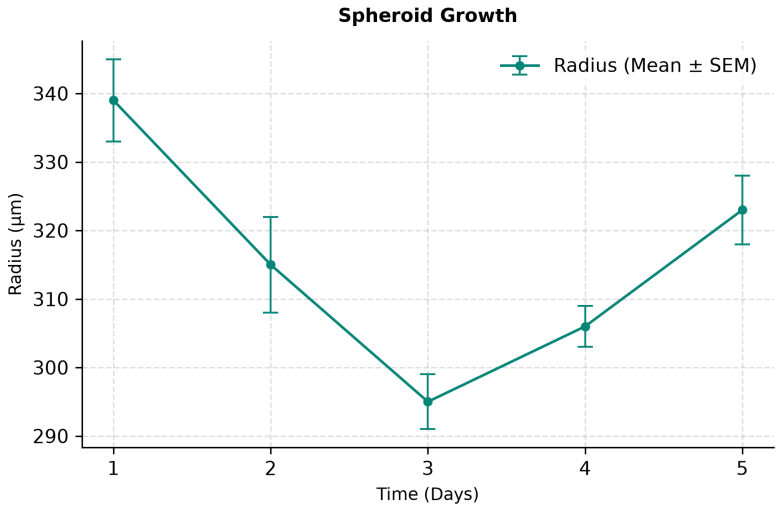


Figure 4.2: Spheroid radius sizes over 5 consecutive days from the day of seeding.

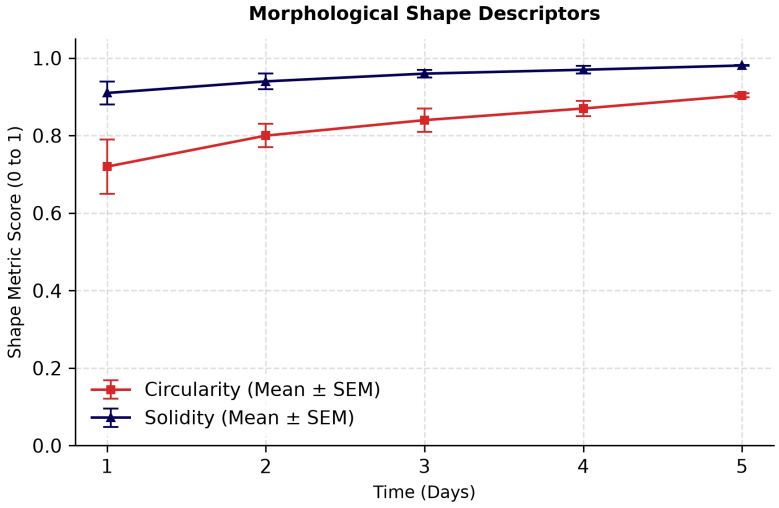


Figure 4.3: Spheroids shape parameters (circularity and solidity) over 5 consecutive days from day of seeding.

Over the first three days, the radius sizes of the spheroids, derived from the surface area measurements, are shrinking steadily, showcasing the compaction. After day 3 post-seeding, the spheroid radii start increasing. Simultaneously, both circularity and solidity (Eq. 3.6, 3.7) are progressively increasing. This pattern indicates that the loose, irregular clusters of cells exhibited in the initial days of seeding, gradually reorganized into a denser, smoother, and more spherical mass.

The suggested range of diameters for conducting experiments with spheroids is (300–500)μm [74]. Based on the data acquired at this stage, we conducted the following irradiation experiments with spheroids at day 5 post-seeding.

4.2.1.2 Spheroid Imaging

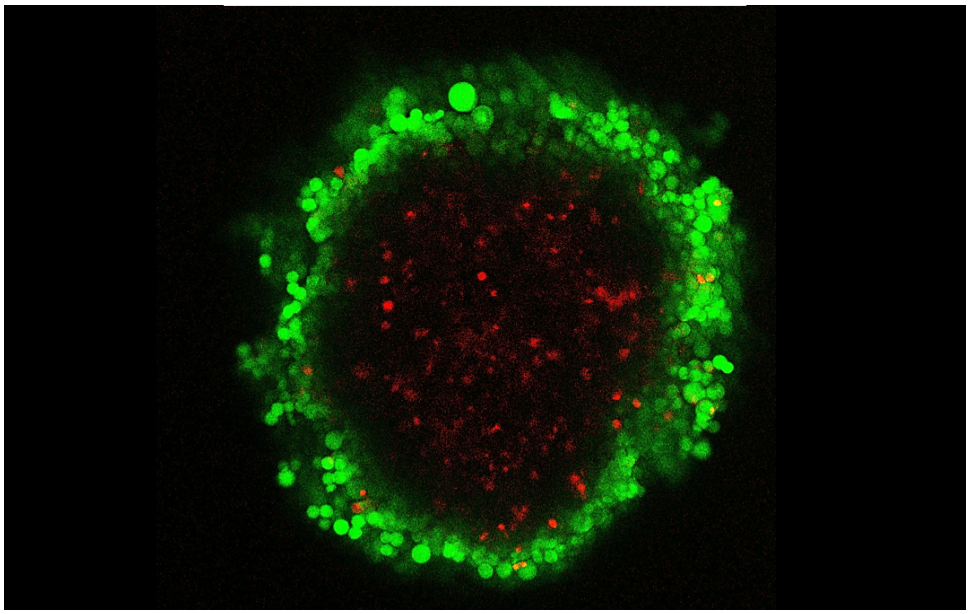


Figure 4.4: Confocal laser scanning microscopy of a PANC-1 spheroid, combined with live/dead fluorescent staining. Captured at 10x magnification.

The resulting imaging confirmed a viable outer shell of proliferating cells surrounding a necrotic core, a characteristic feature of spheroid models and an indication of their increased physiological relevance compared to conventional monolayer cultures.

It should be noted that the Fig.4.4 does not show the entire spheroid structure, but only a layer of cells. To show this, a 3D representation of the spheroid is depicted below:

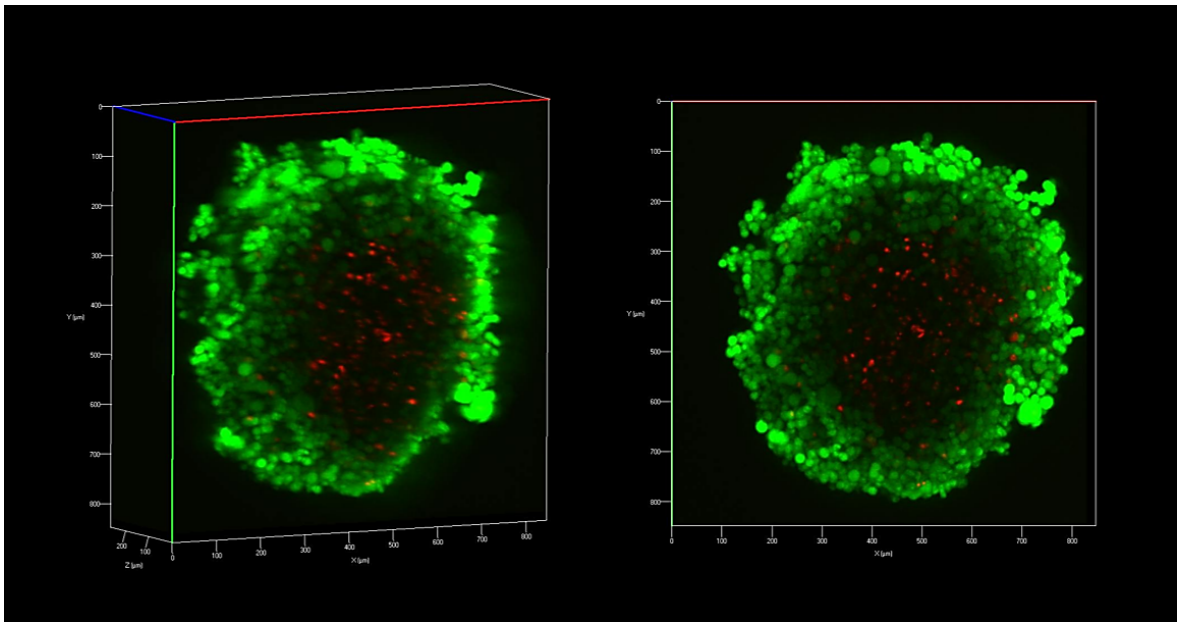


Figure 4.5: 3D representation of a PANC-1 spheroids after confocal laser scanning microscopy, combined with live/dead fluorescent staining. Captured at 10x magnification.

The percentage of the proliferating outer shell compared to the necrotic core was calculated as (46±14)%, using Eq.3.8, with the radius of the whole spheroid measured as (346±1)μm and the radius of the necrotic core as $(282 \pm 1)\mu m$.

A direct measurement of the core and total radii in Fiji provided a baseline fraction of (46±1)%. However, comparative analysis revealed that the segmented volume is substantially dependent on the binarization cutoff and the selected z-stack slice. To avoid underestimating systematic errors from methodological variances, the uncertainty was set to ±14%, corresponding to the maximum deviation observed across independent segmentation approaches, reflecting the calculated volume's sensitivity of the proliferating shell boundary definition.

These results were used during the MCNP6 simulation, to construct the geometry of the simulated spheroids.

4.2.2 Boron Uptake Studies

4.2.2.1 Cytotoxicity of BPA

Mean absorbance values for spheroids incubated with BPA for 2h and 4h were identical (0.125 ± 0.003 and 0.125 ± 0.002 respectively) and matched the value of the untreated control (0.125±0.002). These results confirm that BPA alone does not induce any cytotoxic damage or compromise cell membrane integrity during the typical pre-irradiation uptake period. However, relative percentage cytotoxicity could not be calculated using Eq. 3.10 because the maximum-LDH activity killed control, treated with the lysis buffer, failed to achieve complete cell death (0.15 ± 0.01), even though it is stated in the manual that the test can be used in 3D cell models. This limitation stems from the tight intercellular junctions and dense extracellular matrix characteristics of 3D spheroids, which restrict compound penetration and hinder the diffusion of intracellular LDH into the culture medium. Nonetheless, the results definitely demonstrate the non-toxic profile of BPA prior to neutron irradiation. Further replicas and tests are currently undergoing, in particular to evaluate possible mechanical dismantling processes on the spheroid structure before the reagent treatment to better allow its penetration in the whole cell population.

4.2.2.2 Boron Uptake Studies in in-vitro 2D and 3D models

Inductively Coupled Plasma Mass Spectrometry (ICP-MS):
The quantification of ^{10}B uptake by ICP-MS revealed significant differences between 2D and 3D models, as shown on Table 4.3. In 2D monolayers, boron concentrations reached $(15.09 \pm 0.05)\mu g/g$ at 2h, and were increased by $\sim$ 10% up to $(16.56 \pm 0.06)\mu g/g$ at 4h. Generally, the concentrations were a bit lower than the sufficient quantity for effective therapeutic treatment ($\approx 10^9$ ^{10}B atoms/cell or 20 μg/g of tissue [84]). On the other hand, 3D spheroids exhibited boron levels of $(1.12 \pm 0.02)\mu g/g$ and $(1.51 \pm 0.02)\mu g/g$ measured at 2h and 4h, respectively. While 3D uptake was time-dependent, showing a $\sim$ 36% increase from 2h to 4h, the overall accumulation was approximately an order of magnitude lower than in monolayers.

Table 4.3: ICP-MS results of ^{10}B uptake in 2D cell monolayers and 3D tumor spheroids following BPA incubation.

Culture Model	Condition	Sample Mass [g]	^{10}B Conc. [μg/g]	SD [μg/g]	SEM [μg/g]
2D Monolayer	Untreated Control	0.0845	0.000	—	—
	2 h BPA	0.0805	15.09	0.07	0.05
	4 h BPA	0.0980	16.56	0.09	0.06
3D Spheroid	Untreated Control	0.0580	0.006	—	—
	2 h BPA	0.0335	1.12	0.03	0.02
	4 h BPA	0.0340	1.51	0.03	0.02

The apparent discrepancy between the ^{10}B concentration observed in 2D monolayers and 3D spheroids reflects the critical role of the 3D architectural barriers, including restricted diffusion and poor transport within an organized tumor architecture, and highlights how 2D assays overestimate boron carrier delivery relative to solid tumor tissue.

Cellular uptake of BPA is mainly dependent on the L-type amino acid transporter 1 (LAT1, SLC7A5) [85]. LAT1, is a cell membrane transporter of essential amino acids [86], demonstrating an overexpression in multiple tumors due to the increased need for amino acids from proliferating tumor cells, including pancreatic cancer [87]. Regarding 3D PANC-1 spheroids, live/dead fluorescence imaging (Section 3.2.2.2), demonstrated PI accumulation restricted to the central core, confirming loss of membrane integrity and necrosis. Therefore, it is reasonable to assume that LAT1 function is compromised in the core, due to the non-intact cell membranes. Hence, the direct accumulation of ^{10}B is assumed to be effectively confined to the viable, proliferating outer shell, where it can be transported via the LAT1. Consequently, the ICP-MS measurements underestimate the real values within viable cells, as in the spheroids case the sample is not homogeneous, and the analysis averages the boron mass over the entire spheroid volume, diluting the apparent concentration across the non-accumulating necrotic core.

To account for this assumption, that active BPA internalization is strictly localized to the viable outer shell and negligible in the necrotic core, the effective ^{10}B concentration in the shell (C_{shell}) was estimated by normalizing the ICP-MS concentration by the measured shell volume fraction:

$$C_{\text{shell}} = \frac{C}{f_{\text{shell}}} \tag{4.1}$$

where $f_{\text{shell}} = 0.461 \pm 0.14$ ($46 \pm 14\%$) represents the viable volume fraction derived from the confocal microscopy measurements (Section 4.2.1.2).

The results are presented in the following table 4.4, compared to the results of the initial bulk concentrations measured by ICP-MS (shown in table 4.3):

Table 4.4: Comparison between the initial bulk 3D ICP-MS ^{10}B concentrations (measured across the whole spheroid volume) and the concentrations normalized to the viable proliferating shell in 3D PANC-1 tumor spheroids [mean ± SD].

Incubation Condition	**C** [μg/g]	$C_{\mathbf{shell}}$ [μg/g]
Untreated Control	0.006	0.006
2 h BPA	1.12 ± 0.03	2.4 ± 0.2
4 h BPA	1.51 ± 0.03	3.3 ± 0.2

Accounting for the non-accumulating necrotic core increases the effective ^{10}B concentration in the viable proliferating shell. These corrected values reflect the biologically relevant ^{10}B concentration and were implemented in the dose calculation in Section 4.2.3.

Qualitative Neutron Autoradiography:

Approximated co-localization of the autoradiography samples was performed with histological sections stained with hematoxylin and eosin (Fig. 4.6).

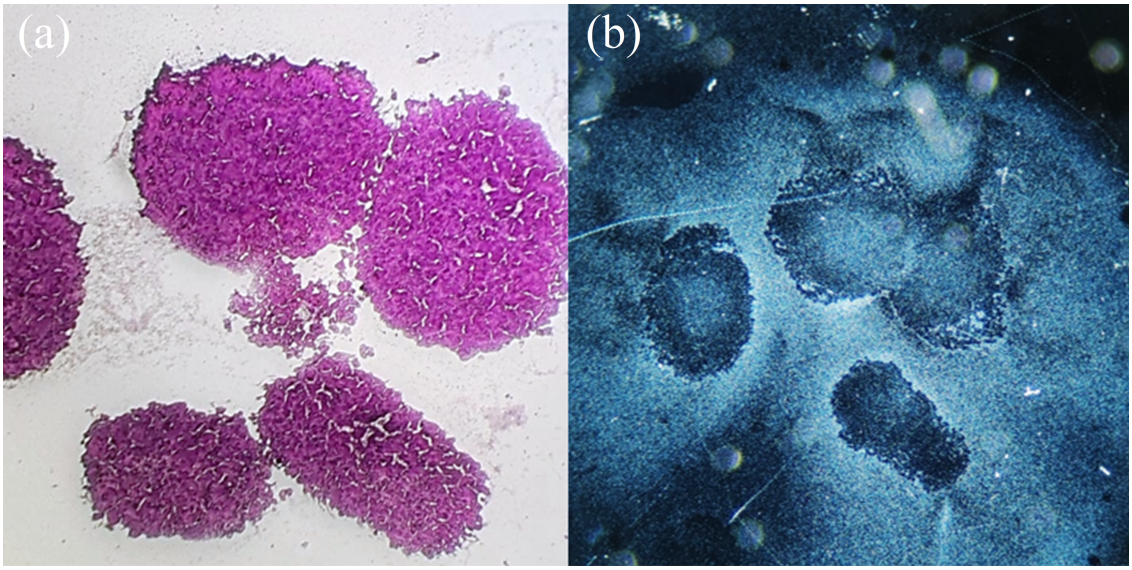


Figure 4.6: 3D PANC-1 spheroids embedded in OCT (a) Histological staining with hematoxylin and eosin (b) Autoradiography after BPA incubation using an air-dried sample.

Perfect correspondence between the histological sections and the neutron autoradiography is constrained by the physical slicing of the OCT-embedded spheroid sample. In particular, cellular histology required 20μm slice thickness, while the autoradiography 60μm. As a result, since the two sections are consecutively obtained, they are capturing different depths of the spheroids, and this depth difference justifies the observed deviations between them.

The qualitative neutron autoradiography confirmed a substantial difference in ^{10}B uptake in BPA-incubated spheroids compared to untreated controls (Fig. 4.7).

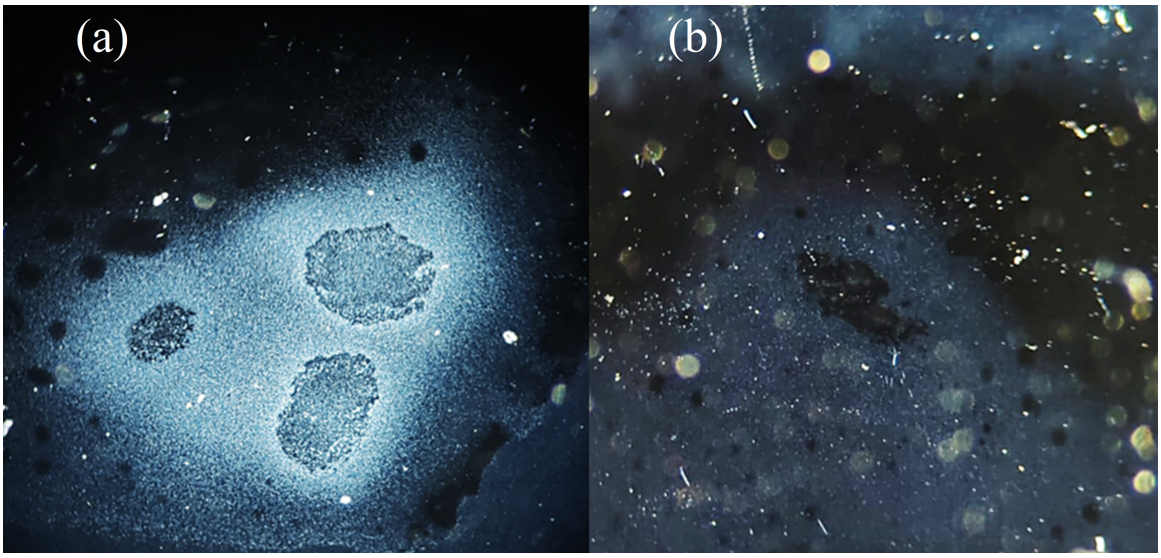


Figure 4.7: Neutron autoradiographies of an air-dried sample of 3D PANC-1 spheroids embedded in OCT (a) after 2h incubation with BPA 4mM, (b) control with no BPA.

Control samples appeared dark, exchibiting only bright background protons tracks from the $^{14}N(n,p)^{14}C$ reaction of nitrogen in the air. In contrast, BPA-treated spheroids displayed a high, bright track density due to the high-LET $^{10}B(n,\alpha)^{7}Li$ reaction products, confirming the boron delivery step.

However, the boron signal was not confined within the anatomical borders of the spheroid, extending beyond them into the surrounding OCT medium. This spatial broadening is indicative of BPA leaching from the tissue into the embedding matrix. This phenomenon aligns with the observations of a recent quantitative LA-ICP-MS imaging study on tumor spheroids incubated with BPA [88], which reported peripheral boron signal at the spheroid boundary reaching an average of 85% of the maximum intraspheroid signal in OCT embedded spheroids, with a secondary signal peak of 37% detected approximately 1000μm from the spheroid center, consistent with diffusion to neighboring spheroids. This is due to boron's solubility and limited intracellular binding, making it highly susceptible to redistribution via diffusion and leaching into the matrix during sample preparation.

As additionally demonstrated by [88], freeze-drying the samples after cryosectioning preserves signal intensity and spatial fidelity, with an increase in mean signal ($\sim$30%) and improved contrast relative to frozen, non–freeze-dried samples. Based on this, we hypothesize that BPA leaching occurred during the drying process at room temperature, during which BPA dissolved in the aqueous part of the spheroid diffused inside but also outside the spheroid into the surrounding OCT.

Further studies are currently being conducted, evaluating lyophilization as an approach of the sample's drying process, as opposed to air-drying at room temperature, in order to test if it can mitigate the BPA spreading beyond the spheroid structure. Preliminary results of this approach are shown in Fig.4.8. Images were acquired using a phase contrast optical microscope and a Leica MZ16A stereomicroscope.

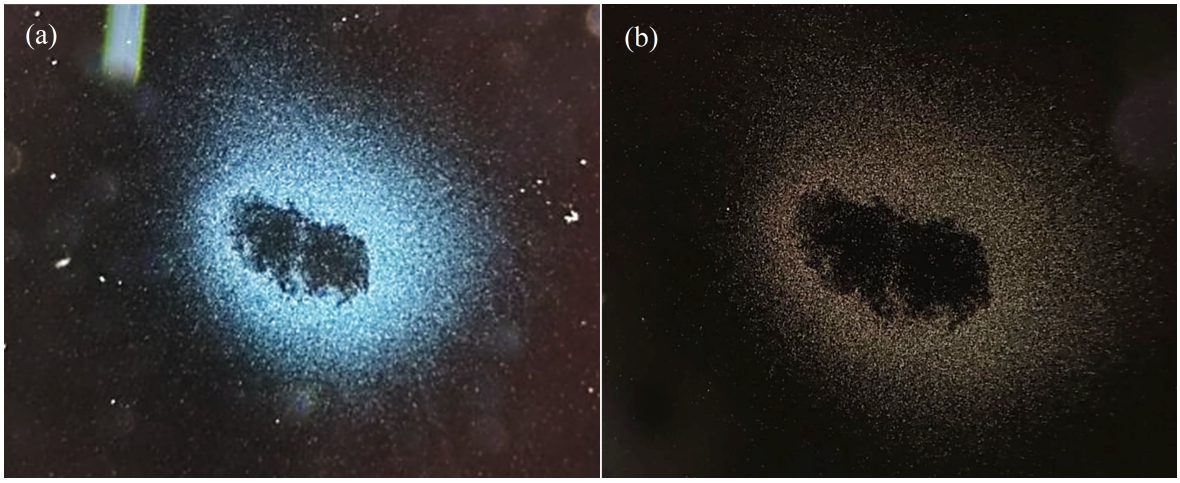


Figure 4.8: Neutron autoradiographies of a freeze-dried sample of 3D PANC-1 spheroids embedded in OCT after 2h incubation with BPA 4mM captured by (a) an optical microscope and (b) a stereomicroscope

Although minor leaching beyond the spheroid perimeter is still observed with freeze-drying, the boron signal is no longer uniformly smeared across the entire spheroid volume, in contrast to Fig. 4.7. The presence of a darker central core surrounded by a brighter peripheral halo suggests a marked improvement in preserving localized boron distribution, marking the lyophilization approach as particularly promising.

4.2.3 Radiobiological Response of PANC-1 2D Monolayers and 3D Spheroids to Neutron, BNCT, C-ion, and Combined Irradiation

4.2.3.1 2D Cultures

Following the clonogenic assay procedure explained in Section 3.2.4.4, the SF were calculated for each irradiation modality using Eq.3.13. The results are displayed in the table below:

Table 4.5: Clonogenic surviving fraction and delivered physical absorbed doses in 2D PANC-1 cell monolayers.

Radiation Modality	**Dose (D) [Gy]**	**Surviving Fraction (SF ± SD)**
C-ions	0	1.0 ± 0.3
	1	0.6 ± 0.1
	2	0.5 ± 0.2
	4	0 ± −
Neutrons	0m_n: 0 ± −	1.0 ± 0.2
	5m_2h_n: 0.5 ±0.05	0.7 ± 0.1
	5m_4h_n: 0.5 ±0.05	0.3 ± 0.2
	10m_n: 1.1 ±0.05	0.43 ± 0.04
Neutrons + BPA (BNCT)	0m_2hBPA: 0 ± −	1.0 ± 0.2
	5m_2hBPA: 1.9 ±0.2	0.02 ± −
	5m_4hBPA: 1.9 ±0.2	0 ± −
	10m_2hBPA: 2.1 ±0.2	0.019 ± 0.004
Combination (C-ions + BNCT)	2 Gy + 0m_2hBPA: 2 ± −	3.7 ± 0.4
	2 Gy + 5m_2hBPA: 3.9 ±0.2	0 ± −
	2 Gy + 5m_4hBPA: 3.9 ±0.2	0 ± −

The absorbed doses for the 2D cell monolayer neutron and BNCT irradiations were obtained from prior computational simulations at the thermal column of the TRIGA Mark II reactor [64], upon whose model the present 3D spheroid simulation geometry was developed.

Values of SF=3.7 and SF=0 in the case of the combined modality and BNCT, could be attributed to seeding errors or cell counting inaccuracies. This reflects a crucial limitation of clonogenic assays, which require a balance between underseeding, not seeding sufficient cells for colony formation, and overseeding, causing colony overlap.

4.2.3.2 3D Spheroids

Utilizing Eq.3.14, the normalized radius (R_{norm}) and the shrinkage of the spheroids were quantified for all the different irradiation conditions, with their corresponding errors. In addition, the growth curves of the spheroids are presented as the normalized radius in relation to the days post-irradiation. The mean value of that day with the corresponding standard error is shown in all graphs.

BNCT experiment 1: The spheroids were incubated for 2 hours with or without 4mM BPA and then exposed to the thermal neutron field for 5min or 10min. The results of their radius regression post-irradiation are shown below. Measurements of 12 spheroids, on average, were used for each irradiation condition.

Table 4.6: BNCT 1: Normalized radius ($R_{\text{day10}}/R_{\text{day}-1}$) and spheroid regression across different irradiation times with and without BPA.

Condition	Irradiation Time	Total Spheroid Dose (Gy)	R_{norm}	Regression (%)
n	0 min	0	0.79 ± 0.05	21 ± 5
	5 min	0.71 ± 0.08	0.96 ± 0.08	4 ± 8
	10 min	1.4 ± 0.2	1.13 ± 0.08	-13 ± 8
BPA + n	5 min	0.98 ± 0.09	0.6 ± 0.1	38 ± 10
	10 min	2 ± 0.2	0.90 ± 0.10	10 ± 10

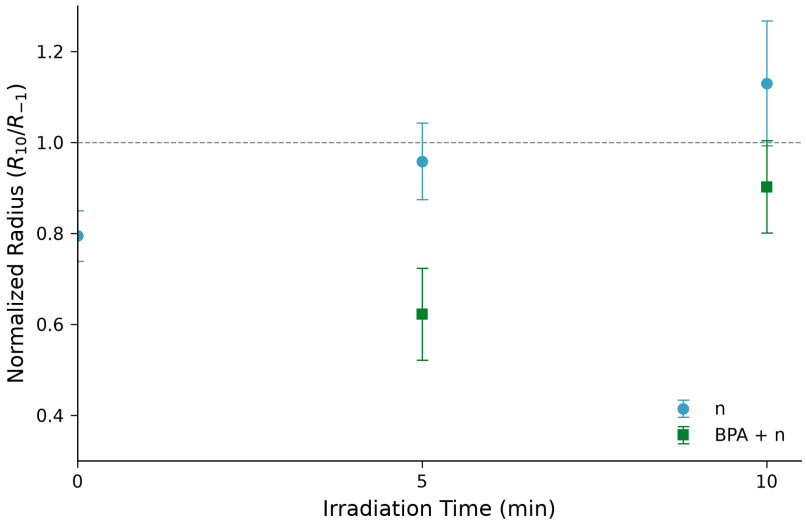


Figure 4.9: Normalized radius of spheroids irradiated with neutrons with and without BPA, with respect to the irradiation time.

From Fig.4.9 it can be shown that the level of shrinkage of the size of the spheroid after neutron irradiation at a corresponding time with BPA is higher compared to just neutron irradiation without BPA. This showcases the increased biological effectiveness of combining the two. The higher normalized radius observed at 10 minutes irradiation is likely an artifact of the limited sample statistics, combined with the radiation-induced damage to the cell, reducing the spheroid's compactness and producing peripheral debris that may have been misinterpreted during the analysis as an increase of the radius.

BNCT experiment 2: Spheroids were exposed to the thermal neutron beam for 5 minutes, after incubation of either 2 or 4 hours of BPA, for three biological replicates (a, b, c). The results of the radius regression of the spheroids are shown below. On average, measurements of 6 spheroids per biological replicate, were used for each irradiation condition.

Table 4.7: BNCT 2: Normalized radius (R_{day9}/R_{day-1}) and regression across biological replicates (a, b, c) under various incubation and exposure conditions.

Condition	Irradiation/ Incubation Times	Total Spheroid Dose (Gy)	Bio Replicate	R_{norm}	Regression (%)
n	0 min	0	a	1.00 ± 0.07	0 ± 7
			b	0.77 ± 0.03	23 ± 3
			c	0.84 ± 0.05	16 ± 5
BPA + n	0 min	0	a	0.88 ± 0.03	12 ± 3
			b	0.88 ± 0.02	12 ± 2
			c	0.94 ± 0.03	6 ± 3
n	5 min (2 h)	0.71 ± 0.08	a	0.80 ± 0.07	20 ± 7
			b	0.84 ± 0.04	16 ± 4
			c	0.97 ± 0.05	3 ± 5
BPA + n	5 min (2 h)	0.98 ± 0.09	a	0.58 ± 0.03	42 ± 3
			b	0.65 ± 0.06	35 ± 6
			c	0.65 ± 0.07	35 ± 7
n	5 min (4 h)	0.71 ± 0.08	a	0.94 ± 0.07	6 ± 7
			b	0.87 ± 0.03	13 ± 3
			c	0.89 ± 0.03	11 ± 3
BPA + n	5 min (4 h)	1.07 ± 0.09	a	0.58 ± 0.01	42 ± 1
			b	0.60 ± 0.03	40 ± 3
			c	0.66 ± 0.04	34 ± 4

Graphs showing the evolution of normalized radius over time post-irradiation, for neutron irradiation with or without BPA, across the different irradiation conditions, are shown below.

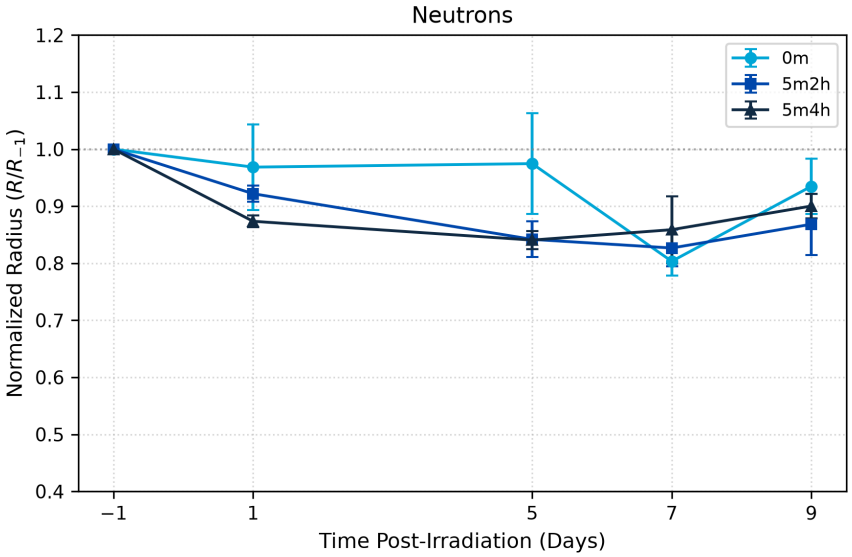


Figure 4.10: Normalized Radius of spheroids irradiated with neutrons, with respect to the days post-irradiation. [mean ± SEM]

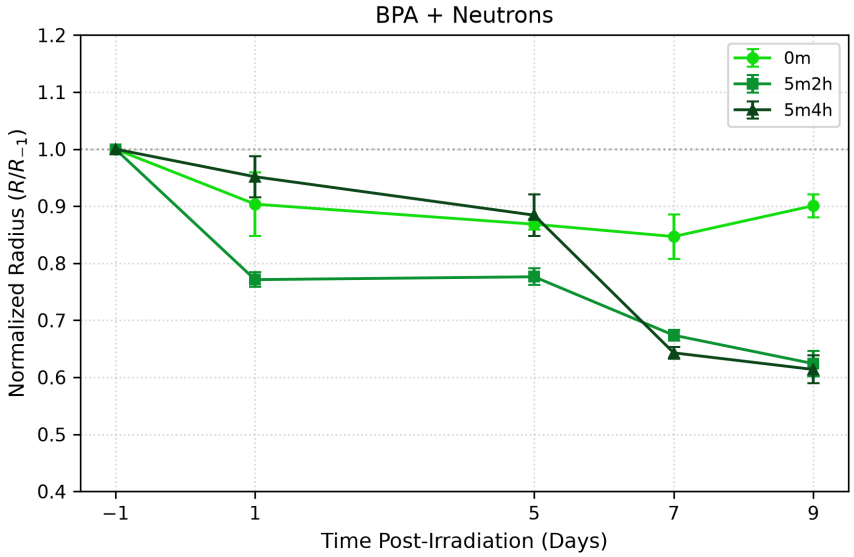


Figure 4.11: Normalized Radius of spheroids irradiated with neutrons after incubation with BPA, with respect to the days post-irradiation. [mean ± SEM]

In the neutron irradiation radius evolution curve (Fig.4.10), we observe a minimum of the normalized radius between days 5-7, followed by a recovery or stabilization by day 9. On the contrary, in case of BPA incubation prior to the neutron irradiation (Fig.4.11), the size regression of the spheroids is not fully stabilized by day 9 post-irradiation.

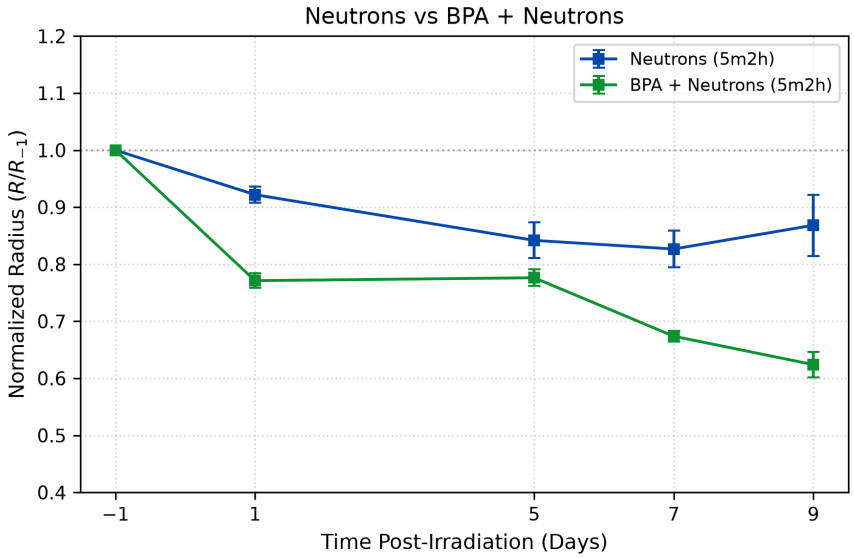


Figure 4.12: Comparison of the normalized radius of spheroids irradiated with 5 min neutron irradiation with and without a 2h incubation with BPA, as a function of the days post-irradiation.

A direct comparison of the 5min neutron irradiation modalities are shown in Fig.4.12, with and without a 2h BPA incubation. This results showcase the increased effect in the spheroid viability of neutron irradiation when combined with BPA, verifying the higher therapeutic efficacy of BNCT, compared to just neutrons.

C-ions: For the C-ions analysis, measurements of 11 spheroids on average were used per biological replicate per irradiation condition (0, 1, 2, 4 Gy).

Table 4.8: C-ions: Dose-response and spheroid regression ($R_{\text{day10}}/R_{\text{day}-1}$) across biological replicates exposed to carbon ion beams.

Dose (Gy)	Bio Replicate	R_{norm}	Regression (%)
0	a	0.9 ± 0.1	12 ± 12
	b	0.9 ± 0.1	12 ± 11
	c	1.20 ± 0.04	-20 ± 4
1	a	0.95 ± 0.10	5 ± 10
	b	0.76 ± 0.05	24 ± 5
	c	1.21 ± 0.05	-21 ± 5
2	a	0.63 ± 0.02	37 ± 2
	b	1.00 ± 0.04	0 ± 4
	c	1.00 ± 0.02	0 ± 2
4	a	0.66 ± 0.03	34 ± 3
	b	0.85 ± 0.02	15 ± 2
	c	0.78 ± 0.04	22 ± 4

In the following graph, the mean value of the different biological replicates is depicted.

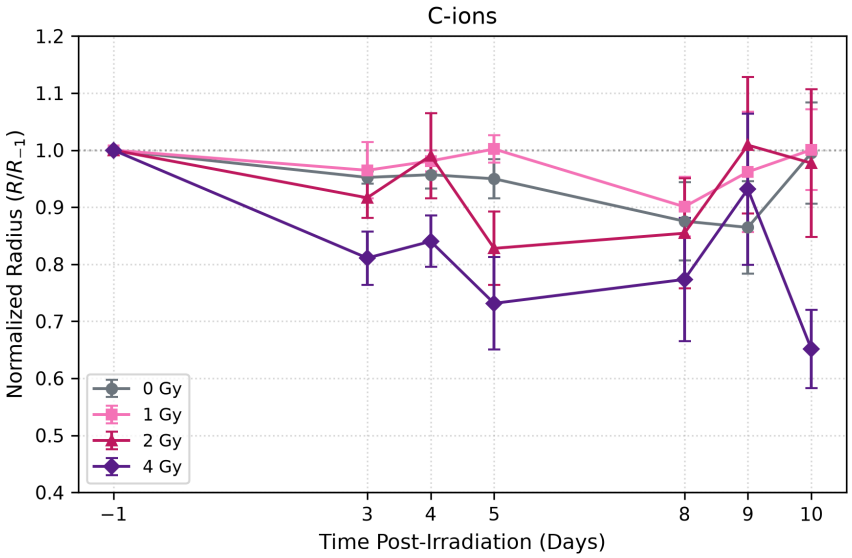


Figure 4.13: Normalized Radius of spheroids irradiated with different doses of C-ions, with respect to the days post-irradiation. [mean ± SEM]

As shown in the graph, only the 4Gy dose of CIRT induced a significant effect on the spheroids at day 10, whereas lower doses are exhibiting slighter size variations during the 10 days after irradiation, concluding approximately at a normalized radius value of 1 at day 10. Notably, the final endpoint is comparable to that achieved with BNCT, despite BNCT delivering a substantially lower physical doses to the spheroids (0.65 and 0.75 Gy for 2h and 4h BPA incubation accordingly), compared to the 4Gy CIRT exposure.

C-ions and BNCT combination: For the combination treatment modality, data from 3 spheroids on average were used for each protocol.

Table 4.9: C-ions and BNCT Combination: Combined effect of carbon ion irradiation (2 Gy) and neutron exposure with or without BPA on spheroid regression.

Condition	Combined Protocol	Total Spheroid Dose (Gy)	R_{norm}	Regression (%)
n	2 Gy + 0 min	2	0.6 ± 0.1	45 ± 11
	2 Gy + 5 min (2 h)	2.71 ± 0.08	0.7 ± 0.1	31 ± 14
	2 Gy + 5 min (4 h)	2.71 ± 0.08	1.07 ± 0.08	-7 ± 8
BPA + n	2 Gy + 0 min	2	0.6 ± 0.1	37 ± 12
	2 Gy + 5 min (2 h)	2.98 ± 0.09	0.7 ± 0.1	34 ± 14
	2 Gy + 5 min (4 h)	3.07 ± 0.09	0.68 ± 0.05	32 ± 5

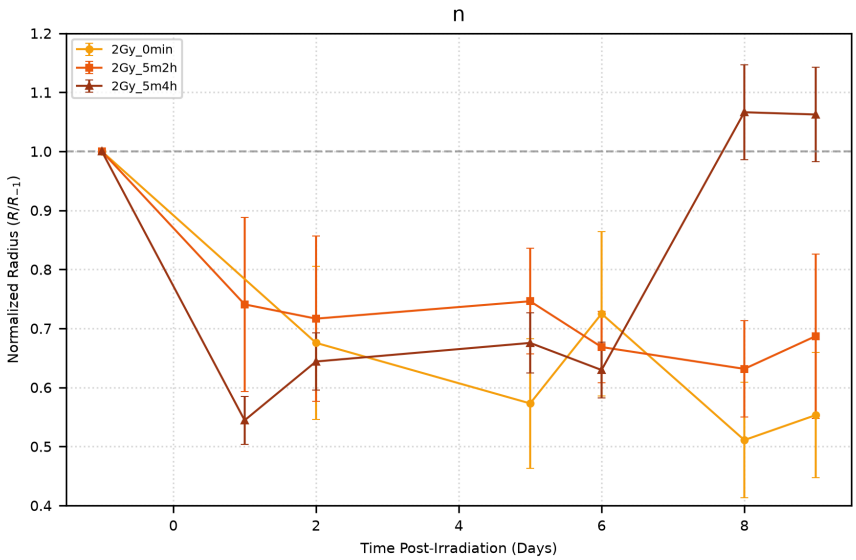


Figure 4.14: Normalized Radius of spheroids irradiated with a combination of C-ions (2Gy) and neutrons, with respect to the days post-irradiation. [mean ± SEM]

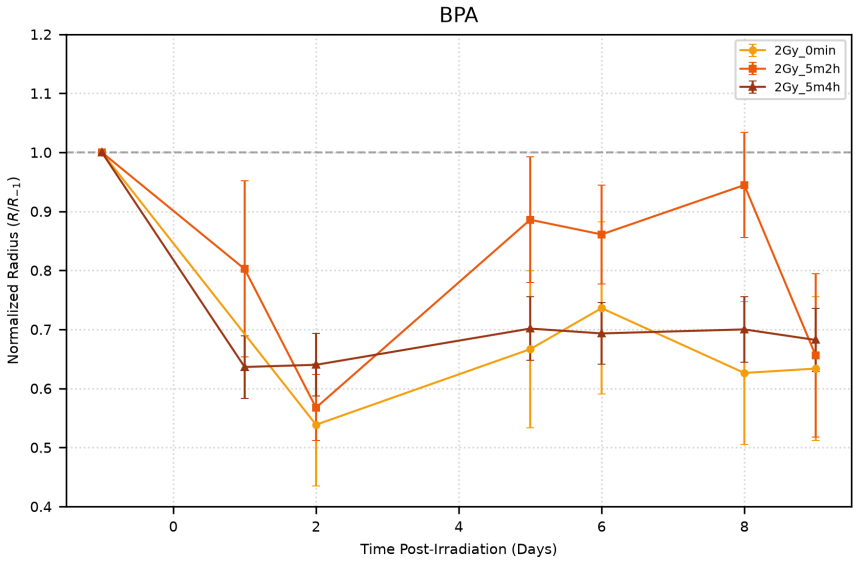


Figure 4.15: Normalized Radius of spheroids irradiated with a combination of C-ions (2Gy) and neutrons after incubation with BPA, with respect to the days post-irradiation. [mean ± SEM]

The combined CIRT-BNCT experiments are showing spheroid regression of a magnitude comparable to the single modalities, but with high variability between spheroids and a small sample size, so no conclusive additive or synergistic effect could be established at the current level.

It is important to note that during the post-irradiation, data acquisition period, the catastrophic irradiation effects on the spheroids were shown by the shedding of necrotic outer cells. This created a halo of cellular debris surrounding the spheroids (as shown in Fig.4.16), posing a challenge during the image analysis, by complicating the precise detection of the boundaries of the spheroid by the implemented macro of ImageJ.

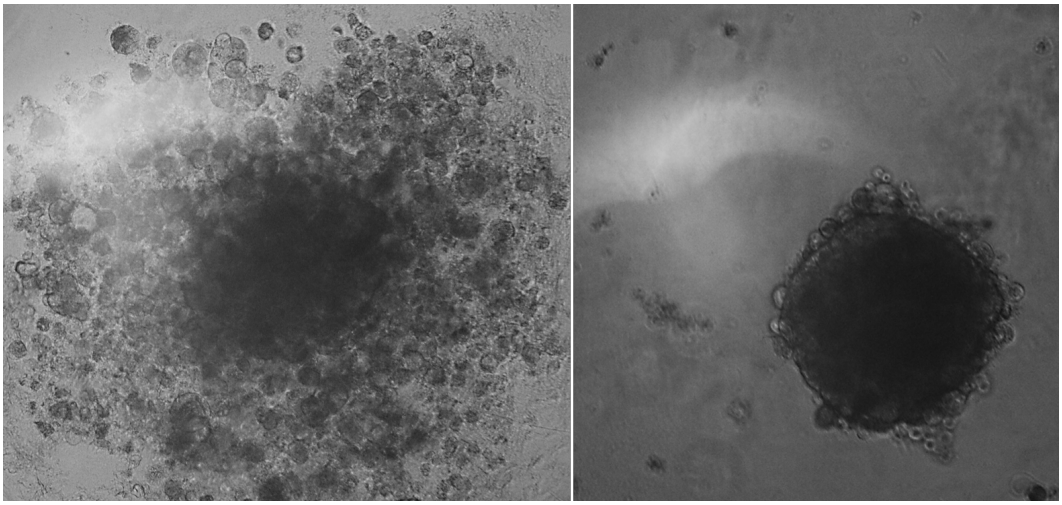


Figure 4.16: Picture taken at x10 magnification of the same spheroid, day 10 post-irradiation (2h BPA incubation and 10min thermal neutron beam exposure) , before (left) and after (right) the change of medium.

The observed increase of the apparent spheroid radius towards the last days of the data acquisition was possibly due to that. On the last day of data collection, complete medium replacement was performed across all conditions, to eliminate the debris. The reduction in the radius value observed on the last day reflects the accurate, debris-free measurement of the intact spheroid core, based on which the total radius regression was calculated.

Boron Enhancement:
The percentage of boron enhancement between the same conditions with and without BPA, was calculated using Eq.3.15, with the corresponding errors, across all experimental modalities.

Table 4.10: Percentage of boron enhancement across experimental setups.

Experiment	Condition	Total Spheroid Dose (Gy)	Biological Replicate	Boron Enhancement (%)
BNCT exp 1	5 min (2h)	0.98 ± 0.09	—	35 ± 12
	10 min	2.0 ± 0.2	—	20 ± 10
BNCT exp 2	5 min (2 h)	0.98 ± 0.09	a	27 ± 7
			b	23 ± 8
			c	34 ± 8
	5 min (4 h)	1.07 ± 0.09	a	38 ± 5
			b	31 ± 4
			c	26 ± 5
Combination	2 Gy + 5 min (2 h)	2.98 ± 0.09	—	5 ± 28
	2 Gy + 5 min (4 h)	3.07 ± 0.09	—	36 ± 7

This comparison of the normalized radius with and without BPA showcases the enhancement in effect that boron adds compared to neutron irradiation alone. Across all experiments and biological replicates, the enhancement percentage is positive. However, for the combination treatment at 2 h incubation, the value exhibits a large uncertainty possibly due to the variability between the limited statistics of this condition. While consistent with an overall positive trend, this specific result is poorly predictive.

4.2.4 Comparative analysis

Based on the results from table 4.5, the surviving fraction (SF) as a function of the dose curves were plotted for the neutron, BNCT and C-ions irradiation modalities, as shown below in Fig.4.17. The data were fitted to the Liner-Quadratic (LQ) model according to Eq.3.5. The fit is shown in the following graphs.

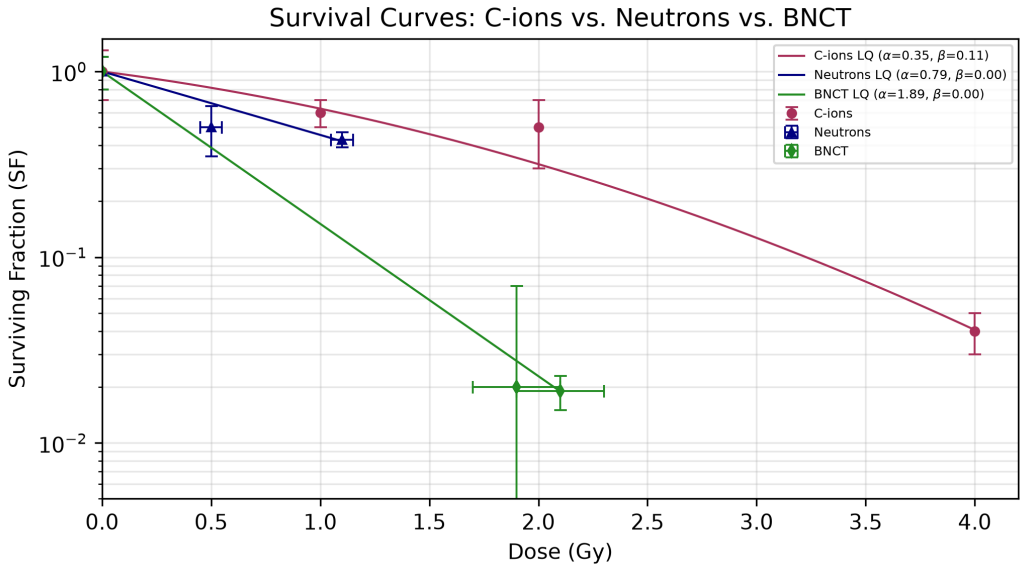


Figure 4.17: LQ fit of the survival curve of the clonogenic survival assays for 2D PANC-1 cell cultures after exposure to C-ions (pink), neutrons (blue) and BNCT (green).

For the the CIRT-BNCT combination irradiation modality, plotting and fitting the LQ of the survival curves was not possible, as the SF values were zero (Table 4.5), indicating clonogenic death.

Due to the limited number of dose points, the linear responses fitted for the BNCT and the neutron modalities, do not represent a reliable result. However, they are presented alognside the C-ions for comparison purposes.

The LQ fit parameters across all modalities are shown in the following table:

Table 4.11: Linear-quadratic model parameters (α, β) and calculated α/β ratios with standard propagated uncertainties.

Radiation Quality	α (Gy^{-1})	β (Gy^{-2})	α/β (Gy)
C-ions	0.3 ± 0.2	0.11 ± 0.05	3 ± 2
Neutrons	0.7 ± 0.8	0.0 ± 0.8	—*
BNCT	1.9 ± 10.0	0.0 ± 4.8	—*

*For Neutrons and BNCT, $\beta = 0$, representing purely linear cell survival curves where $\alpha/\beta \to \infty$ (undefined).

In addition, the survival curve for the C-ion modality was plotted and fitted to the LQ, in comparison with prior reference experimental results, obtained from previous irradiation experiments of PANC-1 cells in Pavia [52]. The fits of both are shown in the graph below:

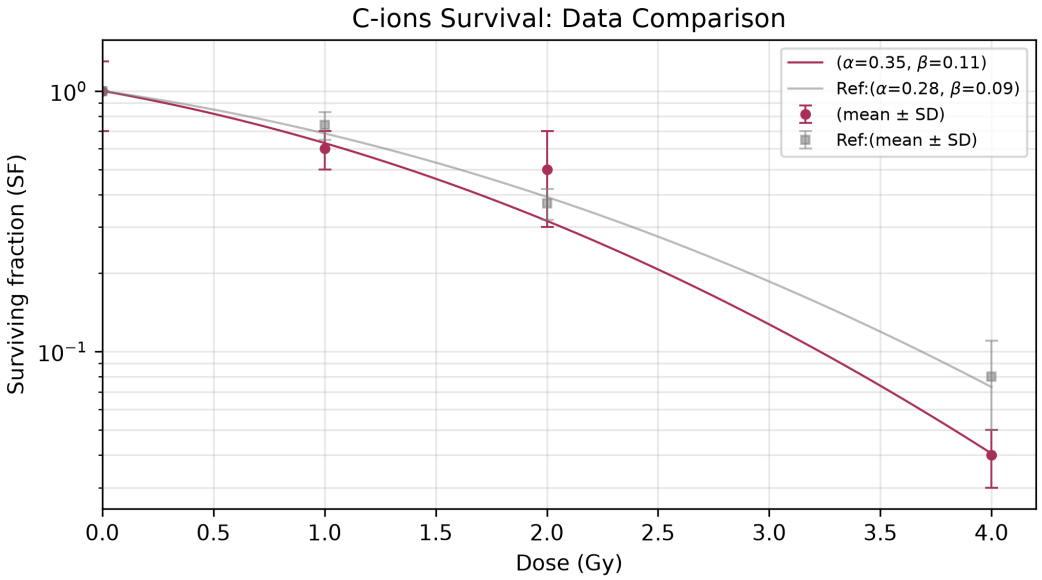


Figure 4.18: LQ fit of the survival curve of the clonogenic survival assays for 2D PANC-1 cell cultures after exposure to C-ions (blue) and comparison with the reference results [52] (grey).

The fitted survival curves demonstrate good agreement between the present and reference datasets. The fitted parameters ($\alpha = 0.3 \pm 0.2\ Gy^{-1}$, $\beta = 0.11 \pm 0.05\ Gy^{-2}$) and the ratio ($\frac{\alpha}{\beta} = 3.07 \pm 2.31\ Gy$) remain within the uncertainty intervals of the reference values ($\alpha = 0.3 \pm 0.1\ Gy^{-1}$, $\beta = 0.09 \pm 0.05\ Gy^{-2}$, $\frac{\alpha}{\beta} = 3.05 \pm 2.15\ Gy$), indicating reproducibility.

The lethal dose required to reduce the surviving fraction (SF) to 50% (LD50) was estimated at (1.5±0.5)Gy for the C-ion irradiations performed in this work, compared with (1.6±0.3)Gy for the reference dataset. For comparison, a previous study investigating C-ion irradiation of PANC-1 cells reported an LD50 of 2.1Gy [9].

Table 4.12: Comparison of absorbed doses between PANC-1 2D monolayer cultures and 3D spheroids (shell vs core) across irradiation modalities. (value ± SD)

Irradiation Modality	**2D D (Gy)**	**3D D_{shell} (Gy)***	**3D D_{core} (Gy)***
0min n	0 ± 0	0 ± 0	0 ± 0
5min n	0.5 ± 0.05	0.4 ± 0.1	0.32 ± 0.02
10min n	1.1 ± 0.05	0.8 ± 0.2	0.65 ± 0.04
0min n + 2hBPA	0 ± 0	0 ± 0	0 ± 0
5min n + 2hBPA	2.1 ± 0.2	0.65 ± 0.08	0.33 ± 0.02
5min n + 4hBPA	2.1 ± 0.2	0.75 ± 0.08	0.33 ± 0.02
10min n + 2hBPA	4.2 ± 0.2	1.3 ± 0.2	0.65 ± 0.04
2Gy C-ions + 0min n	2 ± 0	2 ± 0	2 ± 0
2Gy C-ions + 5min n	2.5 ± 0.05	2.4 ± 0.1	2.32 ± 0.02
2Gy C-ions + 0min n + 2hBPA	2 ± 0	2 ± 0	2 ± 0
2Gy C-ions + 5min n + 2hBPA	4.1 ± 0.2	2.65 ± 0.08	2.33 ± 0.02
2Gy C-ions + 5min n + 4hBPA	4.1 ± 0.2	2.75 ± 0.08	2.33 ± 0.02
0Gy C-ions	0	0	0
1Gy C-ions	1	1	1
2Gy C-ions	2	2	2
4Gy C-ions	4	4	4

*Average of the simulated doses delivered to spheroids of the center and of the outer edge well of the plate.

As observed in the table 4.12, the 3D spheroid shell doses are identical within the error margins with the 2D doses, for the neutron irradiation. On the other hand, for the irradiation modalities including BPA, the doses delivered to the 3D spheroids, assuming the boron distribution is limited to the proliferating shell, are significantly lower than the 2D cultures. These results highlight the reasons why 3D tumor models are essential for BNCT dosimetry research, as they expose the realistic limitations of BPA uptake in solid, pancreatic tumors, demonstrating why 2D monolayers routinely overestimate BNCT efficacy.

To facilitate direct comparison across modalities and to illustrate the data distributions, box plots are utilized. A boxplot provides a visual summary of how the data are distributed. The central box, containing the middle 50% of the data, represents the interquartile range (IQR), bounded by the first (Q_1, 25th percentile) and third (Q_3, 75th percentile) quartiles. The line inside indicates the median (50th percentile). The vertical whiskers show the data spread beyond the box within $1.5x$IQR, while any individual points beyond the whiskers may indicate outliers. A longer box suggests greater variability within the dataset.

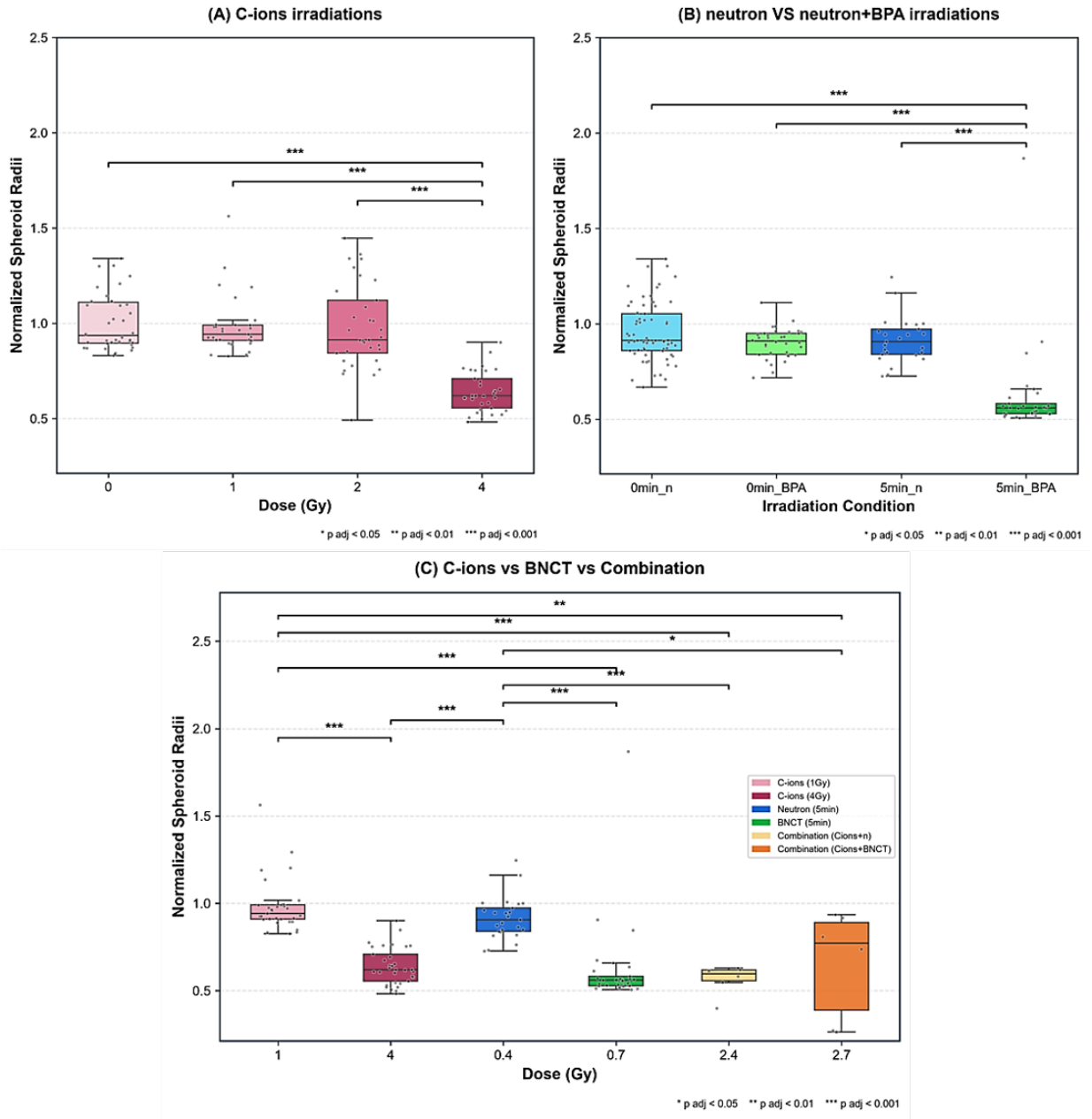


*Figure 4.19: Normalized 3D spheroid radii with respect to the irradiation conditions boxplots (A) C-ions (B) neutrons/BPA+neutrons (C) Comparison among irradiation modalities. Asterisks indicate statistically significant differences: *$p < 0.05$, ** $p < 0.01$, and *** $p < 0.001$.*

Spheroid response to C-ion irradiation exhibited a dose-dependent reduction in size. Although exposures of 1 and 2 Gy maintained median radii close to control levels, 4 Gy induced significant spheroid shrinkage, reducing the median normalized radius to approximately 0.6.

The evaluation of the thermal neutron irradiation confirmed that significant morphological damage is dependent on BPA pre-incubation. Neither the neutron beam exposure without prior BPA incubation nor the BPA incubation without neutron irradiation induced a significantly difference in spheroid shrinkage with the control modalities. Conversely, the combination of BPA incubation and 5 minutes of neutron irradiation caused a major difference in size, below 0.6. This contrast highlights that the impact of both the neutron

beam and BPA alone is negligible compared to the combination of the two, effectively validating that the high biological efficacy of BNCT stems from the localized $^{10}B(n,\alpha)^{7}Li$ capture reaction.

Fig.4.19(C) exhibits a cross-comparison among C-ions, neutron (n), BNCT, and combined C-ions with n/ BNCT modalities. The combination of 2Gy C-ions and n irradiation (2Gy + 5m_n) surpassed the effects of either the C-ions or the 5 minutes n alone, as expected. In parallel, combining 2Gy C-ions with BNCT (2Gy + 5m_BPA), corresponding to 2.7Gy, resulted in high dispersion of results with an elongated interquartile range (IQR). Notably, the BNCT modality (5min_BPA), corresponding to 0.7Gy, has achieved comparable results in spheroid regression as 4Gy C-ions and the 2Gy C-ions and 5 minutes neutron irradiation combination modality (2.4Gy). In previous studies on 2D PANC-1 cells conducted in Pavia [52], the combined modality of CIRT-BNCT demonstrated superior efficacy relative to CIRT alone, which is something that is verified also by these results, as for a dose of ∼3Gy the combination modality induced about 10% more regression than the single CIRT modality for 4Gy. However, considering the high efficacy of BNCT alone for the spheroids, a more pronounced additive effect was anticipated in the CIRT-BNCT combined modality. This is likely attributable to the limited sample size, as well as logistical constraints of the availability between the two irradiation facilities, which resulted in a time window of about 50 hours from the CIRT to the BNCT dose deliveries.

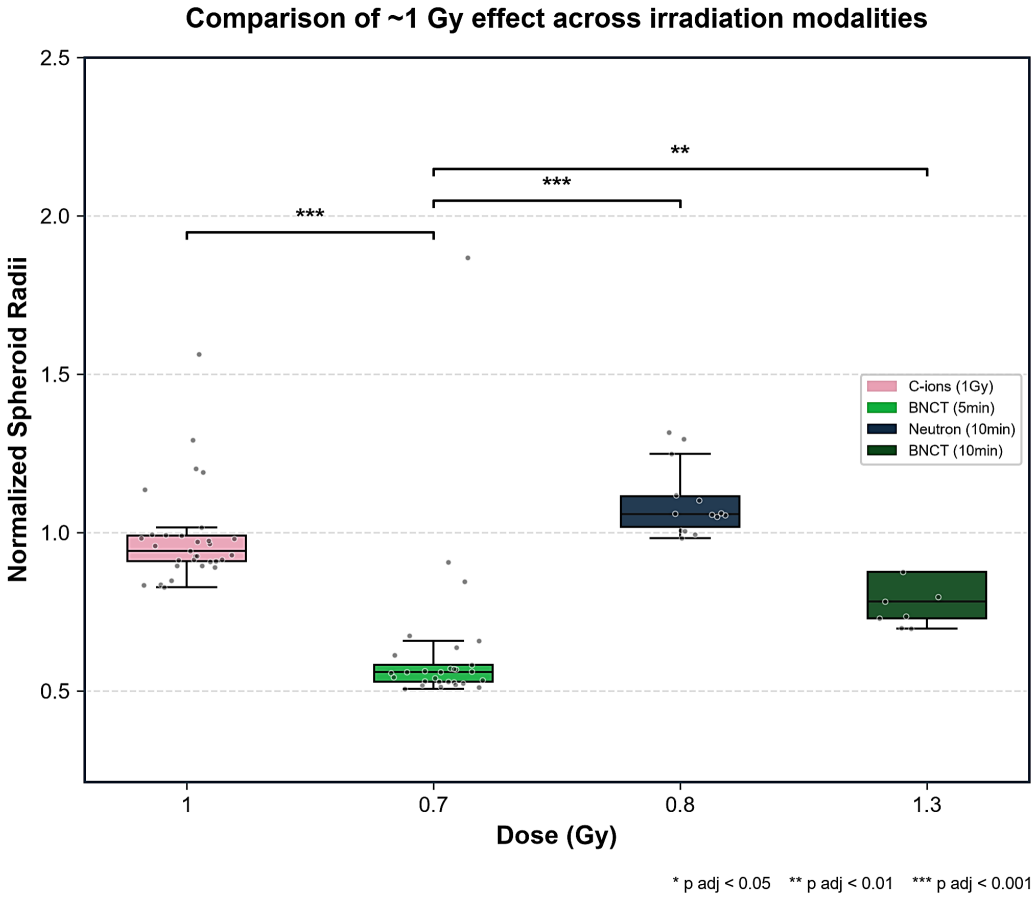


*Figure 4.20: Comparison of the effect on the 3D spheroids radii after irradiation with ∼1Gy across different irradiation modalitites. Asterisks indicate statistically significant differences: *$p < 0.05$, ** $p < 0.01$, and *** $p < 0.001$.*

At comparable absorbed doses in the range (∼0.65–1.3 Gy), comparing the different modalities revealed a more catastrophic effect for BNCT than for C-ions or neutrons alone. While 1Gy of C-ions caused minimal radius shrinkage, and the (0.8±0.2)Gy of 10 minutes n irradiations allowed continued spheroid growth, the BNCT treatment dramatically decreased the spheroids size. This could be interpreted as a preliminary experimental confirmation of the increased RBE level of BNCT compared to monoenergetic C-ions.

The reason behind the dimished effect of the 10 minutes irradiation BNCT compared to the 5 minutes, could be due to the reduced statistics of the 10 minute modality, as it was tested among just one biological replicate during the first preliminary experiment (BNCT1), whereas the 5 minutes BNCT was tested across 3 different biological replicates and also the preliminary experiment.

Indicative spheroid photos exposed to the irradiation conditions illustrated in Fig.4.20, of the same biological replicate when applicable, are shown in Fig.4.21, to visualize the effects.

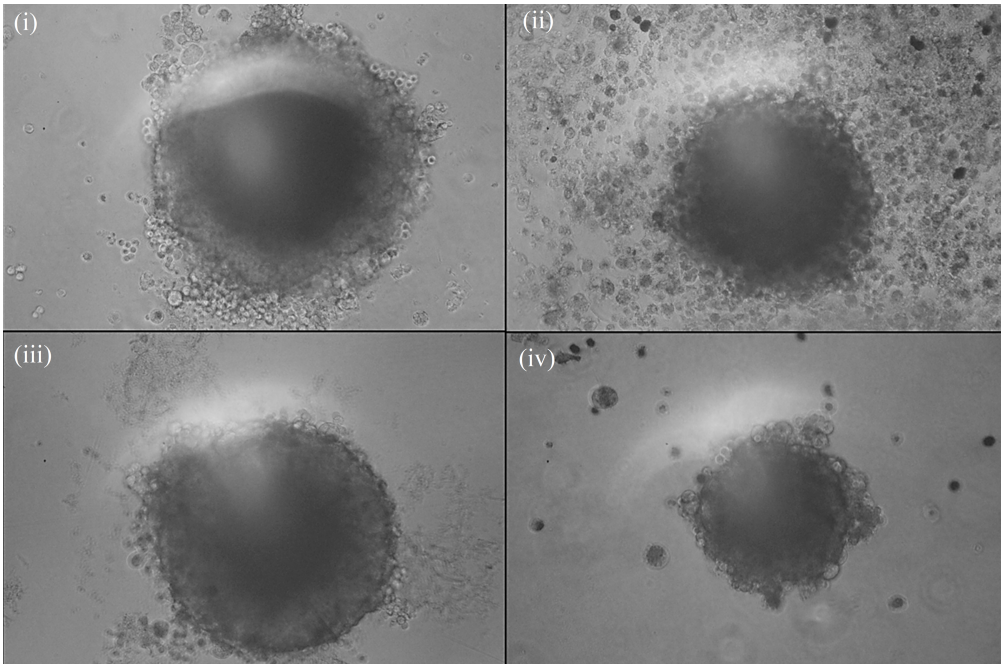


Figure 4.21: PANC-1 spheroid photos comparison captured at x10 magnification: (i) 1Gy C-ion irradiation, on day 10 post-irradiation (ii) 5 minutes n irradiation with 2h BPA incubation, on day 9 post-irradiation (iii) 10 minutes n irradiation without BPA incubation on day 10 post-irradiation (iv) 10 minutes n irradiation with 2h BPA incubation on day 10 post-irradiation.

The observation of the differences of such disruptions on the spheroids by the different irradiation modalities led to qualitative results of the spatial impact of each radiation type.

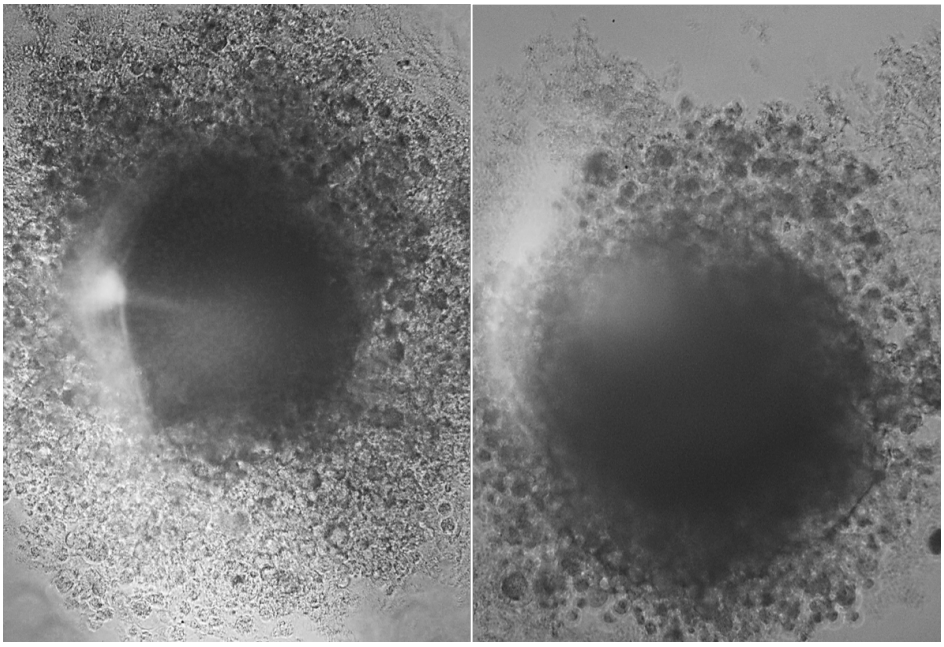


Figure 4.22: PANC-1 spheroids captured at x10 magnification exposed to ∼1Gy BNCT (left) and 4Gy C-ion irradiation (right), on day 8 post-irradiation, from the same biological replicate.

The morphological response revealed distinct spatial damage patterns between BNCT and CIRT. Specifically in Fig.(4.22), an example is shown comparing spheroids exposed to ∼1Gy BNCT compared to 4Gy C-ion irradiation. This type of destruction was detected for the combination modalities, the BNCT and the 4Gy C-ions, whereas for the lower-Gy C-ion doses and for the neutron irradiations the spheroids did not exhibit such a distinct effect (Fig.4.21).

BNCT induced a more pronounced effect on the outer part of the spheroid, expressed as a substantial amount of debris in the periphery and a more distinct size reduction. This reflects the BPA uptake by the proliferating cells that are located in the spheroid's shell. On the other hand, C-ions effectively target the radioresistant, hypoxic core, resulting in comparatively less peripheral debris even at a higher dose. These qualitative observations support the rationale for combining both modalities, highlighting their complementary biological targeting profiles.

Additionally, since the active accumulation of BPA in the spheroids is assumed to be restricted to the proliferating shell, the boron dose is therefore deposited within in. The amount of spheroid size regression exhibited suggests that the high-LET damage of the shell affects also any viable cells in the deeper core and the quiescent cell population. This can be attributed to two mechanisms: microdosimetric cross-firing effect and radiation induced bystander effect (RIBE). Firstly, for the capture reactions occurring at the inner periphery of the shell, due to the ranges of the high-LET products (∼5-9μm), part of their Bragg peak escapes the origin cell and produces a cross-fire effect, depositing physical doses directly into the neighboring border cells of the core [89]. Secondly, RIBE amplifies this damage beyond the range of the ions, proposing that signals generated from irradiated cells induce a similar effect in nearby, non-irradiated cells, due to the existence of physical contact between them, which generates intercellular communication and by the release of signaling molecules by the irradiated cells [90].

Chapter 5

Conclusions

5.1 Summary of key findings

This thesis focuses on building an integrated experimental and computational framework for evaluating BNCT and CIRT, separately and combined, using 3D PANC-1 spheroids as an in-vitro model of pancreatic cancer, in comparison with 2D monolayers. PDAC resistance to conventional radiotherapy, driven by its dense TME, high hypoxia levels and close proximity to surrounding OAR, leaves surgery as the only potentially curative treatment. In this context, advanced particle therapies offer a promising alternative. CIRT effectively delivers homogeneous doses to deep, hypoxic tissues, while BNCT selectively targets metabolically active cells, via tumor-specific ^{10}B uptake. A combined approach of the two could exploit these features to synergistically target both the infiltrative margins and the hypoxic cores of radioresistant solid tumors such as the PDAC, sparing the surrounding healthy tissues. To evaluate these modalities, more realistic preclinical models, compared to the 2D monolayers, are required, such as 3D spheroids, that can more accurately resemble the tumor architecture, which directly affects drug penetration and hypoxia profiles, thus treatment efficacy.

The key findings are summarized below, according to the thesis' objectives stated in Chapter 1.

The 3D spheroids were first characterized, by assessing their shape and size. Over a 5-day period post-seeding, they grew into increasingly compact and round structures. The spatial distribution of the viability of the spheroid cells was mapped via confocal fluorescent microscopy, showing a viable proliferating shell, accounting for ∼46% of the spheroid volume, surrounding a necrotic core. This highlights the relevance of the 3D spheroid model over the 2D, as it resembles the architecture of solid tumors, justifying spheroids as a more representative model for BNCT dosimetry.

This structure was then used to build the geometry model for the MCNP6 simulation, which addresses the problem of computational dosimetry considering the 96-well plate irradiated in the modified thermal column of the Triga Mark II reactor of Pavia University. The simulation provided the dose components of the proliferating shell and the necrotic core separately, mainly driven by the assumption that ^{10}B internalization was limited to the viable external layer, showing a dose-rate difference between them and between central and edge wells. In particular, for the outer shell of the spheroids, the doses

showed a ∼ 33% increase in the edge well compared to the central one in the case of neutron irradiation and ∼ 15% increased for BNCT. For the spheroid core, there was on average a reduction of ∼ 2.5% from the dose of the central well to the outer well, among neutron and BNCT modalities. This indicates that not only the geometry model, but also the precise irradiation position affects the received dose. This is likely because of the parabolic profile exhibited of the thermal neutron flux in tissue equivalent material, due to the less attenuated neutron-flux on the plate edges. Ultimately, this variability holds great importance in terms of real tumor settings, where heterogeneous fluence and cellular uptake prevent a uniform dose delivery, highlighting the necessity for microdosimetric modeling for BNCT.

The ^{10}B vector used in this thesis is BPA, one of the two clinically approved agents for BNCT. BPA incubation did not produce any detectable cytotoxicity in the spheroids. Preliminary qualitative neutron autoradiography, using OCT-embedded spheroids, demonstrated a significantly higher track density in BPA-incubated spheroids compared to the controls, although the boron signal was not confined within the spheroid borders, indicating leaching into the OCT matrix during sample preparation. Regarding the ICP-MS analysis, the principal approach used to derive quantitative information on ^{10}B accumulation by spheroids, the boron uptake strongly differed between the two models, with the 3D spheroids reaching 1.1-1.5 ppm (for 2h and 4h of incubation respectively), about an order of magnitude below the 15-16.7 ppm measured in the 2D model. Upon normalizing the concentration to the spheroid's viable shell, where the BPA accumulation is assumed to be confined, the boron concentration, 2.4-3.3 ppm, remained substantially lower than the 2D values. These results are in line with what is expected under the biological point of view, that the more compact and internally structured 3D models offer naturally less surface and thus receptors for the active uptake of BPA. Thus, these preliminary results seems to confirm that 2D cultures overestimate boron uptake and delivery, and therefore BNCT efficacy.

Consequently, the calculated doses for the neutron irradiation conditions including BPA pre-incubation were significantly lower in the 3D model than in the 2D, while the neutron doses without BPA were identical within uncertainty concerning the 2D model and the 3D spheroids shell. In 2D monolayers, BNCT reduced the clonogenic surviving fraction by 2% or lower. In 3D spheroids, neutron irradiation or BPA incubation separately did not produce any changes to the spheroid size, whereas BPA incubation followed by 5 minutes of neutron exposure led to a size regression of ∼38%, at physical doses ∼1Gy. The boron enhancement was positive for every tested condition, at ∼30% for BNCT delivering doses of ∼1 Gy. Regarding C-ions, only 4 Gy irradiation produced a significant shrinkage of ∼24%, with the doses of 1 or 2 Gy having minimal effects at the endpoint. Therefore, BNCT was the most effective modality tested for the spheroids, achieving comparable results to the C-ions despite delivering a much lower physical dose, consistent with the high-LET products of the ^{10}B(n, α)^{7}Li reaction. Because the 2D and 3D endpoints differ (clonogenic survival versus spheroid size), the two models are compared qualitatively.

Regarding the CIRT-BNCT combined modality, in the 2D model, an estimated dose of (3.9 ± 0.2)Gy led to complete loss of clonogenic capacity, so no survival curve could be fitted. In the 3D model, a total estimated dose of ∼ 3Gy produced a size regression of ∼34%, comparable to that of single modalities. However, due to the variability between spheroids, the extended interval between the two fractions due to logistical difficulties between the two irradiation facilities, and the reduced sample statistics, no additive or

synergistic effect could be established by the present study alone. Nevertheless, qualitative morphological assessments of each modality separately, demonstrated distinct spatial damage patterns, highlighting their complementary biological targeting profiles and supporting the rationale for their combination.

To our knowledge, these represent the first experimental data evaluating the CIRT-BNCT combination in 3D PANC-1 spheroids. This work allowed to set a starting point conditions scenario for the effective implementation of more realistic and relevant biological models for the application of BNCT in pancreatic tumours.

5.2 Preliminary nature of the study and future directions

This thesis is a preliminary study within a broader project about the combination of CIRT and BNCT in pancreatic cancer. It aims to evaluate the use of 3D PANC-1 spheroids as a model by providing the first preliminary data, and not a definitive quantification of the treatment efficacy.

For future studies, as a first step, an increase of the number of spheroids and biological replicates is needed for each irradiation modality, to confirm and strengthen the statistical validity of the described outcomes. Additional combination modalities should be explored, varying the doses, irradiation order and timing, for a more systematic analysis. Furthermore, the treatment's response for the spheroids was evaluated only through morphological analysis, so it should evolve to include also viability and proliferation assays.

Regarding the boron uptake studies, since the boron concentration was measured in bulk by ICP-MS, while the shell concentration depends on the assumption of confinement to the viable shell, apart from the repetition of the ICP-MS analysis, the microdistribution should be assessed more reliably. A preliminary attempt of improving the sample preparation protocol for neutron autoradiography by freeze-drying the samples, showed dark areas without tracks inside the spheroids, suggesting limited BPA diffusion in the deeper spheroid regions. Even though the results are promising, more replicates are required for the optimization of the sample preparation protocol. Another possible advancement could be the use of a fluorescent nuclear track detector (FNTD), to improve the acquisition of the spatial distribution of ^{10}B as a function of the different layers composing the spheroids.

Moreover, the 3D single cell line spheroid, should be evolved into a more realistic model, by combining also additional cell lines (like fibroblasts or endothelial cells) with the PANC-1 cells, and ultimately to patient-derived organoids. On the computational side, the MNCP6 model should be complimented by including Geant4-DNA, a code capable of simulating DNA damage at the level of the specific cell line exploited in the experiments.

These developments will be especially relevant with the upcoming accelerator-based neutron source at CNAO, which will allow both modalities to be studied at one site.

In conclusion, 3D spheroids proved to be a more realistic model for BNCT dosimetry than 2D monolayers. They show that BPA delivery in solid tumor-resembling architecture is limited, yet BNCT still produced a clear response at low physical dose. The CIRT-BNCT combination in 3D models remains an open question that this thesis does not close, but marks its starting point.

References

[1] World Health Organization. *Global status report on cancer 2026: The future we choose together*. Geneva: World Health Organization, 2026. ISBN: 978-92-4-012397-7. URL: https://www.who.int/publications/i/item/9789240123977.

[2] European Commission. *Commission Staff Working Document: Review of Europe's Beating Cancer Plan*. Tech. rep. SWD(2025) 39 final. Brussels: European Commission, 2025.

[3] World Health Organization and International Agency for Research on Cancer. *Global Cancer Observatory*. 2024. URL: https://gco.iarc.who.int/.

[4] American Cancer Society. *Cancer Facts & Figures 2026*. Atlanta, GA: American Cancer Society, 2026.

[5] Christopher J. Halbrook, Costas A. Lyssiotis, Marina Pasca di Magliano, et al. "Pancreatic cancer: Advances and challenges". In: *Cell* 186.8 (2023), pp. 1729–1754. DOI: 10.1016/j.cell.2023.02.014.

[6] J. D. Mizrahi et al. "Pancreatic cancer". In: *The Lancet* 395.10242 (2020), pp. 2008–2020. DOI: 10.1016/S0140-6736(20)30974-0.

[7] Panagiotis Sarantis et al. "Pancreatic ductal adenocarcinoma: Treatment hurdles, tumor microenvironment and immunotherapy". In: *World Journal of Gastrointestinal Oncology* 12.2 (2020), pp. 173–181. DOI: 10.4251/wjgo.v12.i2.173.

[8] Akram Pourshams, Sahar Saeedi Sepanlou, Kevin S. Ikuta, et al. "The global, regional, and national burden of pancreatic cancer and its attributable risk factors in 195 countries and territories, 1990–2017: a systematic analysis for the Global Burden of Disease Study 2017". In: *The Lancet Gastroenterology & Hepatology* 4.12 (2019), pp. 934–947. DOI: 10.1016/S2468-1253(19)30347-4.

[9] A. Charalampopoulou et al. "Advancing Radiobiology: Investigating the Effects of Photon, Proton, and Carbon-Ion Irradiation on PANC-1 Cells in 2D and 3D Tumor Models". In: *Current Oncology* 32.1 (2025), p. 49. DOI: 10.3390/curroncol32010049.

[10] Amelia Barcellini et al. "Locally Advanced Pancreatic Ductal Adenocarcinoma: Challenges and Progress". In: *OncoTargets and Therapy* 13 (2020), pp. 12705–12720. DOI: 10.2147/OTT.S220971.

[11] Giulia Giustarini et al. "Characterization of 3D heterocellular spheroids of pancreatic ductal adenocarcinoma for the study of cell interactions in the tumor immune microenvironment". In: *Frontiers in Oncology* 13 (2023), p. 1156769. DOI: 10.3389/fonc.2023.1156769.

[12] Olga Sokol and Marco Durante. "Carbon Ions for Hypoxic Tumors: Are We Making the Most of Them?" In: *Cancers* 15.18 (2023), p. 4494. DOI: 10.3390/cancers15184494.

[13] Barbara Vischioni et al. "Radioresistant, Rare, Recurrent, and Radioinduced: 4Rs of Hadrontherapy for Patients Selections". In: *International Journal of Particle Therapy* 15 (2025), p. 100737. ISSN: 2331-5180. DOI: 10.1016/j.ijpt.2024.100737.

[14] Heying Yao et al. "Evolution of Particle Radiotherapy: From Physical to Dual Targeting in Precision Medicine". In: *Molecular Pharmaceutics* 23.5 (2026), pp. 2829–2847. DOI: 10.1021/acs.molpharmaceut.6c00111.

[15] L. S. Yu et al. "Tissue Architecture Influences the Biological Effectiveness of Boron Neutron Capture Therapy in In Vitro/In Silico Three-Dimensional Self-Assembly Cell Models of Pancreatic Cancers". In: *Cancers* 13.16 (2021), p. 4058. DOI: 10.3390/cancers13164058.

[16] Z. Zhou et al. "'Cell knife' for cancer: the clinician's perspective". In: *Frontiers in Immunology* 16 (2025), p. 1536355. DOI: 10.3389/fimmu.2025.1536355.

[17] Q. Ma, P. Zhang, H. Zhang, et al. "Core clinical procedures and efficacy-enhancing strategies in boron neutron capture therapy". In: *Discover Oncology* 17 (2026), p. 591. DOI: 10.1007/s12672-026-04774-y.

[18] A. Charalampopoulou, F. De Luca, G. Magro, et al. “The rise of 3D spheroids in radiobiology for assessing tumour radioresistance”. In: *Acta Oncologica* 65 (2026), pp. 46–58. DOI: 10.2340/1651-226X.2026.45079.

[19] W. Li et al. “3D Biomimetic Models to Reconstitute Tumor Microenvironment In Vitro: Spheroids, Organoids, and Tumor-on-a-Chip”. In: *Advanced Healthcare Materials* 12.14 (2023), p. 2202609. DOI: 10.1002/adhm.202202609.

[20] Soukaina El Harane et al. “Cancer Spheroids and Organoids as Novel Tools for Research and Therapy: State of the Art and Challenges to Guide Precision Medicine”. In: *Cells* 12.7 (2023), p. 1001. DOI: 10.3390/cells12071001.

[21] Artur A. Akhunzianov et al. “Resistance to Radiotherapy in Cancer”. In: *Diseases* 13.1 (2025), p. 22. DOI: 10.3390/diseases13010022.

[22] World Health Organization. *Health topics: cancer*. 2026. URL: https://www.who.int/health-topics/cancer#tab=tab_1.

[23] Murat Beyzadeoglu, Gokhan Ozyigit, and Cuneyt Ebruli. *Basic Radiation Oncology*. 2nd. Springer, 2022. DOI: 10.1007/978-3-030-87308-0.

[24] National Cancer Institute. *What is cancer?* 2026. URL: https://www.cancer.gov/about-cancer/understanding/what-is-cancer.

[25] Sandra Morović. “Tumor Hypoxia and Radioresistance”. In: *Radiology and Oncology* 48.2 (2024), pp. 52–58. DOI: 10.55378/rv.48.2.6.

[26] Wafa Bouleftour, Eric Rowinski, Sabrine Louati, et al. “A Review of the Role of Hypoxia in Radioresistance in Cancer Therapy”. In: *Medical Science Monitor* 27 (2021), e934116. DOI: 10.12659/MSM.934116.

[27] Élisabeth Cohen-Jonathan-Moyal et al. “Radioresistant tumours: From identification to targeting”. In: *Cancer/Radiothérapie* 24.6–7 (2020), pp. 699–705. DOI: 10.1016/j.canrad.2020.05.005.

[28] Eric J. Hall and Amato J. Giaccia. *Radiobiology for the Radiologist*. 7th. Lippincott Williams & Wilkins, 2012. ISBN: 978-1-60831-193-4.

[29] Jr. Bast Robert C. et al., eds. *Holland-Frei Cancer Medicine*. 5th. Hamilton (ON): BC Decker, 2000. URL: https://www.ncbi.nlm.nih.gov/books/NBK20777/.

[30] Columbia University Department of Surgery. *What is Pancreatic Cancer?* 2026. URL: https://columbiasurgery.org/conditions-and-treatments/pancreatic-cancer#what-is-pancreatic-cancer.

[31] Frank Gaillard, Craig Hacking, Mohammad Niknejad, et al. *Pancreatic ductal adenocarcinoma*. 2026. DOI: 10.53347/rID-6736. URL: https://doi.org/10.53347/rID-6736 (visited on 06/28/2026).

[32] Marco Dell’Oro et al. “Clinical Limitations of Photon, Proton and Carbon Ion Therapy for Pancreatic Cancer”. In: *Cancers* 12.1 (2020), p. 163. DOI: 10.3390/cancers12010163.

[33] Francesco Pezzella, Mahvash Tavassoli, and David J. Kerr, eds. *Oxford Textbook of Cancer Biology*. Oxford Textbooks in Oncology. Oxford University Press, 2019. DOI: 10.1093/med/9780198779452.001.0001.

[34] Ervin B. Podgorsak. *Radiation Physics for Medical Physicists*. Biological and Medical Physics, Biomedical Engineering. Springer, 2010. DOI: 10.1007/978-3-642-008745-7.

[35] Joel E. Tepper, Robert L. Foote, and Jeff M. Michalski. *Clinical Radiation Oncology*. 5th. Elsevier, 2021. ISBN: 978-0-323-67246-7.

[36] D. J. Buglewicz et al. “Biological Effects of Monoenergetic Carbon Ions and Their Associated Secondary Particles”. In: *Frontiers in Oncology* 12 (2022), p. 788293. ISSN: 2234-343X. DOI: 10.3389/fonc.2022.788293. URL: https://www.frontiersin.org/journals/oncology/articles/10.3389/fonc.2022.788293/full.

[37] Agnes Schipler and George Iliakis. “DNA double-strand–break complexity levels and their possible contributions to the probability for error-prone processing and repair pathway choice”. In: *Nucleic Acids Research* 41.16 (2013), pp. 7589–7605. DOI: 10.1093/nar/gkt556.

[38] International Atomic Energy Agency. *Advances in Boron Neutron Capture Therapy*. Non-serial Publications. Vienna: IAEA, 2023.

[39] W. H. Jin et al. “A Review of Boron Neutron Capture Therapy: Its History and Current Challenges”. In: *International Journal of Particle Therapy* 9.1 (2022), pp. 71–82. ISSN: 2331-5180. DOI: 10.14338/IJPT-22-00002.1.

[40] Son Long Ho et al. “Gadolinium Neutron Capture Therapy (GdNCT) Agents from Molecular to Nano: Current Status and Perspectives”. In: *ACS Omega* 7.3 (2022), pp. 2533–2553. DOI: 10.1021/acsomega.1c06603.

[41] D. Zheng et al. “Boron Neutron Capture Therapy: A Technology-Driven Renaissance”. In: *Cancers* 18.3 (2026), p. 498. DOI: 10.3390/cancers18030498.

[42] Shuai Wang et al. “Boron Neutron Capture Therapy: Current Status and Challenges”. In: *Frontiers in Oncology* 12 (2022), p. 788770. DOI: 10.3389/fonc.2022.788770.

[43] S. Long Ho et al. “Gadolinium Neutron Capture Therapy (GdNCT) Agents from Molecular to Nano: Current Status and Perspectives”. In: *ACS Omega* 7.3 (2022), pp. 2533–2553. DOI: 10.1021/acsomega.1c06603.

[44] Simonetta Geninatti-Crich et al. “MRI-Guided Neutron Capture Therapy by Use of a Dual Gadolinium/Boron Agent Targeted at Tumour Cells through Upregulated Low-Density Lipoprotein Transporters”. In: *Chemistry – A European Journal* 17.30 (2011), pp. 8479–8486. DOI: https://doi.org/10.1002/chem.201003741. eprint: https://chemistry-europe.onlinelibrary.wiley.com/doi/pdf/10.1002/chem.201003741. URL: https://chemistry-europe.onlinelibrary.wiley.com/doi/abs/10.1002/chem.201003741.

[45] Sahar Rakhshan et al. “A Comparative Study of 157Gd and 10B Effect in a Carborane-Based Theranostic Agent for Membrane-Targeted Carbonic Anhydrase IX Inhibition and MRI-Guided Neutron Capture Therapy in Mesothelioma Treatment”. In: *ACS Central Science* 11.11 (Nov. 2025), pp. 2215–2229. ISSN: 2374-7943. DOI: 10.1021/acscentsci.5c01632. eprint: https://pubs.acs.org/acscii/article-pdf/11/11/2215/42290036/oc5c01632.pdf. URL: https://doi.org/10.1021/acscentsci.5c01632.

[46] G. Gonçalves et al. “Lithium halide filled carbon nanocapsules: Paving the way towards lithium neutron capture therapy (LiNCT)”. In: *Carbon* 208 (2023), pp. 148–159. ISSN: 0008-6223. DOI: 10.1016/j.carbon.2023.03.034.

[47] A. A. Morris et al. “Advancing lithium neutron capture therapy: ^{6}Li-loaded nanoparticles and laser-driven neutron sources”. In: *Applied Physics Letters* 124.4 (2024), p. 043701. DOI: 10.1063/5.0185189.

[48] Katharina Seidensaal et al. “The role of combined ion-beam radiotherapy (CIBRT) with protons and carbon ions in a multimodal treatment strategy of inoperable osteosarcoma”. In: *Radiotherapy and Oncology* 159 (2021), pp. 8–16. ISSN: 0167-8140. DOI: 10.1016/j.radonc.2021.01.029.

[49] Y. Li et al. “Flourish of Proton and Carbon Ion Radiotherapy in China”. In: *Frontiers in Oncology* 12 (2022), p. 819905. DOI: 10.3389/fonc.2022.819905.

[50] Stefan Rieken, Daniel Habermehl, Thomas Haberer, et al. “Proton and carbon ion radiotherapy for primary brain tumors delivered with active raster scanning at the Heidelberg Ion Therapy Center (HIT): early treatment results and study concepts”. In: *Radiation Oncology* 7 (2012), p. 41. DOI: 10.1186/1748-717X-7-41.

[51] Mitra Safavi-Naeini, A. Chacon, Susanna Guatelli, et al. “Opportunistic dose amplification for proton and carbon ion therapy via capture of internally generated thermal neutrons”. In: *Scientific Reports* 8 (2018), p. 16257. DOI: 10.1038/s41598-018-34643-w.

[52] Alessandro Somenzi et al. “O066 / #563 - COMBINING CARBON-IONS RADIOTHERAPY AND BORON NEUTRON CAPTURE THERAPY: FIRST IN VITRO EXPLORATION OF AN INNOVATIVE STRATEGY FOR RADIORESISTANT TUMORS”. In: *International Journal of Particle Therapy* 17 (2025). PTCOG 63, p. 100822. ISSN: 2331-5180. DOI: 10.1016/j.ijpt.2025.100822. URL: https://www.sciencedirect.com/science/article/pii/S233151802500085X.

[53] Y. Han et al. “Combined BNCT-CIRT treatment planning for glioblastoma using the effect-based optimization”. In: *Physics in Medicine & Biology* 69.1 (2023), p. 015001. DOI: 10.1088/1361-6560/ad120f.

[54] Srinivas Gunti et al. “Organoid and Spheroid Tumor Models: Techniques and Applications”. In: *Cancers* 13.4 (2021), p. 874. DOI: 10.3390/cancers13040874.

[55] Brendon M. Baker and Christopher S. Chen. “Deconstructing the third dimension – how 3D culture microenvironments alter cellular cues”. In: *Journal of Cell Science* 125.13 (2012), pp. 3015–3024. DOI: 10.1242/jcs.079509.

[56] G. Rauner, Piyush B. Gupta, and Charlotte Kuperwasser. “From 2D to 3D and beyond: the evolution and impact of in vitro tumor models in cancer research”. In: *Nature Methods* 22 (2025), pp. 1776–1787. DOI: 10.1038/s41592-025-02769-1.

[57] Ana Maria B. Garnique et al. “Two-Dimensional and Spheroid-Based Three-Dimensional Cell Culture Systems: Implications for Drug Discovery in Cancer”. In: *Drugs and Drug Candidates* 3.2 (2024), pp. 391–409. DOI: 10.3390/ddc3020024.

[58] Parul Benien and Archana Swami. “3D Tumor Models: History, Advances and Future Perspectives”. In: *Future Oncology* 10.7 (2014), pp. 1311–1327. DOI: 10.2217/fon.13.274.

[59] Michaela Stadler et al. “Increased complexity in carcinomas: Analyzing and modeling the interaction of human cancer cells with their microenvironment”. In: *Seminars in Cancer Biology* 35 (2015), pp. 107–124. ISSN: 1044-579X. DOI: 10.1016/j.semcancer.2015.08.007.

[60] Junfang Tu et al. “Cancer spheroids derived exosomes reveal more molecular features relevant to progressed cancer”. In: *Biochemistry and Biophysics Reports* 26 (2021), p. 101026. ISSN: 2405-5808. DOI: https://doi.org/10.1016/j.bbrep.2021.101026. URL: https://www.sciencedirect.com/science/article/pii/S2405580821001205.

[61] Gianpiero Lazzari et al. “Multicellular spheroid based on a triple co-culture: A novel 3D model to mimic pancreatic tumor complexity”. In: *Acta Biomaterialia* 78 (2018), pp. 296–307. ISSN: 1742-7061. DOI: https://doi.org/10.1016/j.actbio.2018.08.008. URL: https://www.sciencedirect.com/science/article/pii/S1742706118304665.

[62] Monika Szczepanek. “3D melanoma model for in vitro BNCT studies: effects of neutron radiation on ^{10}BPA-loaded melanoma spheroids”. PhD thesis. Jagiellonian University, 2024.

[63] Denise B. Pelowitz et al. *MCNP6 User’s Manual*. Tech. rep. LA-CP-13-00634. Los Alamos, NM, USA: Los Alamos National Laboratory, May 2013.

[64] Alessandro Somenzi. “Studi sull’efficacia di ioni carbonio e Boron Neutron Capture Therapy in cellule di adenocarcinoma pancreatico”. Master’s thesis. Università degli Studi di Pavia, 2023. URL: https://unitesi.unipv.it/handle/20.500.14239/16584.

[65] David R. White et al. “4. The Composition of Body Tissues”. In: *Journal of the International Commission on Radiation Units and Measurements* os-23.1 (1989), pp. 20–23. DOI: 10.1093/jicru_os23.1.20.

[66] International Commission on Radiological Protection. “ICRP Publication 110: Adult Reference Computational Phantoms”. In: *Annals of the ICRP* 39.2 (2009). Table A.1, pp. 48–51. DOI: 10.1016/j.icrp.2009.09.001.

[67] Nicola Wheeler, Kayode Dada, and Carrie Minnaar. “An overview of the developments in 3D cancer cell models, assay techniques, and imaging modalities”. In: *Human Cell* 39 (Apr. 2026). DOI: 10.1007/s13577-026-01375-3.

[68] Greiner Bio-One. *Customer Drawing: CELLSTAR® PS Microplate, 96-Well, U-Bottom, Cell-Repellent Surface (Item No. 650970, Rev. 1)*. Technical drawing, released 2015-03-16. Greiner Bio-One GmbH. Frickenhausen, Germany, 2015.

[69] S. Bortolussi et al. “Neutron flux and gamma dose measurement in the BNCT irradiation facility at the TRIGA reactor of the University of Pavia”. In: *Nuclear Instruments and Methods in Physics Research Section B: Beam Interactions with Materials and Atoms* 414 (2018), pp. 113–120. ISSN: 0168-583X. DOI: https://doi.org/10.1016/j.nimb.2017.10.023. URL: https://www.sciencedirect.com/science/article/pii/S0168583X17309424.

[70] Matteo Ferrari. “Characterization of the Gamma Dose Component in the BNCT Irradiation Facility and Dosimetry for *in Vitro* Experiments at the TRIGA Reactor in Pavia”. Academic Year 2013/2014. Master’s thesis. University of Pavia, 2014.

[71] Judith F. Briesmeister. *MCNP—A General Monte Carlo N-Particle Transport Code, Version 4C*. Tech. rep. LA-13709-M. Los Alamos, NM: Los Alamos National Laboratory, 2000.

[72] M. Szczepanek, M. Silarski, A. Panek, et al. “Effect of Neutron Radiation on ^{10}BPA-Loaded Melanoma Spheroids and Melanocytes”. In: *Cells* 14.3 (2025), p. 232. DOI: 10.3390/cells14030232. URL: https://doi.org/10.3390/cells14030232.

[73] American Type Culture Collection. *PANC-1 (ATCC® CRL-1469™)*. https://www.atcc.org/products/crl-1469. Accessed: 2026-09-13. n.d.

[74] Jolanta Kulesza, Monika Pawłowska, and Ewa Augustin. “The Influence of Antitumor Unsymmetrical Bisacridines on 3D Cancer Spheroids Growth and Viability”. In: *Molecules* 26.20 (2021). ISSN: 1420-3049. URL: https://www.mdpi.com/1420-3049/26/20/6262.

[75] Johannes Schindelin et al. “Fiji: An Open-Source Platform for Biological-Image Analysis”. In: *Nature Methods* 9.7 (2012), pp. 676–682. DOI: 10.1038/nmeth.2019.

[76] Thermo Fisher Scientific. *CyQUANT™ LDH Cytotoxicity Assay User Guide*. Pub. No. MAN0000000, Rev. B.0; Cat. No. C20301. Thermo Fisher Scientific Inc. Waltham, MA, USA, 2020. URL: https://www.thermofisher.com.

[77] Robert Thomas. *Practical Guide to ICP-MS: A Tutorial for Beginners*. 3rd. Boca Raton, FL: CRC Press, 2013. DOI: 10.1201/b14923.

[78] E.H. Evans. “ATOMIC MASS SPECTROMETRY | Inductively Coupled Plasma”. In: *Encyclopedia of Analytical Science (Second Edition)*. Ed. by Paul Worsfold, Alan Townshend, and Colin Poole. Second Edition. Oxford: Elsevier, 2005, pp. 229–237. ISBN: 978-0-12-369397-6. DOI: https:

//doi.org/10.1016/B0-12-369397-7/00036-4. URL: https://www.sciencedirect.com/science/article/pii/B0123693977000364.

[79] S. Bortolussi and S. Altieri. "Thermal neutron irradiation field design for boron neutron capture therapy of human explanted liver". In: *Medical Physics* 34.12 (2007), pp. 4700–4705. DOI: https://doi.org/10.1118/1.2795831. eprint: https://aapm.onlinelibrary.wiley.com/doi/pdf/10.1118/1.2795831. URL: https://aapm.onlinelibrary.wiley.com/doi/abs/10.1118/1.2795831.

[80] M.A. Gadan et al. "Set-up and calibration of a method to measure 10B concentration in biological samples by neutron autoradiography". In: *Nuclear Instruments and Methods in Physics Research Section B: Beam Interactions with Materials and Atoms* 274 (2012), pp. 51–56. ISSN: 0168-583X. DOI: https://doi.org/10.1016/j.nimb.2011.11.043. URL: https://www.sciencedirect.com/science/article/pii/S0168583X11010743.

[81] Fondazione CNAO. *CNAO Synchrotron*. 2026. URL: https://fondazionecnao.it/adroterapia/sincrotrone.

[82] Nicolaas A. P. Franken et al. "Clonogenic assay of cells in vitro". In: *Nature Protocols* 1.5 (2006), pp. 2315–2319. DOI: 10.1038/nprot.2006.339.

[83] Martina Ricci et al. "Morphological Analysis of US Treated PANC-1 Spheroids". In: *Applied Sciences* 15.4 (2025). ISSN: 2076-3417. DOI: 10.3390/app15041707. URL: https://www.mdpi.com/2076-3417/15/4/1707.

[84] Subhash Chandra et al. "Quantitative evaluation of boron neutron capture therapy (BNCT) drugs for boron delivery and retention at subcellular-scale resolution in human glioblastoma cells with imaging secondary ion mass spectrometry (SIMS)". In: *Journal of Microscopy* 254.3 (2014), pp. 146–156. DOI: 10.1111/jmi.12126.

[85] Yoshikatsu Kanai. "Amino acid transporter LAT1 (SLC7A5) as a molecular target for cancer diagnosis and therapeutics". In: *Pharmacology & Therapeutics* 230 (2022), p. 107964. DOI: 10.1016/j.pharmthera.2021.107964.

[86] Mariafrancesca Scalise et al. "Crossing the Borders: The amino acid transporter LAT1 (SLC7A5) in the Blood-Brain Barrier". In: *Neurochemistry International* 191 (2025), p. 106070. DOI: 10.1016/j.neuint.2025.106070.

[87] Yixi Zhao et al. "Advances in the development of large neutral amino acid transporter 1 (LAT1) substrate analogues and inhibitors for the delivery of drugs and radiopharmaceuticals". In: *European Journal of Medicinal Chemistry* 302 (2026), p. 118382. DOI: 10.1016/j.ejmech.2025.118382.

[88] F. Zachariah Ali, A. P. Morrell, P. R. Golda, et al. "Quantitative LA-ICP-MS Imaging of Elemental Distributions with Protein Correlation in 3D Tumor Models". In: *Analytical Chemistry* 98.31 (2026), pp. 23164–23178. DOI: 10.1021/acs.analchem.6c03012. URL: https://doi.org/10.1021/acs.analchem.6c03012.

[89] V. Levrague et al. "Impact of intracellular radionuclide distribution in a Monte Carlo biophysical 3D multi-cellular model for targeted alpha therapy". In: *Medical Physics* 52.7 (July 2025), e17917. DOI: 10.1002/mp.17917.

[90] Haoyi Tang et al. "Radiation-induced bystander effect and its clinical implications". In: *Frontiers in Oncology* Volume 13 - 2023 (2023). ISSN: 2234-943X. DOI: 10.3389/fonc.2023.1124412. URL: https://www.frontiersin.org/journals/oncology/articles/10.3389/fonc.2023.1124412.